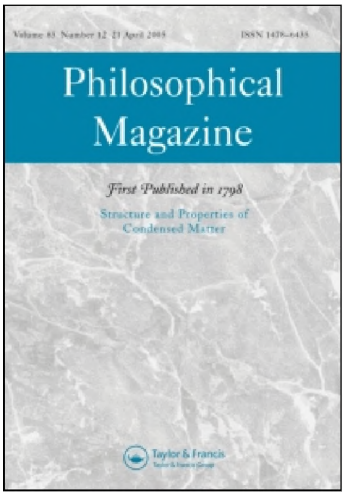

Philosophical Magazine
Publication details, including instructions for authors and subscription information:
http://www.informaworld.com/smpp/title~content=t713695589

Three-dimensional singular stress field at the front of a crack and lattice crack deviation (LCD) in a cubic single crystal plate

Reaz A. Chaudhuri [a]
[a] Department of Materials Science and Engineering, 122 S. Central Campus Dr., Room 304, University of Utah, Salt Lake City, Utah 84112-0560, USA

Online publication date: 12 May 2010

To cite this Article Chaudhuri, Reaz A.(2010) 'Three-dimensional singular stress field at the front of a crack and lattice crack deviation (LCD) in a cubic single crystal plate', Philosophical Magazine, 90: 15, 2049 — 2113
To link to this Article: DOI: 10.1080/14786430903571412
URL: http://dx.doi.org/10.1080/14786430903571412

Philosophical Magazine
Vol. 90, No. 15, 21 May 2010, 2049–2113

Taylor & Francis
Taylor & Francis Group

Three-dimensional singular stress field at the front of a crack and lattice crack deviation (LCD) in a cubic single crystal plate

Reaz A. Chaudhuri*

Department of Materials Science and Engineering, 122 S. Central Campus Dr., Room 304, University of Utah, Salt Lake City, Utah 84112-0560, USA

(*Received 6 July 2009; final version received 5 December 2009*)

A novel eigenfunction expansion technique, based in part on separation of the thickness variable, is developed to derive three-dimensional asymptotic stress fields in the vicinity of the front of a semi-infinite through-crack weakening an infinite plate made of a homogeneous cubic single crystal. Crack-side boundary conditions and those that are prescribed on the top and bottom (free) surfaces of the cubic crystal plate are exactly satisfied. Explicit expressions for singular stress fields in the vicinity of the front of through-thickness cracks, weakening cubic single crystal plates subjected to far-field extension/bending (mode I), sliding shear/twisting (mode II) and antiplane shear (mode III) loadings are presented. The present investigation considers three through-crack systems (crack plane)[crack front] × [propagation direction], (010)[001] × [100], $(\bar{1}10)[001] \times [110]$ and (110)[110] × [001], weakening cubic crystals, and their relatively easier cleavage planes for propagation. It also introduces a new concept of lattice crack deviation (LCD) barrier, which can explain the reported discrepancy between simulations and experiments with regards to crack deviation from a "difficult" cleavage system to an easier one. Additionally, the relationships of the easier cleavage systems based on the present solutions with the structural chemistry aspects of various single crystals, such as bcc alkali metals, bcc transition alkali metals, fcc transition metals, group IVA (diamond cubic) elements, usually ionic compounds (rock salt and fluorite structures), covalent compounds (zinc blende structure), etc., are also discussed. Finally, the LCD parameter is strongly correlated with the anisotropic ratio for the cracked cubic crystal concerned.

Keywords: three-dimensional eigenfunction; stress singularity; stress intensity factor; crack front; lattice crack deviation barrier; cubic single crystal; bond shear strain

1. Introduction

Single crystals are being increasingly used in high temperature applications, such as gas turbine rotor blades, primarily because of their creep resistance. Other possible and potential applications include rocket motor nozzles and spacecraft nose cones, power plants, refineries, chemical processing plants and so on. Creep deformation and rupture are initiated in the region of grain boundaries of a polycrystalline metal

*Email: r.chaudhuri@utah.edu

ISSN 1478–6435 print/ISSN 1478–6443 online

DOI: 10.1080/14786430903571412
http://www.informaworld.com

or alloy, and proceed by sliding and separation. Thus, creep rupture failures are intercrystalline, in contrast to the transcrystalline room temperature fatigue failures [1]. The problem of intercrystalline failure is partially alleviated by coarse grain size, which reduces the length of grain boundary, and is altogether eliminated by the employment of single crystal materials.

Cubic single crystals, which are characterized by the highest level of symmetry (with the exception of isotropic one), occupy a special place in materials technology, because of the preponderance of these materials in both traditional and modern (high technology) industrial applications (roughly 30% of 5572 inorganic crystals listed by Nowacki [2] belong to this category). For example, many important metals, such as Fe, Cu, Ag, Au, Al, Ni, Pt, etc., are widely used, and some of them, e.g. Cu and Fe, have defined human civilizations. MgO (magnesia), with a rock salt unit cell, is a traditional refractory ceramic widely used in the steel industry. UO_2 (uranium dioxide) is a reactor fuel ceramic that can accommodate fission products, such as helium gas, in the unoccupied volume near the center of its fluorite unit cell, without troublesome swelling [3]. $BaTiO_3$ (barium titanate), which has perovskite unit cell above 120°C, and other perovskite ceramics have important ferroelectric and piezoelectric properties. Electronic ceramics such as $BaTiO_3$ and magnetic ceramics such as $NiFe_2O_4$ (nickel ferrite), with inverse spinel unit cell, represent the largest part of the industrial ceramics market. YSZ (Y_2O_3-stabilized ZrO_2), a cubic single crystal ceramic with perovskite structure, is used in solid oxide fuel cells.

The most important cubic single crystals are, however, the intrinsic elemental semiconductors of group IVA of the periodic table, i.e. Si (silicon) and Ge (germanium) of ultrahigh purity (with diamond cubic structure), and their extrinsic versions, wherein very small amounts of dopants are added in a highly controlled way. Almost equally important are intrinsic compound semiconductors formed from elements near group IVA, such as III–V (e.g. AlSb, GaP, GaAs, GaSb, InP, InAs, InSb) and II–VI (e.g. ZnS, ZnSe, ZnTe, CdS, CdTe, HgTe) compounds with zinc blende unit cells as well as their extrinsic versions.

Stroh [4], following the lead of Eshelby et al. [5], appears to be among the first to study the weakening effect of a crack in two-dimensional anisotropic single crystals of which the cubic forms a special case, since these materials are characterized by three independent elastic constants [6,7] and display the highest level of symmetry among the family of single crystals. The study by Sih et al. [8] pertaining to the two-dimensional singular stress field at the tip of a crack weakening an anisotropic plate, can be employed to its cubic single crystal counterpart. Other follow-up studies pertaining to cracks in two-dimensional anisotropic solids include Cherepanov [9], Sham and Zhou [10] and Argatov and Nazarov [11] among others. Significant progress in research on a two-dimensional cracked anisotropic solid notwithstanding, the corresponding progress in its three-dimensional counterpart appears to be marked by its complete absence. This is because mathematical difficulties posed by problems pertaining to the three-dimensional cracked solids, including single cubic crystals, are substantially greater than their two-dimensional counterparts. More important, the above papers that employ the Lekhnitskii (e.g. [8,9]) and Stroh (e.g. [10]) type formulations are all based on complex variables. Since the three-dimensional space is too small to accommodate the next higher dimensional analog of complex variables (for which at least a four-dimensional space will be required),

these complex variables based techniques are by themselves not adequate in solving problems pertaining to three-dimensional cracked anisotropic solids. The first objective of the present paper is to bridge this long-standing mathematical gap.

Because of its importance to the modern electronics industry, and also because silicon can be produced as a virtually dislocation-free single crystal [12,13], crack propagation in this cubic crystal has been investigated experimentally (see, for example, [14–26]) as well as computationally, e.g. [26–32] (atomistic simulation using both molecular dynamics and density functional theory or a hybrid approach) for its fracture characteristics by a number of researchers. Other important cubic single crystals that have been investigated include gallium arsenide (GaAs) [33,34] and tungsten (W) [35–38] among others. Cracks in silicon single crystals have been observed in the transmission electron microscope to propagate in the absence of dislocations [13]. Silicon is reported to have two principal cleavage planes: {111} planes, usually the easy cleavage planes [17] and {110} planes [16]. Different crack propagation directions have been investigated for both crack planes using atomistic simulations by Perez and Gumbsch [28]. In GaAs, because of its ionicity, brittle fracture would produce two charged surfaces on {111} planes, thus more or less ruling them out as cleavage planes [33]. However, only neutral surfaces would be produced on {110} planes upon cleavage, making them the preferred cleavage planes in GaAs. Margevicius and Gumbsch [33] have experimentally investigated fracture toughness of GaAs, and also different crack propagation directions on {110}, the easy cleavage planes for polar semiconductors. More recently, Kermode et al. [26] have investigated low-speed propagation instabilities in silicon using quantum-mechanical hybrid, multiscale modeling and single-crystal fracture experiments.

Two long-standing issues pertaining to the phenomenon of brittle fracture in single crystals relate to the ability (or lack thereof) to predict more favorable or easier cleavage planes as mentioned above, and the associated phenomenon of crack deviation, which constitute the second objective of the present investigation. As Perez and Gumbsch [28] have rightly observed, anisotropy with respect to the crack propagation direction is difficult to understand theoretically, which is the primary focus of the present investigation. This is especially true for the three-dimensional crack problem, which has remained a challenge to the researchers in the field.

Thomson et al. [39] have been the first to discover the manifestation of the lattice trapping effect in a finite stability range of stress intensity factors for a crack of given length. The magnitude of the lattice trapping strongly changes with the bonding characteristics [40–42]. On the atomic scale, the breaking of the bonds naturally depends on their orientation with respect to the loading axis. Kohloff et al. [43] have shown through atomistic simulations that the lattice trapping effect [39] is anisotropic with respect to the orientation of the crack front on a given cleavage plane. The effect of lattice trapping in a Si single crystal has more recently been investigated by Perez and Gumbsch [28], and Bernstein and Hess [30] through atomistic simulations. Margevicius and Gumbsch [33] and Riedle et al. [38] have experimentally investigated the same in monocrystalline GaAs and W, respectively. More importantly, Riedle et al. [38] have measured fracture toughness of four low-index crack systems in W at temperatures between room temperature and 77 K

(liquid nitrogen temperature). At 77 K, the dislocation activity is not substantial, which has prompted them to conclude that "the brittle fracture process itself must be anisotropic", with respect to not only to the plane but also to the direction of crack propagation [38]. Such anisotropy has been explained by these authors [38] in terms of the discrete atomistic nature of the crystal, and has been considered to be a "consequence of anisotropic lattice trapping".

Perez and Gumbsch [28] have observed two distinct types of bond breaking processes: (i) a continuous process without pronounced structural relaxations leading to a small lattice trapping range, and (ii) a clearly discontinuous abrupt bond breaking event resulting in a large lattice trapping range. Low lattice trapping results in low fracture toughness and easy propagation of cracks in directions in which a continuous bond breaking occurs [28]. The discontinuous bond breaking process which results from higher lattice trapping, in contrast, pertains to structural rearrangements and relaxations involving about 8 to 10 atoms in the immediate vicinity of the crack tip or front [28]. This would lead to higher fracture toughness. Great strides made in the computer simulations notwithstanding, any agreement of simulation results with experiments can at best be deemed qualitative [28]. For silicon, propagation in the "difficult" direction predicted by Perez and Gumbsch [28] via simulation could not be seen in cleavage experiments [17,28]. Whereas experiments would exhibit a deviation of the crack onto an inclined plane, the crack would continue to propagate in the original plane according to simulations [28]. The present investigation intends to resolve this issue by introducing a new concept of lattice crack deviation (LCD) parameter, which can explain the above-mentioned discrepancy between simulations and experiments.

In what follows, a simple, yet novel eigenfunction expansion type method, based on the partial separation of z-variables technique [44–47], is developed to obtain three-dimensional asymptotic displacement and stress fields in the vicinity of the front of a semi-infinite crack weakening a cubic single crystal plate. Section 2 provides a mathematical statement of the problem under investigation. The solution of a new eigenfunction expansion method is developed to obtain explicit expressions for three-dimensional asymptotic singular stress fields in the vicinity of a point located at the front of a crack, subjected to the free-free crack-side boundary condition. The general approach is outlined in Section 4. Expressions for the singular stress field in the vicinity of a (010)[001] crack front weakening a plate subjected to anti-plane shear loading are presented in Section 4. Expressions for the singular stress fields in the vicinity of the fronts of two different through-cracks, namely, (010)[001] and $(\bar{1}10)$[001], shown in Figures 1 and 2, respectively, weakening a cubic single crystal plate subjected to extension/bending are presented in Sections 5 and 6, respectively. The details of the mathematical derivation of the solutions for the mode I/II loading case, involving complex and imaginary roots, are presented in Appendix 1 and Appendix 2, respectively. Expressions for displacements and singular stress fields in the neighborhood of the front of the through-crack, $(1\bar{1}0)$[110](not shown), weakening a cubic single crystal plate subjected to anti-plane shear and extension/bending are presented in Section 7 and Appendix 3. Appendix 4 presents comparisons (i.e. similarities/dissimilarities) of solutions involving complex and imaginary roots with their isotropic counterpart. Sections 8 and 9 present the concept of as well as the expression for the LCD energy barrier and crack deviation

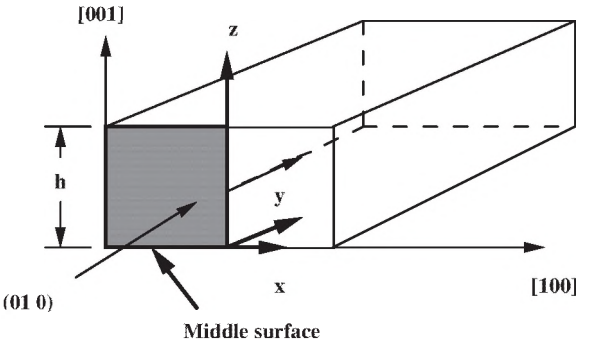

Figure 1. Schematic of the top half of a cubic crystal weakened by a (010) [001] through-crack.

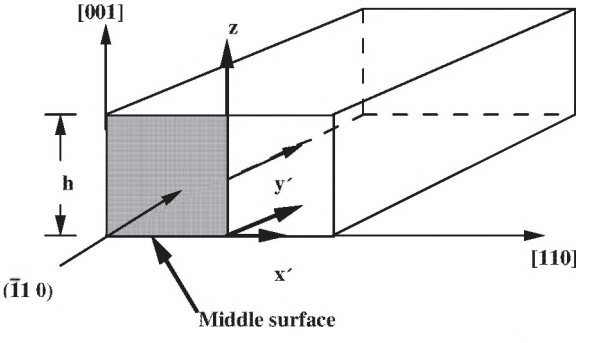

Figure 2. Schematic of the top half of a cubic crystal weakened by a ($\bar{1}$10)[001] through-crack.

analysis, respectively, while their mathematical details are presented in Appendix 5 and Appendix 6, respectively. Structure–fracture property relationships for certain classes of cubic crystals are presented in Section 10, whereas some important and interesting numerical results are presented in Section 11.

2. Formulation of the problem of a (010)[001] through-crack propagating along the [100] direction

The Cartesian coordinate system (x, y, z) is convenient to describe the deformation behavior in the vicinity of a semi-infinite crack weakening an infinite plate made of a homogeneous cubic single crystal material (Figure 1). The cleavage plane considered is (010), which belongs to the {100} family of planes. Here, the z-axis is placed along the straight crack front [001], whereas the coordinates x [100], y [010], are used to define the direction along the length of the crack (propagation direction) and the direction transverse to it, respectively, in the middle plane of the plate. u, v and w represent the components of the displacement vector in the x, y and z directions, respectively.

The stress–strain relationships for a cubic single crystal are given by [6,7]

$$\begin{Bmatrix} \sigma_x \\ \sigma_y \\ \sigma_z \\ \tau_{yz} \\ \tau_{xz} \\ \tau_{xy} \end{Bmatrix} = \begin{bmatrix} c_{11} & c_{12} & c_{12} & 0 & 0 & 0 \\ c_{12} & c_{11} & c_{12} & 0 & 0 & 0 \\ c_{12} & c_{12} & c_{11} & 0 & 0 & 0 \\ 0 & 0 & 0 & c_{66} & 0 & 0 \\ 0 & 0 & 0 & 0 & c_{66} & 0 \\ 0 & 0 & 0 & 0 & 0 & c_{66} \end{bmatrix} \begin{Bmatrix} \varepsilon_x \\ \varepsilon_y \\ \varepsilon_z \\ \gamma_{yz} \\ \gamma_{xz} \\ \gamma_{xy} \end{Bmatrix}, \tag{1}$$

where c_{ij}, $i, j = 1, \ldots, 6$, denotes the elastic stiffnesses of a cubic single crystal plate. s_{ij}, $i, j = 1, \ldots, 6$, denotes the corresponding elastic compliances. The three equilibrium equations for a linear elastic solid, made of a cubic single crystal material, can be expressed in terms of the displacement components, u, v, and w, as follows:

$$c_{11}\frac{\partial^2 u}{\partial x^2} + c_{66}\frac{\partial^2 u}{\partial y^2} + c_{66}\frac{\partial^2 u}{\partial z^2} + (c_{12} + c_{66})\frac{\partial^2 v}{\partial x \partial y} + (c_{12} + c_{66})\frac{\partial^2 w}{\partial x \partial z} = 0, \tag{2a}$$

$$(c_{12} + c_{66})\frac{\partial^2 u}{\partial x \partial y} + c_{66}\frac{\partial^2 v}{\partial x^2} + c_{11}\frac{\partial^2 v}{\partial y^2} + c_{66}\frac{\partial^2 v}{\partial z^2} + (c_{12} + c_{66})\frac{\partial^2 w}{\partial y \partial z} = 0, \tag{2b}$$

$$(c_{12} + c_{66})\frac{\partial^2 u}{\partial x \partial z} + (c_{12} + c_{66})\frac{\partial^2 v}{\partial y \partial z} + c_{66}\frac{\partial^2 w}{\partial x^2} + c_{66}\frac{\partial^2 w}{\partial y^2} + c_{11}\frac{\partial^2 w}{\partial z^2} = 0. \tag{2c}$$

The boundary conditions include those at the plate faces and crack-side surfaces. The three boundary conditions imposed on the plate faces, $z = \pm h$, are given as follows:

(1) Stress-free:

$$\tau_{xz} = \tau_{yz} = \sigma_z = 0, \tag{3a}$$

(2) Fixed:

$$u = v = w = 0, \tag{3b}$$

(3) Lubricated:

$$\tau_{xz} = \tau_{yz} = w = 0, \tag{3c}$$

whereas those at the crack-side free surfaces are more conveniently expressed in local cylindrical polar coordinates, $\theta = \pm\pi$, and are given as follows:

$$\sigma_\theta = \tau_{r\theta} = \tau_{\theta z} = 0. \tag{4}$$

The assumed displacement functions for the three-dimensional crack problem under consideration are selected on the basis of separation of z-variables [44–47]. These are as given below:

$$u(x, y, z) = \exp(ikz)U(x, y), \tag{5a}$$

$$v(x, y, z) = \exp(ikz)V(x, y), \tag{5b}$$

$$w(x, y, z) = \exp(ikz)W(x, y), \tag{5c}$$

where $k \in Z$, the set of integers. It may be noted that since the z-dependent term and its first partial derivative can either be bounded and integrable at most admitting ordinary discontinuities, or the first partial derivative can at worst be square integrable (in the sense of Lebesgue integration) in its interval $z \in [-h, h]$, i.e. admitting singularities weaker than square root (i.e. $z^{-1/2+\varepsilon}$, $\varepsilon > 0$), it can be represented by Fourier series. The latter case is justified by the Riesz–Fischer theorem [48], and its physical implication is that of satisfying the criterion of finiteness of local strain energy and path independence [49]. Thus, the separation of the z-dependent term, which is the key to solving a three-dimensional crack problem, is a direct consequence of the Riesz–Fischer theorem. Substitution of Equation (5) into Equation (1) yields the following system of coupled partial differential equations (PDEs):

$$c_{11}\frac{\partial^2 U}{\partial x_1^2} + c_{66}\frac{\partial^2 U}{\partial y_1^2} + c_{66}U + (c_{12}+c_{66})\frac{\partial^2 V}{\partial x_1 \partial y_1} + (c_{12}+c_{66})\frac{\partial W}{\partial x_1} = 0, \tag{6a}$$

$$(c_{12}+c_{66})\frac{\partial^2 U}{\partial x_1 \partial y_1} + c_{66}\frac{\partial^2 V}{\partial x_1^2} + c_{11}\frac{\partial^2 V}{\partial y_1^2} + c_{66}V + (c_{12}+c_{66})\frac{\partial W}{\partial y_1} = 0, \tag{6b}$$

$$(c_{12}+c_{66})\frac{\partial U}{\partial x_1} + (c_{12}+c_{66})\frac{\partial V}{\partial y_1} + c_{66}\frac{\partial^2 W}{\partial x_1^2} + c_{66}\frac{\partial^2 W}{\partial y_1^2} + c_{11}W = 0, \tag{6c}$$

where

$$x_1 = ikx, \quad y_1 = iky. \tag{7}$$

3. Singular stress fields in the vicinity of a (010)[001] through-crack weakening a cubic single crystal plate subjected to general loading

The solution to the system of coupled partial differential equations, Equations (6), subjected to the most general loading, can now be sought in the form of the following modified Frobenius type series in terms of the variable $x_1 + py_1$ as follows:

$$U(x_1, y_1) = \sum_{n=0}^{\infty} a'_{s+n}(x_1 + py_1)^{s+2n+1} + \sum_{n=0}^{\infty} a_{s+n}(x_1 + py_1)^{s+2n}, \tag{8a}$$

$$V(x_1, y_1) = \sum_{n=0}^{\infty} b'_{s+n}(x_1 + py_1)^{s+2n+1} + \sum_{n=0}^{\infty} b_{s+n}(x_1 + py_1)^{s+2n}, \tag{8b}$$

$$W(x_1, y_1) = \sum_{n=0}^{\infty} c'_{s+n}(x_1 + py_1)^{s+2n} + \sum_{n=0}^{\infty} c_{s+n}(x_1 + py_1)^{s+2n+1}. \tag{8c}$$

Out of the various combinations, such as (a', b', c'), (a, b, c), (a', b, c), (a, b', c), (a, b, c'), (a', b', c), (a', b, c'), and (a, b', c'), only the first two groupings can produce meaningful solutions for the present class of problems, which are described below.

This step permits separation of the mode III from the modes I/II for the problem under investigation. Needless to mention, the separation of the mode III from mode I/II loadings cannot be guaranteed for every class of elastic anisotropic materials, e.g. triclinic.

4. Singular stress fields in the vicinity of a (010)|001| through-crack along |100| direction in a cubic single crystal plate subjected to mode III loading

The solution to the system of coupled partial differential equations, Equations (6), can now be assumed in the form of the following modified Frobenius type series [44,50,51] in terms of the variable $x_1 + py_1$, although unlike in [44,50,51], the variables, x_1 and y_1, are themselves not separable:

$$U(x_1, y_1) = \sum_{n=0}^{\infty} a'_{s+n}(x_1 + py_1)^{s+2n+1}, \tag{9a}$$

$$V(x_1, y_1) = \sum_{n=0}^{\infty} b'_{s+n}(x_1 + py_1)^{s+2n+1}, \tag{9b}$$

$$W(x_1, y_1) = \sum_{n=0}^{\infty} c'_{s+n}(x_1 + py_1)^{s+2n}. \tag{9c}$$

Here, the combined variable $x_1 + py_1$ represents an affine transformation in the same spirit as that by Eshelby et al. [5], Stroh [4] and Sih et al. [8], although these latter authors have employed completely different techniques. Substitution of Equations (9) into Equations (6) and equating the coefficients of $(x_1 + py_1)^{s+2n-2}$ yields the following recurrent relationship:

$$\begin{aligned}(s+2n-1)\{&(c_{12}+c_{66})a'_{s+n-1} + (c_{12}+c_{66})pb'_{s+n-1} \\ &+ (s+2n)c_{66}(1+p^2)c'_{s+n}\} + c_{11}c'_{s+n-1} = 0,\end{aligned} \tag{10}$$

which, for $n = 0$, reduces to the following:

$$c_{66}(p^2 + 1)c'_s = 0, \quad \text{for } s \neq 0,\ s \neq 1, \tag{11}$$

since $a'_{s-1} = b'_{s-1} = c'_{s-1} = 0$.

For nontrivial c'_s, Equation (11) supplies the following characteristic equation for the coupled differential equations under consideration:

$$p^2 + 1 = 0, \tag{12a}$$

leading to

$$p_{1,2} = \pm i, \tag{12b}$$

which are identical to their isotropic plate counterparts. The displacement and stress fields in the vicinity of a semi-infinite crack front can now be expressed in the same manner as that of an isotropic plate [44].

5. Singular stress fields in the vicinity of a (010)[001] through-crack propagating along [100] direction in a cubic single crystal plate under mode I/II loading

The solution to the system of coupled partial differential equations, Equations (6), can also be assumed in the form of the following modified Frobenius type series [44,52–54] in terms of the variable $x_1 + py_1$, although unlike in [44,52–54], these variables are not separable:

$$U(x_1, y_1) = \sum_{n=0}^{\infty} a_{s+n}(x_1 + py_1)^{s+2n}, \tag{13a}$$

$$V(x_1, y_1) = \sum_{n=0}^{\infty} b_{s+n}(x_1 + py_1)^{s+2n}, \tag{13b}$$

$$W(x_1, y_1) = \sum_{n=0}^{\infty} c_{s+n}(x_1 + py_1)^{s+2n+1}. \tag{13c}$$

On substitution of Equations (13) into Equations (6), and equating the coefficients of $(x_1 + py_1)^{s+2n-2}$, the following set of recurrent relationships can be derived:

$$(s+2n)(s+2n-1)(c_{11} + c_{66}p^2)a_{s+n} + c_{66}a_{s+n-1} + (s+2n)(s+2n-1)(c_{12} + c_{66})pb_{s+n} + (s+2n-1)(c_{12} + c_{66})c_{s+n-1} = 0, \tag{14a}$$

$$(s+2n)(s+2n-1)\{(c_{12} + c_{66})pa_{s+n} + (c_{11}p^2 + c_{66})b_{s+n}\} + c_{66}b_{s+n-1} + (s+2n-1)(c_{12} + c_{66})c_{s+n-1} = 0, \tag{14b}$$

which, for $n = 0$, reduce to

$$\begin{bmatrix} c_{11} + c_{66}p^2 & (c_{12} + c_{66})p \\ (c_{12} + c_{66})p & c_{11}p^2 + c_{66} \end{bmatrix} \begin{Bmatrix} a_s \\ b_s \end{Bmatrix} = \begin{Bmatrix} 0 \\ 0 \end{Bmatrix}, \quad \text{for } s \neq 0, 1. \tag{15}$$

The characteristic equations for the coupled partial differential equations are given by

$$p^4 + 2\chi p^2 + 1 = 0, \tag{16}$$

where χ is a normalized elastic parameter given by

$$\chi = \frac{(c_{11}^2 - c_{12}^2 - 2c_{12}c_{66})}{2c_{11}c_{66}}. \tag{17}$$

Eshelby et al. [5] have shown that the characteristic equation, such as Equation (16), has no real roots. Equation (16) has either (i) four complex or (ii) four imaginary roots in the nondegenerate case, depending upon χ, which in turn, depends upon the anisotropy ratio, $\bar{\lambda} = 1/\lambda$, in which λ is defined for a cubic crystal, with respect to (010)[001]x[100] cleavage system, as follows:

$$\lambda = \frac{c_{11} - c_{12}}{2c_{66}}, \tag{18}$$

which reduces to 1 for an isotropic material, such as polycrystalline metals in the absence of texturing. The physical significance of the anisotropic ratio, $\bar{\lambda}$, is that whereas the elastic constant, $c_{66}(=c_{44}=c_{55})$ represents resistance to shearing on the $\{001\}$ family of planes in the $\langle 100\rangle$ type directions, $(c_{11}-c_{12})/2$ represents the same on the $\{001\}$ family of planes in the $\langle 1\bar{1}0\rangle$ type directions [55]. Needless to say, unlike an isotropic material the resistance to shearing in a cubic single crystal is generally expected to be different in these two directions.

The normalized elastic parameter, χ, can conveniently be expressed in terms of λ as follows:

$$\chi = \lambda + \frac{c_{12}(\lambda - 1)}{c_{11}}. \tag{19}$$

It can be easily seen that

$$\chi \text{ is } \begin{cases} <1; & \text{for } \lambda < 1, \\ =1; & \text{for } \lambda = 1, \\ >1; & \text{for } \lambda > 1. \end{cases} \tag{20}$$

$\chi = 1$ represents degenerate isotropic case.

5.1. *Case (a): complex roots*

$$p_{1,2} = \xi \pm i\eta, \quad p_{3,4} = -\xi \pm i\eta, \tag{21}$$

where

$$\xi = \frac{1}{\sqrt{2}}[1 - \chi]^{1/2}, \tag{22a}$$

$$\eta = \frac{1}{\sqrt{2}}[1 + \chi]^{1/2}, \tag{22b}$$

valid for $\chi < 1$.

The detailed mathematical derivation of the solution is provided in Appendix 1. Substitution of Equation (88) in conjunction with Equation (93) into the boundary conditions on the crack-side surfaces given by Equation (4) yields four homogeneous equations, which reduce to: either

$$\cos(s-1)\pi = 0, \tag{23a}$$

or

$$\sin(s-1)\pi = 0. \tag{23b}$$

Equation (23a) contributes to the lowest non-vanishing eigenvalue, $s = 1/2$, in the range $0 < s < 1$, as required by the criterion of locally finite energy. Equation (23b) yields $s = 0$, 1, which correspond to the rigid body translation and rotation, respectively.

In order to express the asymptotic stress field in terms of the stress intensity factors $K_I(z)$ and $K_{II}(z)$, it is convenient to obtain from Equation (15)

$$c_{12}\bar{A}_i + c_{11}p_i\bar{B}_i = -c_{66}(\bar{A}_i + \bar{p}_i\bar{B}_i), \quad i = 1, \ldots, 4 \text{ (no sum on } i), \tag{24}$$

in which $\overline{p}_i$ is the complex conjugate of p_i given by Equations (21) and (22), and $\overline{B}_i$ is given by Equation (82). $\sigma_y(r, \theta, z)$ can now be obtained from Equation (81), in conjunction with Equations (82) and (1), as follows:

$$\begin{aligned}\sigma_y(r,\theta,z) = -r^{s-1}D_b(z)(ik)^s s c_{66}\Big\{&\left\{(\cos(\theta)+\xi\sin(\theta))^2+\eta^2\sin^2(\theta)\right\}^{(s-1)/2}\\ &\times[(A_1\{1+\xi H_1+\eta H_2\}-A_2\{\eta H_1-\xi H_2\})\cos((s-1)\psi)\\ &-(A_1\{\eta H_1-\xi H_2\}+A_2\{1+\xi H_1+\eta H_2\})\sin((s-1)\psi)]\\ &+\left\{(\cos(\theta)-\xi\sin(\theta))^2+\eta^2\sin^2(\theta)\right\}^{(s-1)/2}\\ &\times[(A_3\{1+\xi H_1+\eta H_2\}-A_4\{\eta H_1-\xi H_2\})\cos((s-1)\psi')\\ &-(A_3\{\eta H_1-\xi H_2\}+A_4\{1+\xi H_1+\eta H_2\})\sin((s-1)\psi')]\Big\}+O(r^{s+1}).\end{aligned} \tag{25}$$

$\sigma_x(r, \theta, z)$ can, similarly, be obtained from the other relation in Equation (15).

5.1.1. *Symmetric (mode I) loading (extension/bending)*

In this case,

$$A_1 = A_3; \quad A_2 = -A_4. \tag{26}$$

This relationship among the four unknown coefficients (eigenvectors) under mode I can also be verified by using the following boundary conditions that correspond to the far-field symmetric loading:

$$\theta = 0: \quad u_\theta = \tau_{r\theta} = \tau_{\theta z} = 0, \tag{27a}$$

$$\theta = \pi: \quad \sigma_\theta = \tau_{r\theta} = \tau_{\theta z} = 0. \tag{27b}$$

When $s = 1/2$, substitution of Equations (92b) and (88) in conjunction with Equation (93) into Equation (27) yields Equation (26). Additionally,

$$-A_1(\eta + H_2) + A_2(\xi + H_1) = 0,$$

which yields

$$\frac{A_2}{A_1} = -\frac{\eta}{\xi}\frac{(c_{11}+c_{12})}{(c_{11}-c_{12})}. \tag{28}$$

Finally, on substitution of Equations (26) and (28) into the expressions for displacements and stresses, and by defining the mode I stress intensity factor, $K_I(z)$, as

$$K_I(z) = \sqrt{2}D_b(z)(ik)^{1/2}(c_{11}+c_{12})A_1, \tag{29}$$

the components of in-plane displacements and stresses, in the vicinity of a semi-infinite crack front, under symmetric far-field loading, can be expressed as follows:

$$u(r,\theta,z)=\frac{K_{\mathrm{I}}(z)}{(c_{11}^2-c_{12}^2)}\sqrt{\frac{r}{2}}\Bigg[\left\{(\cos\theta+\xi\sin\theta)^2+\eta^2\sin^2\theta\right\}^{1/4}\times\left\{(c_{11}-c_{12})\cos(\psi/2)-(c_{11}+c_{12})\frac{\eta}{\xi}\sin(\psi/2)\right\}+\left\{(\cos\theta-\xi\sin\theta)^2+\eta^2\sin^2\theta\right\}^{1/4}\times\left\{(c_{11}-c_{12})\cos(\psi'/2)+(c_{11}+c_{12})\frac{\eta}{\xi}\sin(\psi'/2)\right\}\Bigg], \tag{30a}$$

$$v(r,\theta,z)=\frac{K_{\mathrm{I}}(z)}{(c_{11}^2-c_{12}^2)}\sqrt{\frac{r}{2}}\Bigg[\left\{(\cos\theta+\xi\sin\theta)^2+\eta^2\sin^2\theta\right\}^{1/4}\times\left\{-\frac{(c_{11}^2-c_{12}^2)}{2c_{66}\xi}\cos(\psi/2)+2c_{11}\eta\sin(\psi/2)\right\}+\left\{(\cos\theta-\xi\sin\theta)^2+\eta^2\sin^2\theta\right\}^{1/4}\times\left\{\frac{(c_{11}^2-c_{12}^2)}{2c_{66}\xi}\cos(\psi'/2)+2c_{11}\eta\sin(\psi'/2)\right\}\Bigg], \tag{30b}$$

$$\sigma_x(r,\theta,z)=\frac{K_{\mathrm{I}}(z)}{2\sqrt{2r}}\Bigg[\left\{(\cos\theta+\xi\sin\theta)^2+\eta^2\sin^2\theta\right\}^{-1/4}\left\{\cos(\psi/2)+\frac{\eta}{\xi}\sin(\psi/2)\right\}+\left\{(\cos\theta-\xi\sin\theta)^2+\eta^2\sin^2\theta\right\}^{-1/4}\left\{\cos(\psi'/2)-\frac{\eta}{\xi}\sin(\psi'/2)\right\}\Bigg], \tag{31a}$$

$$\sigma_y(r,\theta,z)=\frac{K_{\mathrm{I}}(z)}{2\sqrt{2r}}\Bigg[\left\{(\cos\theta+\xi\sin\theta)^2+\eta^2\sin^2\theta\right\}^{-1/4}\left\{\cos(\psi/2)-\frac{\eta}{\xi}\sin(\psi/2)\right\}+\left\{(\cos\theta-\xi\sin\theta)^2+\eta^2\sin^2\theta\right\}^{-1/4}\left\{\cos(\psi'/2)+\frac{\eta}{\xi}\sin(\psi'/2)\right\}\Bigg], \tag{31b}$$

$$\tau_{xy}(r,\theta,z)=-\frac{K_{\mathrm{I}}(z)}{2\sqrt{2r\xi}}\Bigg[\left\{(\cos\theta+\xi\sin\theta)^2+\eta^2\sin^2\theta\right\}^{-1/4}\cos(\psi/2)-\left\{(\cos\theta-\xi\sin\theta)^2+\eta^2\sin^2\theta\right\}^{-1/4}\cos(\psi'/2)\Bigg]. \tag{31c}$$

5.1.2. *Skew-symmetric (mode II) loading (sliding shear/twisting)*

In this case,

$$A_1=-A_3;\quad A_2=A_4. \tag{32}$$

This relationship among the four unknown coefficients (eigenvectors) under mode II can also be verified by using the following boundary conditions that correspond to the far-field antisymmetric loading:

$$\theta = 0: \quad u_r = \sigma_\theta = \tau_{\theta z} = 0, \tag{33a}$$

$$\theta = \pi: \quad \sigma_\theta = \tau_{r\theta} = \tau_{\theta z} = 0. \tag{33b}$$

When $s = 1/2$, substitution of Equations (92a) and (88) in conjunction with Equation (93) into Equation (33) yields Equation (32). Additionally,

$$A_2(1 + \xi H_1 + \eta H_2) + A_1(\eta H_1 - \xi H_2) = 0,$$

which yields

$$\frac{A_2}{A_1} = \frac{4c_{11}c_{66}\xi\eta}{(c_{11}^2 - c_{12}^2)}. \tag{34}$$

Finally, on substitution of Equations (32) and (34) into the expressions for displacements and stresses, and by defining the mode II stress intensity factor, $K_{II}(z)$, as

$$K_{II}(z) = 2\sqrt{2}D_b(z)(ik)^{1/2}\xi c_{66}A_1, \tag{35}$$

the components of in-plane displacements and stresses, in the vicinity of a semi-infinite crack front, under skew-symmetric far-field loading, can be expressed as follows:

$$\begin{aligned} u(r,\theta,z) = \frac{K_{II}(z)}{(c_{11}^2 - c_{12}^2)}\sqrt{\frac{r}{2}}\Bigg[& \left\{(\cos\theta + \xi\sin\theta)^2 + \eta^2\sin^2\theta\right\}^{1/4} \\ & \times \left\{\frac{(c_{11}^2 - c_{12}^2)}{2c_{66}\xi}\cos(\psi/2) + 2c_{11}\eta\sin(\psi/2)\right\} \\ & - \left\{(\cos\theta - \xi\sin\theta)^2 + \eta^2\sin^2\theta\right\}^{1/4} \\ & \times \left\{-\frac{(c_{11}^2 - c_{12}^2)}{2c_{66}\xi}\cos(\psi'/2) + 2c_{11}\eta\sin(\psi'/2)\right\}\Bigg], \end{aligned} \tag{36a}$$

$$\begin{aligned} v(r,\theta,z) = -\frac{K_{II}(z)}{(c_{11}^2 - c_{12}^2)}\sqrt{\frac{r}{2}}\Bigg[& \left\{(\cos\theta + \xi\sin\theta)^2 + \eta^2\sin^2\theta\right\}^{1/4}\left\{(c_{11} - c_{12})\cos(\psi/2)\right. \\ & \left. + (c_{11} + c_{12})\frac{\eta}{\xi}\sin(\psi/2)\right\} + \left\{(\cos\theta - \xi\sin\theta)^2 + \eta^2\sin^2\theta\right\}^{1/4} \\ & \times \left\{(c_{11} - c_{12})\cos(\psi'/2) - (c_{11} + c_{12})\frac{\eta}{\xi}\sin(\psi'/2)\right\}\Bigg], \end{aligned} \tag{36b}$$

$$\sigma_x(r,\theta,z)=\frac{K_{II}(z)}{2\sqrt{2r}}\left[\left\{(\cos\theta+\xi\sin\theta)^2+\eta^2\sin^2\theta\right\}^{-1/4}\left\{\frac{(\eta^2-\xi^2)}{\xi}\cos(\psi/2)-2\eta\sin(\psi/2)\right\}\right.$$
$$\left.-\left\{(\cos\theta-\xi\sin\theta)^2+\eta^2\sin^2\theta\right\}^{-1/4}\left\{\frac{(\eta^2-\xi^2)}{\xi}\cos(\psi'/2)+2\eta\sin(\psi'/2)\right\}\right], \tag{37a}$$

$$\sigma_y(r,\theta,z)=\frac{K_{II}(z)}{2\sqrt{2r\xi}}\left[\left\{(\cos\theta+\xi\sin\theta)^2+\eta^2\sin^2\theta\right\}^{-1/4}\cos(\psi/2)\right.$$
$$\left.+\left\{(\cos\theta-\xi\sin\theta)^2+\eta^2\sin^2\theta\right\}^{-1/4}\cos(\psi'/2)\right], \tag{37b}$$

$$\tau_{xy}(r,\theta,z)=\frac{K_{II}(z)}{2\sqrt{2r}}\left[\left\{(\cos\theta+\xi\sin\theta)^2+\eta^2\sin^2\theta\right\}^{-1/4}\left\{\cos(\psi/2)+\frac{\eta}{\xi}\sin(\psi/2)\right\}\right.$$
$$\left.+\left\{(\cos\theta-\xi\sin\theta)^2+\eta^2\sin^2\theta\right\}^{-1/4}\left\{\cos(\psi'/2)-\frac{\eta}{\xi}\sin(\psi'/2)\right\}\right]. \tag{37c}$$

It may be noted that in the expressions for displacements and stresses, given by Equations (30) and (31), respectively, under mode I loading, there is a coupling between $\cos(\psi/2)$ and $\sin(\psi/2)$ (and similar coupling between $\cos(\psi'/2)$ and $\sin(\psi'/2)$) terms, except for τ_{xy}, given by Equation (31c). Similarly, in the expressions for displacements and stresses, given by Equations (36) and (37), respectively, under mode II loading, there is a coupling between $\cos(\psi/2)$ and $\sin(\psi/2)$ (and similar coupling between $\cos(\psi'/2)$ and $\sin(\psi'/2)$) terms, except for σ_y, given by Equation (37b). Appendix 4 presents a comparison of the solution involving complex roots with its isotropic counterpart, and concludes that the expressions for ρ and ψ look different from their isotropic counterparts. This is especially true for ψ at $x=0$. The significance of this, albeit being semi-qualitatively and indirectly inferred at this stage, is that for $\chi<1$ (or $\lambda<1$), the through (010)[001] crack considered here is, unlike its isotropic counterpart, more likely to deviate from its original plane (010) and original propagation direction [100], because of this coupling, which arises from the complex roots. It can then be inferred that the (010)[001] is not an easy cleavage system for cubic crystals with anisotropic ratio, $\bar{\lambda}>1$. It may, however, be remarked that the existing Griffith–Irwin approach cannot by itself predict this type of crack kinking (deviation) behavior in single crystals, and an additional conceptual-cum-analytical tool must be developed to incorporate the lattice discreteness and the associated energy barrier. This is because Griffith's criterion is "not really a fracture criterion but only a necessary condition for fracture" [28]. Secondly, and more important, atomistic modeling of a crack requires consideration of both the long range elastic interactions and the short range chemical reactions. The Griffith–Irwin approach does not take the latter into account, and that is why atomistic simulation employs empirical interaction models (e.g. Stillinger–Weber potential, Tersoff potential, etc.). For example, Perez and Gumbsch [28] have investigated the cleavage anisotropy in silicon single crystals by making use of total-energy pseudopotential calculations in the context of the density functional theory. In the present study,

this is accomplished in the form of the LCD energy barrier (see Sections 8 and 9 below).

5.2. *Case (b): imaginary roots*

The four imaginary roots of Equation (16) are given by

$$p_{1,2} = \pm i(\xi' + \eta'), \quad p_{3,4} = \pm i(\xi' - \eta'), \tag{38}$$

where

$$\xi' = \frac{1}{\sqrt{2}}[1 + \chi]^{1/2}, \tag{39a}$$

$$\eta' = \frac{1}{\sqrt{2}}[-1 + \chi]^{1/2}, \tag{39b}$$

valid for $\chi > 1$.

The detailed mathematical derivation of the solution is provided in Appendix 2. Substitution of Equation (101) in conjunction with Equation (93) into the boundary conditions on the crack-side surfaces given by Equaiton (4) yield four homogeneous equations, which reduce to either

$$\cos(s-1)\pi = 0, \tag{40a}$$

or

$$\sin(s-1)\pi = 0, \tag{40b}$$

Equation (40a) contributes to the lowest non-vanishing eigenvalue, $s = 1/2$, in the range $0 < s < 1$, as required by the criterion of locally finite energy. Equation (40b) yields $s = 0$, 1, which correspond to the rigid body translation and rotation, respectively. For $s = 1/2$, $\cos((s-1)\psi_1(\theta))$, $\sin((s-1)\psi_1(\theta))$, etc., in Equation (101) can be obtained in terms of $\cos(\psi_1(\theta))$, $\sin(\psi_1(\theta))$ given by Equation (99).

5.2.1. *Symmetric (mode I) loading (extension/bending)*

For $s = 1/2$,

$$A_2 = A_4 = 0; \tag{41}$$

and

$$\frac{A_3}{A_1} = -\frac{\{c_{11}(\xi' - \eta') + c_{12}(\xi' + \eta')\}}{\{c_{11}(\xi' + \eta') + c_{12}(\xi' - \eta')\}}. \tag{42}$$

Finally, on substitution of Equations (41) and (42) into the expressions for displacements and stresses, and by defining the mode I stress intensity factor, $K_I(z)$, as

$$K_I(z) = \sqrt{2} D_b(z)(ik)^{1/2} \frac{c_{66}\eta'}{(c_{12} + c_{66})} \{c_{11}(\xi' - \eta') + c_{12}(\xi' - \eta')\} A_1, \tag{43}$$

the components of in-plane displacements and stresses, in the vicinity of a semi-infinite crack front, under symmetric far-field loading, can be expressed as follows:

$$u(r,\theta,z)=\frac{K_I(z)}{(c_{11}^2-c_{12}^2)\eta'}\sqrt{\frac{r}{2}}\Big[\{\cos^2\theta+(\xi'+\eta')^2\sin^2\theta\}^{1/4}\times\{c_{11}(\xi'+\eta')+c_{12}(\xi'-\eta')\}\cos(\psi_1/2)-\{\cos^2\theta+(\xi'-\eta')^2\sin^2\theta\}^{1/4}\times\{c_{11}(\xi'-\eta')+c_{12}(\xi'+\eta')\}\cos(\psi_1'/2)\Big], \tag{44a}$$

$$v(r,\theta,z)=\frac{K_I(z)}{(c_{11}^2-c_{12}^2)\eta'}\sqrt{\frac{r}{2}}\Big[-\{\cos^2\theta+(\xi'+\eta')^2\sin^2\theta\}^{1/4}\{c_{12}+c_{11}(\xi'-\eta')^2\}\sin(\psi_1/2)+\{\cos^2\theta+(\xi'-\eta')^2\sin^2\theta\}^{1/4}\{c_{12}+c_{11}(\xi'+\eta')^2\}\sin(\psi_1'/2)\Big], \tag{44b}$$

$$\sigma_x(r,\theta,z)=\frac{K_I(z)}{2\sqrt{2r\eta'}}\Big[\{\cos^2\theta+(\xi'+\eta')^2\sin^2\theta\}^{-1/4}(\xi'+\eta')\cos(\psi_1/2)-\{\cos^2\theta+(\xi'-\eta')^2\sin^2\theta\}^{-1/4}(\xi'-\eta')\cos(\psi_1'/2)\Big], \tag{45a}$$

$$\sigma_y(r,\theta,z)=-\frac{K_I(z)}{2\sqrt{2r\eta'}}\Big[\{\cos^2\theta+(\xi'+\eta')^2\sin^2\theta\}^{-1/4}(\xi'-\eta')\cos(\psi_1/2)-\{\cos^2\theta+(\xi'-\eta')^2\sin^2\theta\}^{-1/4}(\xi'+\eta')\cos(\psi_1'/2)\Big], \tag{45b}$$

$$\tau_{xy}(r,\theta,z)=\frac{K_I(z)}{2\sqrt{2r\eta'}}\Big[\{\cos^2\theta+(\xi'+\eta')^2\sin^2\theta\}^{-1/4}\sin(\psi_1/2)-\{\cos^2\theta+(\xi'-\eta')^2\sin^2\theta\}^{-1/4}\sin(\psi_1'/2)\Big]. \tag{45c}$$

5.2.2. *Skew-symmetric (mode II) loading (sliding shear/twisting)*

For $s=1/2$,

$$A_1=A_3=0, \tag{46}$$

and

$$\frac{A_4}{A_2}=-\frac{(\xi'-\eta')\{c_{11}(\xi'-\eta')+c_{12}(\xi'+\eta')\}}{(\xi'+\eta')\{c_{11}(\xi'+\eta')+c_{12}(\xi'-\eta')\}}. \tag{47}$$

Finally, on substitution of Equations (46) and (47) into the expressions for displacements and stresses, and by defining the mode II stress intensity factor, $K_{II}(z)$, as

$$K_{II}(z)=\sqrt{2}D_b(z)(ik)^{1/2}\frac{c_{66}\eta'}{(c_{12}+c_{66})(\xi'+\eta')}\{c_{11}(\xi'-\eta')+c_{12}(\xi'+\eta')\}A_2, \tag{48}$$

the components of in-plane displacements and stresses, in the vicinity of a semi-infinite crack front, under skew-symmetric far-field loading, can be expressed as follows:

$$u(r,\theta,z)=\frac{K_{II}(z)}{(c_{11}^2-c_{12}^2)\eta'}\sqrt{\frac{r}{2}}\Bigg[\left\{\cos^2\theta+(\xi'+\eta')^2\sin^2\theta\right\}^{1/4}\left\{c_{11}(\xi'+\eta')^2+c_{12}\right\}\sin(\psi_1/2)$$
$$-\left\{\cos^2\theta+(\xi'-\eta')^2\sin^2\theta\right\}^{1/4}\left\{c_{11}(\xi'-\eta')^2+c_{12}\right\}\sin(\psi_1'/2)\Bigg], \tag{49a}$$

$$v(r,\theta,z)=\frac{K_{II}(z)}{(c_{11}^2-c_{12}^2)\eta'}\sqrt{\frac{r}{2}}\Bigg[\left\{\cos^2\theta+(\xi'+\eta')^2\sin^2\theta\right\}^{1/4}$$
$$\times\left\{c_{11}(\xi'-\eta')+c_{12}(\xi'+\eta')\right\}\cos(\psi_1/2)-\left\{\cos^2\theta+(\xi'-\eta')^2\sin^2\theta\right\}^{1/4}$$
$$\times\left\{c_{11}(\xi'+\eta')+c_{12}(\xi'-\eta')\right\}\cos(\psi_1'/2)\Bigg], \tag{49b}$$

$$\sigma_x(r,\theta,z)=-\frac{K_{II}(z)}{2\sqrt{2r}\eta'}\Bigg[\left\{\cos^2\theta+(\xi'+\eta')^2\sin^2\theta\right\}^{-1/4}(\xi'+\eta')^2\sin(\psi_1/2)$$
$$-\left\{\cos^2\theta+(\xi'-\eta')^2\sin^2\theta\right\}^{-1/4}(\xi'-\eta')^2\sin(\psi_1'/2)\Bigg], \tag{50a}$$

$$\sigma_y(r,\theta,z)=\frac{K_{II}(z)}{2\sqrt{2r}\eta'}\Bigg[\left\{\cos^2\theta+(\xi'+\eta')^2\sin^2\theta\right\}^{-1/4}\sin(\psi_1/2)$$
$$-\left\{\cos^2\theta+(\xi'-\eta')^2\sin^2\theta\right\}^{-1/4}\sin(\psi_1'/2)\Bigg], \tag{50b}$$

$$\tau_{xy}(r,\theta,z)=\frac{K_{II}(z)}{2\sqrt{2r}\eta'}\Bigg[\left\{\cos^2\theta+(\xi'+\eta')^2\sin^2\theta\right\}^{-1/4}(\xi'+\eta')\cos(\psi_1/2)$$
$$-\left\{\cos^2\theta+(\xi'-\eta')^2\sin^2\theta\right\}^{-1/4}(\xi'-\eta')\cos(\psi_1'/2)\Bigg]. \tag{50c}$$

It may be noted that in the expressions for displacements and stresses, given by Equations (44) and (45), respectively, under mode I loading, there is no coupling between $\cos(\psi/2)$ and $\sin(\psi/2)$ (and similar absence of coupling between $\cos(\psi'/2)$ and $\sin(\psi'/2)$) terms. The same is true in the expressions for displacements and stresses, given by Equations (49) and (50), respectively, under mode II loading. Appendix 4 presents a comparison of the solution involving imaginary roots with its isotropic counterpart, and concludes that the expressions for ρ and ψ look similar to their isotropic counterparts. This is especially true for ψ at $x=0$. The significance of this, albeit being qualitatively and indirectly inferred, is that for $\chi>1$ (or $\lambda>1$), the through (010)[001] crack considered here is, like its isotropic counterpart, more likely to propagate in its original plane (010) and direction [100], because of this absence of coupling, which arises due to the imaginary roots. It can then be inferred that the (010)[001] is an easy cleavage system in cubic crystals with anisotropic ratio, $\bar{\lambda}<1$. As has been remarked earlier, this absence of crack kinking (deviation) cannot be

predicted by the existing Griffith-Irwin approach, and will need additional analysis (see Sections 8 and 9 below).

Finally, it may be noted that the above expressions for displacements, given by Equations (30), (36), (44) and (49), and stresses, given by Equations (31), (37), (45) and (50), reduce to their two-dimensional counterparts (see, for example, Sih et al. [8]).

5.2.3. *Plate surface boundary conditions*

(1) The stress field in the vicinity of the front of a semi-infinite crack under in-plane extension (mode I)/shear (mode II) can be recovered if in Equations (29) and (43) or Equations (35) and (48)

$$D_b(z) = D_{bs}(z) = D_2 \cos(kz). \tag{51}$$

By using the stress-free boundary condition on the plate surfaces, given by Equation (3a), the general form of $D_{bs}(z)$ can be obtained as

$$D_{bs}(z) = \sum_{n=0}^{\infty} D_{2n} \cos\left(\frac{(2n+1)}{2h}\pi z\right). \tag{52}$$

Hence, $K_I = K_{Is}$ and $K_{II} = K_{IIs}$ represent symmetric stress intensity factors. If the odd functions are selected from $D_b(z)$, it can yield the out-of-plane bending (mode I)/twisting (mode II) case given by

$$D_b(z) = D_{ba}(z) = D_1 \sin(kz). \tag{53}$$

$D_{ba}(z)$ that satisfies the stress-free condition on the plate surfaces is given by

$$D_{ba}(z) = \sum_{n=1}^{\infty} D_{1n} \sin\left(\frac{n\pi}{h} z\right). \tag{54}$$

Here $K_I = K_{Ia}$ and $K_{II} = K_{IIa}$ are anti-symmetric stress intensity factors.

(2, 3) Satisfaction of fixed and lubricated boundary conditions, given by Equations (3b) and (3c), respectively, on the plate faces results in identical expressions for the displacement and singular stress fields as above.

6. Singular stress fields in the vicinity of a $(\bar{1}10)[001]$ through-crack propagating along [110] direction

The cleavage plane considered is $(\bar{1}10)$, which belongs to the {110} family of planes (Figure 2). Here, the z-axis is placed along the straight crack front, [001], whereas the coordinates x' [110], y' [$\bar{1}$10] are used to define the directions along the length of the crack (propagation direction) and the direction transverse to it, respectively, in the middle plane of the plate. u, v and w represent the components of the displacements in the x', y' and z directions, respectively.

The stress–strain relationships for a cubic single crystal are given by

$$\begin{Bmatrix} \sigma'_x \\ \sigma'_y \\ \sigma_z \\ \tau_{yz} \\ \tau_{xz} \\ \tau'_{xy} \end{Bmatrix} = \begin{bmatrix} c'_{11} & c'_{12} & c_{12} & 0 & 0 & 0 \\ c'_{12} & c'_{11} & c_{12} & 0 & 0 & 0 \\ c_{12} & c_{12} & c_{11} & 0 & 0 & 0 \\ 0 & 0 & 0 & c_{66} & 0 & 0 \\ 0 & 0 & 0 & 0 & c_{66} & 0 \\ 0 & 0 & 0 & 0 & 0 & c'_{66} \end{bmatrix} \begin{Bmatrix} \varepsilon'_x \\ \varepsilon'_y \\ \varepsilon_z \\ \gamma_{yz} \\ \gamma_{xz} \\ \gamma'_{xy} \end{Bmatrix}, \tag{55}$$

where c'_{11}, c'_{12}, and c'_{66} denote the elastic stiffnesses with respect to the rotated coordinate system x', y' (obtained by rotation of 45° about the z-axis). s'_{11}, s'_{12} and s'_{66} denote the corresponding elastic compliances. The three equilibrium equations for a linear elastic cubic solid can now be expressed in terms of the displacement components, u, v and w, as follows:

$$c'_{11}\frac{\partial^2 u}{\partial x^2} + c'_{66}\frac{\partial^2 u}{\partial y^2} + c_{66}\frac{\partial^2 u}{\partial z^2} + (c'_{12} + c'_{66})\frac{\partial^2 v}{\partial x \partial y} + (c_{12} + c_{66})\frac{\partial^2 w}{\partial x \partial z} = 0, \tag{56a}$$

$$(c'_{12} + c'_{66})\frac{\partial^2 u}{\partial x \partial y} + c'_{66}\frac{\partial^2 v}{\partial x^2} + c'_{11}\frac{\partial^2 v}{\partial y^2} + c_{66}\frac{\partial^2 v}{\partial z^2} + (c_{12} + c_{66})\frac{\partial^2 w}{\partial y \partial z} = 0, \tag{56b}$$

$$(c_{12} + c_{66})\frac{\partial^2 u}{\partial x \partial z} + (c_{12} + c_{66})\frac{\partial^2 v}{\partial y \partial z} + c_{66}\frac{\partial^2 w}{\partial x^2} + c_{66}\frac{\partial^2 w}{\partial y^2} + c_{11}\frac{\partial^2 w}{\partial z^2} = 0, \tag{56c}$$

in which

$$\begin{aligned} c'_{11} &= \frac{1}{2}(c_{11} + c_{12} + 2c_{66}), \quad c'_{12} = \frac{1}{2}(c_{11} + c_{12} - 2c_{66}), \\ c'_{66} &= \frac{1}{2}(c_{11} - c_{12}). \end{aligned} \tag{57}$$

The inverse anisotropic ratio, λ', with respect to the $(\bar{1}10)[001] \times [110]$ cleavage system defined above is now defined as

$$\lambda' = \frac{c'_{11} - c'_{12}}{2c'_{66}} = \frac{2c_{66}}{(c_{11} - c_{12})} = \bar{\lambda} = \frac{1}{\lambda}, \tag{58}$$

where λ' is interestingly enough the anisotropic ratio ($\bar{\lambda}$) defined on the basis of the elastic constants with respect to the cube edges.

The corresponding normalized elastic parameter, χ', is given by

$$\chi' = \frac{\lambda'(c'_{11} + c'_{12}) - c'_{12}}{c'_{11}} = \lambda' + \frac{c'_{12}(\lambda' - 1)}{c'_{11}}. \tag{59}$$

It can be seen as before that

$$\chi' \text{ is } \begin{cases} <1; & \text{for } \lambda' < 1, \\ =1; & \text{for } \lambda' = 1, \\ >1; & \text{for } \lambda' > 1. \end{cases} \tag{60}$$

$\chi' = 1$ represents degenerate isotropic case.

Following the same procedure as for the (010)[001] cleavage system, it can easily be seen that the solution for the antiplane shear (mode III) loading remains unaltered. As for the extension-bending (mode I) and in-plane shear-twisting (mode II) loadings, it can easily be seen that $\bar{\lambda} = \lambda' > 1$, which is equivalent to $\lambda < 1$, yields imaginary roots. This implies that for cubic crystals with $\bar{\lambda} > 1$, the $(\bar{1}10)[001]$ is an easy cleavage system. Conversely, $\bar{\lambda} = \lambda' < 1$, which is equivalent to $\lambda > 1$, yields complex roots, implying that the (010)[001] crack, with the [100] propagation direction, is the easy cleavage system as compared to the $(\bar{1}10)[001]$ crack, the propagation direction being [110] in the latter case.

7. Singular stress fields in the vicinity of a $(1\bar{1}0)[110]$ through-crack propagating along [001] direction

The cleavage plane considered is $(1\bar{1}0)$, which belongs to the {110} family of planes (not shown). Here, the z-axis is placed along the straight crack front, [110], whereas the coordinates x' [001], y' $[1\bar{1}0]$ are used to define the directions along the length of the crack (propagation direction) and the direction transverse to it, respectively, in the middle plane of the plate. u, v and w represent the components of the displacements in the x', y' and z directions, respectively.

The stress–strain relationships for a cubic single crystal are given by

$$\begin{Bmatrix} \sigma_x \\ \sigma'_y \\ \sigma'_z \\ \tau'_{yz} \\ \tau_{xz} \\ \tau_{xy} \end{Bmatrix} = \begin{bmatrix} c_{11} & c_{12} & c_{12} & 0 & 0 & 0 \\ c_{12} & c'_{11} & c'_{12} & 0 & 0 & 0 \\ c_{12} & c'_{12} & c'_{11} & 0 & 0 & 0 \\ 0 & 0 & 0 & c'_{66} & 0 & 0 \\ 0 & 0 & 0 & 0 & c_{66} & 0 \\ 0 & 0 & 0 & 0 & 0 & c_{66} \end{bmatrix} \begin{Bmatrix} \varepsilon_x \\ \varepsilon'_y \\ \varepsilon'_z \\ \gamma'_{yz} \\ \gamma_{xz} \\ \gamma_{xy} \end{Bmatrix}, \tag{61}$$

where c'_{11}, c'_{12} and c'_{66} denote the elastic stiffnesses with respect to the rotated coordinate system y', z' (obtained by rotation of 45° about the x-axis). s'_{11}, s'_{12} and s'_{66} denote the corresponding elastic compliances. The three equilibrium equations for a linear elastic cubic solid can now be expressed in terms of the displacement components, u, v and w, as follows:

$$c_{11}\frac{\partial^2 u}{\partial x^2} + c_{66}\frac{\partial^2 u}{\partial y^2} + c_{66}\frac{\partial^2 u}{\partial z^2} + (c_{12} + c_{66})\frac{\partial^2 v}{\partial x \partial y} + (c_{12} + c_{66})\frac{\partial^2 w}{\partial x \partial z} = 0, \tag{62a}$$

$$(c_{12} + c_{66})\frac{\partial^2 u}{\partial x \partial y} + c_{66}\frac{\partial^2 v}{\partial x^2} + c'_{11}\frac{\partial^2 v}{\partial y^2} + c'_{66}\frac{\partial^2 v}{\partial z^2} + (c'_{12} + c'_{66})\frac{\partial^2 w}{\partial y \partial z} = 0, \tag{62b}$$

$$(c_{12} + c_{66})\frac{\partial^2 u}{\partial x \partial z} + (c'_{12} + c'_{66})\frac{\partial^2 v}{\partial y \partial z} + c_{66}\frac{\partial^2 w}{\partial x^2} + c'_{66}\frac{\partial^2 w}{\partial y^2} + c'_{11}\frac{\partial^2 w}{\partial z^2} = 0, \tag{62c}$$

where c'_{11}, c'_{12} and c'_{66} are given by Equations (57). The asymptotic solution for mode III loading is briefly discussed in Appendix 3. For mode I/II loadings, the

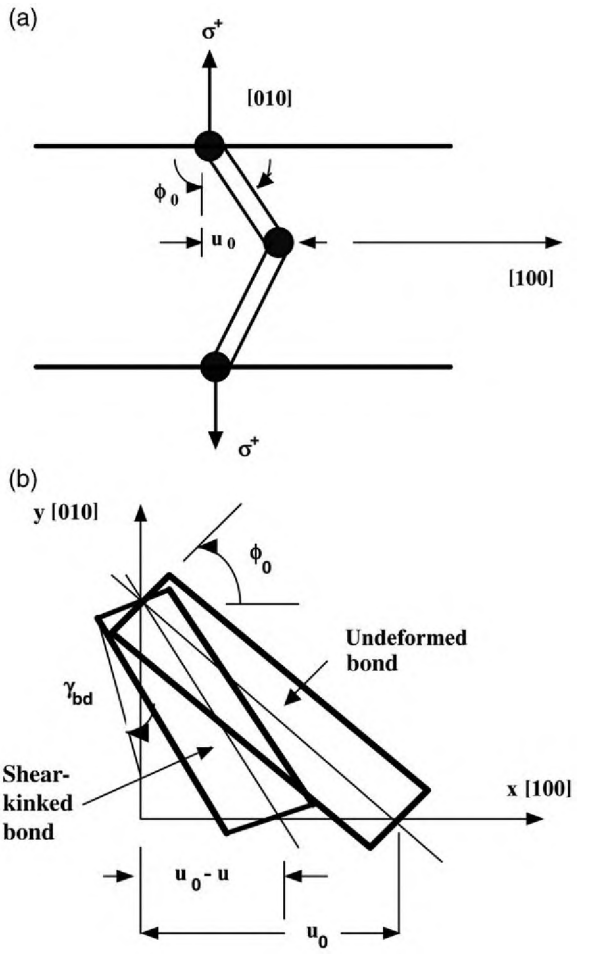

Figure 3. Schematics of (a) misaligned bonds under tension; (b) shear kinking of a bond and associated rotational/shear instability.

characteristic equations for the coupled partial differential equations, Equations (62) are given as before,

$$\begin{bmatrix} c_{11} + c_{66}p^2 & (c_{12} + c_{66})\,p \\ (c_{12} + c_{66})\,p & c'_{11}p^2 + c_{66} \end{bmatrix} \begin{Bmatrix} a_s \\ b_s \end{Bmatrix} = \begin{Bmatrix} 0 \\ 0 \end{Bmatrix}, \quad \text{for } s \neq 0,\ 1 \tag{63}$$

leading to

$$p^4 + 2\chi'' p^2 + \frac{c_{11}}{c'_{11}} = 0, \tag{64}$$

where χ'' is a normalized elastic parameter given by

$$\chi'' = \frac{(c_{11}c'_{11} - c_{12}^2 - 2c_{12}c_{66})}{2c'_{11}c_{66}}. \tag{65}$$

The inverse anisotropic ratio, λ'', with respect to the $(1\bar{1}0)[110] \times [001]$ cleavage system is now defined as

$$\lambda'' = \frac{\sqrt{c_{11}c'_{11}} - c_{12}}{2c_{66}}. \tag{66}$$

The corresponding normalized elastic parameter, χ'', is then given by

$$\chi'' = \frac{\lambda''\left(\sqrt{c_{11}c'_{11}} + c_{12}\right) - c_{12}}{c'_{11}} = \sqrt{\frac{c_{11}}{c'_{11}}}\lambda'' + \frac{c_{12}(\lambda'' - 1)}{c'_{11}}. \tag{67}$$

It can be seen that

$$\chi'' \text{ is } \begin{cases} < \sqrt{\dfrac{c_{11}}{c'_{11}}}; & \text{for } \lambda'' < 1, \\ = \sqrt{\dfrac{c_{11}}{c'_{11}}} = 1; & \text{for } \lambda'' = 1, \\ > \sqrt{\dfrac{c_{11}}{c'_{11}}}; & \text{for } \lambda'' > 1. \end{cases} \tag{68}$$

Equation (64) has either (a) four complex or (b) four imaginary roots, depending on whether

$$\text{(a) } \chi'' < \sqrt{\frac{c_{11}}{c'_{11}}}, \quad \text{or} \quad \text{(b) } \chi'' > \sqrt{\frac{c_{11}}{c'_{11}}}.$$

$\chi'' = \sqrt{\dfrac{c_{11}}{c'_{11}}} = 1$ represents the degenerate isotropic material case, for which the solution is available in Chaudhuri and Xie [44].

7.1. *Case (a): complex roots*

The four complex roots of Equation (64) can be written as follows:

$$p_{1,2} = \xi'' \pm i\eta'', \quad p_{3,4} = -\xi'' \pm i\eta'', \tag{69a, b}$$

where

$$\xi'' = \frac{1}{\sqrt{2}}\left[\left(\frac{c_{11}}{c'_{11}}\right)^{1/2} - \chi''\right]^{1/2}, \tag{70a}$$

$$\eta'' = \frac{1}{\sqrt{2}}\left[\left(\frac{c_{11}}{c'_{11}}\right)^{1/2} + \chi''\right]^{1/2}, \tag{70b}$$

valid for $\chi'' < \sqrt{c_{11}/c'_{11}}$. The final solution is provided in Appendix 3.

7.2. *Case (b): imaginary roots*

The four imaginary roots of Equation (64) are given by

$$p_{1,2} = \pm i(\xi''' + \eta'''), \quad p_{3,4} = \pm i(\xi''' - \eta'''), \tag{71a}$$

where

$$\xi''' = \frac{1}{\sqrt{2}}\left[\left(\frac{c_{11}}{c'_{11}}\right)^{1/2} + \chi''\right]^{1/2}, \tag{72a}$$

$$\eta''' = \frac{1}{\sqrt{2}}\left[-\left(\frac{c_{11}}{c'_{11}}\right)^{1/2} + \chi''\right]^{1/2}, \tag{72b}$$

valid for $\chi'' > \sqrt{c_{11}/c'_{11}}$. Again, the final solution is provided in Appendix 3.

Following the same procedure as for the (010)[001] cleavage system, it can easily be seen that the solution for the antiplane shear (mode III) loading is slightly altered (see Appendix 3). As for the extension-bending (mode I) and in-plane shear-twisting (mode II) loadings, it can easily be seen that $\lambda'' > 1$ (or $\chi'' > \sqrt{c_{11}/c'_{11}}$) yields imaginary roots. This implies that for cubic crystals with $\lambda'' > 1$, $(1\bar{1}0)[110]$ is an easy cleavage system. Conversely, $\lambda'' < 1$ yields complex roots, implying that the $(1\bar{1}0)[110]$ with the [001] propagation direction, is difficult to be achieved in actual experiments. This is in agreement with Refs. [7,8] of Perez and Gumbsch [28] for monocrystalline Si.

8. Lattice crack deviation (LCD) energy barrier

As has been mentioned earlier, the lattice trapping phenomenon is responsible for keeping a crack stable in a "difficult" cleavage plane/direction, and not permitting it to propagate in that plane/direction "until loads somewhat larger than the Griffith load are reached" [28]. Perfectly brittle cleavage (i.e. absence of dislocation activity in the crack front region) in monocrystalline semiconductor materials such as Si and GaAs is expected to involve only the breaking of atomic bonds. In view of the discrete nature of the crystal lattice, brittle fracture in such materials would be affected by the lattice trapping phenomenon [39]. According to Thompson et al. [39], a somewhat higher load, K^{+}, as compared to its Griffith counterpart, K_G, would be required to advance the crack (bond breaking), while the crack closure (bond healing) can be achieved at a somewhat lower load, K^{-}. The lattice trapping regime, where a crack of given length remains stable at one particular position in the lattice [28], is defined as a range of applied load (stress intensity factor). The experimentally observed deflected crack would propagate under mixed mode (i.e., opening and shear mode) and its relationship with a lattice related phenomenon has, however, not been studied in the literature [28]. This would necessitate introduction of a new concept of the lattice crack deviation (LCD) parameter, and its quantification, which is the primary focus of what follows.

The lattice crack deviation parameter is, like its lattice trapping counterpart, also an energy barrier, as well as a manifestation of the discreteness of the lattice itself. It also is influenced by the direction in which the crack front bonds are broken. In what follows, the critical stress, σ^{+}_{sc}, responsible for shear kinking of bonds which follow zigzag paths, can be obtained by taking a simple micro-mechanics approach. The approach adopted here is analogous to microbuckling, kink band formation and

propagation instability in a unidirectional fiber reinforced composite specimen, such as carbon fiber reinforced epoxy, with initial fiber waviness or misalignment [56–58]. The primary difference is, however, that here although the applied loading is tensile (and not compressive), the bond will initially be compressed and shear-kinked because of the snapping effect. The dominant effect of the shear deformation would cause the onset of a critical state in the parallel atomic bonds, responsible for a collective phenomenon (domino effect) of kinked bond–band formation and propagation, leading to crack turning from a more difficult cleavage system to an easier one. The details of the mathematical derivation are presented in Appendix 5. An atomic bond level analysis yields the stress intensity factor (or fracture toughness) for loading as follows:

$$K_c^+ = C\sigma_c^+ = C\left[\frac{\varepsilon_{bd}\cos(\phi_0 - \gamma_{bd})}{s_{11}} + \frac{\gamma_{bd}}{s_{66}(\phi_0 - \gamma_{bd})}\right]; \quad \phi_0 > \gamma_{bd} \geq 0, \tag{73}$$

where σ_c^+ is the critical stress (loading or bond breaking), C is a constant (function of crack length, specimen geometry, etc.), and K is the mode I stress intensity factor. The superscript "+" denotes the loading case. The extensional strain, ε_{bd}, is computed from the corresponding shear strain, γ_{bd}, using Mohr's circle [56]. The corresponding stress intensity factor for unloading is given by

$$K_c^- = C\sigma_c^- = C\left[\frac{\varepsilon_{bd}\cos(\phi_0 - \gamma_{bd})}{s_{11}} + \frac{\gamma_{bd}}{s_{66}\phi_0}\right], \tag{74}$$

in which the superscript "–" denotes the unloading (i.e. bond healing) case. The LCD regime, where a crack of given length remains stable at one particular position in the lattice (lattice trapped) and/or propagate in a "difficult" manner, before turning from a more "difficult" cleavage system to an easier one, is given by $\Delta K^* = K_c^+/K_c^- - 1$.

9. Crack deflection (deviation) analysis

Atomic bonding in rock salt crystals and alkali (bcc) metals along three important principal directions, [100], [110] and [111], has been illustrated by Newnham (see Figure 75 of [59]). In rock salt single crystals, such as LiF, NaCl and KCl, the bonds form uninterrupted chains along the edges of the cubic cell. In contrast, in bcc metals, such as Li, Na and K, the bonds to nearest neighbor atoms are directed along the [111] body diagonals; consequently, these bonds form uninterrupted chains in these directions [59].

In single crystals of alkali halides (rock salt structure), when subjected to tensile stress, σ^+, applied along, e.g. [010] direction, bonds will ultimately fail in tension, and no rotation or shear deformation effect is expected to influence bond failure. No crack deviation is expected in such cases. In contrast, when single crystals of bcc metals are subjected to tensile stress, σ^+, applied along, e.g. [010] direction, bonds, which follow zigzag paths, will rotate as well as elongate. In such cases, the bond failure will primarily be governed by shear deformation, and will lead to crack deflection. A review of the literature reveals an absence of this type of analysis.

The present analysis is based on elastic plane inextensional deformation of the bond. Figure 3a depicts the schematic of a pair of misaligned bonds under tension,

whereas the shear kinking of a bond and associated rotational/shear instability is illustrated in Figure 3b. The concept is analogous to micro-kinks in carbon fibers discussed by Chaudhuri [60]. The initial bond misalignment is defined as follows [56]:

$$u_0(x, y) = \frac{u_0}{L}[yH(y) - (y - L)H(y - L)], \tag{75}$$

where L is the length of a chemical bond, u_0 is the "initial displacement" in the x-direction, as shown in Figure 3a, and $H(y)$ is the Heaviside function. The governing partial differential equation can be written as follows [56]:

$$(1 + s_{66}\sigma_c^+)u_{,yy} + \frac{s_{66}}{s_{11}}u_{,xx} = s_{66}\sigma_c^+ u_{0,yy}, \tag{76}$$

where $u(x, y)$ is the displacement component in the x-direction, whereas $s_{ij}, i, j = 1, \ldots, 6$, represent the elastic compliances of a crystal. Utilizing the fact that

$$y\delta(y) = (y - L)\delta(y - L) = 0, \tag{77}$$

and substitution of Equation (75) into Equation (76) leads to

$$(1 + s_{66}\sigma_{sc}^+)u_{,yy} + \frac{s_{66}}{s_{11}}u_{,xx} = \frac{s_{66}\sigma_{sc}^+ u_0}{L}[y\delta(y) - (y - L)\delta(y - L)]. \tag{78}$$

The detailed mathematical derivation of the solution is provided in Appendix 6. Finally, substitution of Equation (130) into Equation (141) leads to the following:

$$|\tan(\beta)| = \left[\frac{s_{11}}{s_{66}}\left(\frac{\phi_0}{\phi_0 - \gamma_{bd}}\right)\right]^{1/2}; \quad \phi_0 > \gamma_{bd} \geq 0. \tag{79}$$

This is illustrated in Figure 4.

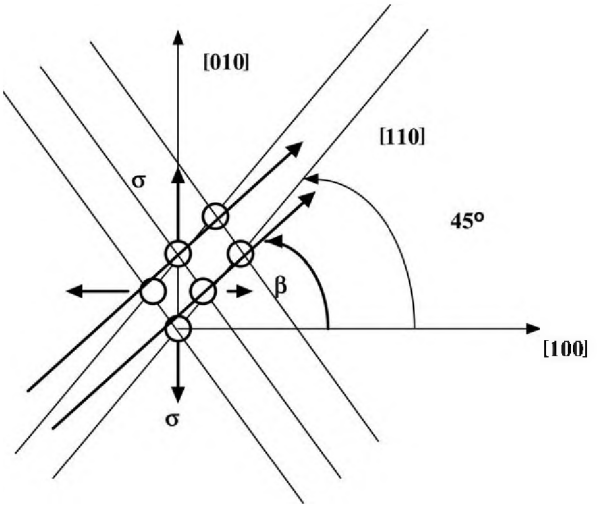

Figure 4. Schematic of lattice crack deviation in a cubic crystal.

10. Structure–fracture property relationships for certain cubic crystals

The present investigation considers three through-crack systems ((crack plane)[crack front] × [propagation direction]), (010)[001] × [100], $(\bar{1}10)[001] \times [110]$ and $(1\bar{1}0)[110] \times [001]$, weakening cubic crystals, and their relatively easy cleavage planes/directions for propagation. The term relatively easy cleavage plane is used here, since the cubic crystals are known to have other cleavage planes, such as {111}, {112}, and other directions of propagation, which are not investigated here. For example, Ebrahimi and Kalwani [21] have listed 15 cleavage planes and their surface energies in silicon single crystals. It can easily been seen from this analysis that the choice for an easy cleavage plane depends on the normalized elastic parameter, χ, χ' or χ'', which, in turn, depends on the respective anisotropic ratio, $\bar{\lambda} = 1/\lambda$, $1/\lambda'$ or $1/\lambda''$. $\bar{\lambda} = 1/\lambda$ is a function of the elastic stiffness coefficients computed with respect to the cube edges.

Elastic stiffness constants, c_{11}, c_{12} and c_{66}, are listed in Table 1 for various cubic single crystal systems, which are taken from standard references, e.g. [59,61]. The anisotropic ratio, $\bar{\lambda} = \lambda'$, its inverse, λ, and the normalized elastic parameter, χ, for the (010)[001] cleavage system are listed in Table 2. Table 2 also lists inverse anisotropic ratios, λ', λ'' as well as normalized elastic parameters, χ', χ'', for the $(\bar{1}10)[001]$ and $(1\bar{1}0)[110]$ cleavage systems.

Table 3 lists the nature of the roots (i.e. complex or imaginary) and the (relatively) easy cleavage system(s) for crack propagation among the three cleavage systems investigated here. The elastic properties are controlled by various aspects of the underlying structural chemistry of these cubic crystals, such as the Bravais lattice type, bonding (covalent, ionic and metallic), bonding (including hybridized) orbitals, electro-negativity of constituent atoms in a compound, polarity, etc. The details of these characteristics pertaining to structural chemistry of the crystals considered here are available in the published literature (see, for example, [59,62,63]).

It may be noted from Table 2 that the alkali metals, Li, Na, and K, have the highest $\bar{\lambda}$ values, whereas RbI and other ionic crystals with the rock salt structure have the lowest. Atomic bonding along several principal directions in these cubic crystals are illustrated and discussed in Newnham [59].

In bcc alkali metal crystals, such as Li, Na, and K, the bonds to nearest-neighbor atoms are directed along the ⟨111⟩ body diagonals [59]. Consequently, the bonds form uninterrupted chains in these directions. It can easily be seen that when these crystals are stretched along any of the ⟨111⟩ directions, the bonds parallel to that direction are elongated in the absence of any bending. Thus, the elastic stiffness for any of the ⟨111⟩ directions is expected to be relatively large, since only stretching and no shear is involved. In contrast, when tensile stresses are applied along any of the ⟨100⟩ directions, the near-neighbor bonds in bcc metals follow a zigzag path in this direction [59]. This is because when stretched along a cube edge, the bonds will rotate as well as elongate. This results in a smaller elastic stiffness coefficient in ⟨100⟩ than its ⟨111⟩ counterpart, since force constants for bending are generally smaller than for stretching [59]. This explains the large anisotropic ratios, $\bar{\lambda} = \lambda'$, for the alkali metals listed in Table 2. As a result, λ and χ are less than unity and 0, respectively ($\chi < 0$, $\chi' > 1$) for these crystals, giving rise to complex roots for the (010)[001] through-crack and imaginary roots for the $(\bar{1}10)[001]$ through-crack. In the same vein, λ'' and χ'' are

Table 1. Structures and elastic properties of various cubic single crystals [59,61].

Crystal (Temp. K)	Structure	Bravais lattice	c_{11} (GPa)	c_{12} (GPa)	c_{66} (GPa)
Li (298)	bcc	bcc	13.50	11.44	8.78
Na (299)	bcc	bcc	7.39	6.22	4.19
K (299)	bcc	bcc	3.70	3.14	1.88
α-Fe (room)	bcc	bcc	236.88	140.63	116.01
Ta (300)	bcc	bcc	260.91	157.43	81.82
W (300)	bcc	bcc	523.27	204.53	160.72
Mo (300)	bcc	bcc	440.77	172.43	121.65
V (300)	bcc	bcc	227.95	118.70	42.55
Nb (300)	bcc	bcc	246.50	134.50	28.73
Au (room)	fcc	fcc	192.90	163.80	41.50
Th (300)	fcc	fcc	75.30	48.90	47.80
Cu (room)	fcc	fcc	168.40	121.40	75.40
Ag (room)	fcc	fcc	124.00	93.40	46.10
Pd (300)	fcc	fcc	227.10	176.04	71.73
Ni (room)	fcc	fcc	246.50	147.30	124.70
Pt (300)	fcc	fcc	346.70	250.70	76.50
Al (room)	fcc	fcc	107.30	60.90	28.30
Ge (room)	Dia. cubic	fcc	129.20	47.90	67.00
Si (298)	Dia. cubic	fcc	165.78	63.94	79.62
C (dia.) (300)	Dia. cubic	fcc	1076.00	125.00	575.80
AlSb (300)	Zinc blende	fcc	89.39	44.27	41.55
GaSb (298)	Zinc blende	fcc	88.50	40.40	43.30
GaAs (room)	Zinc blende	fcc	119.04	53.84	59.52
GaP (300)	Zinc blende	fcc	141.20	62.53	70.47
InAs (room)	Zinc blende	fcc	83.29	45.26	39.59
InP (room)	Zinc blende	fcc	102.20	57.60	46.00
InSb (room)	Zinc blende	fcc	67.00	36.49	30.19
ZnS (room)	Zinc blende	fcc	100.00	65.00	34.00
ZnSe (298)	Zinc blende	fcc	80.96	48.81	44.05
ZnTe (298)	Zinc blende	fcc	71.34	40.78	31.15
CdTe (298)	Zinc blende	fcc	53.51	36.81	19.94
HgTe	Zinc blende	fcc	54.80	38.10	20.40
LiF (room)	Rock salt	fcc	111.20	42.00	62.80
LiCl (room)	Rock salt	fcc	49.40	22.60	24.90
LiBr (room)	Rock salt	fcc	39.40	18.80	19.10
MgO (300)	Rock salt	fcc	289.30	87.70	154.77
NaF (room)	Rock salt	fcc	97.10	24.30	28.00
NaCl (room)	Rock salt	fcc	49.70	12.70	12.70
NaBr (300)	Rock salt	fcc	39.70	10.01	9.98
KF (room)	Rock salt	fcc	65.80	14.90	12.80
KCl (295)	Rock salt	fcc	40.50	6.98	6.30
KBr (room)	Rock salt	fcc	34.60	5.80	5.05
RbF (room)	Rock salt	fcc	57.00	12.50	9.10
RbCl (room)	Rock salt	fcc	36.45	6.10	4.75
RbBr (300)	Rock salt	fcc	31.55	4.93	3.80
TiC (room)	Rock salt	fcc	500.00	113.00	175.00
PbS	Rock salt	fcc	127.00	29.80	24.80
PbSe	Rock salt	fcc	107.00	7.70	13.00
PbF_2 (300)	Fluorite	fcc	88.80	47.20	24.54
BaF_2 (room)	Fluorite	fcc	90.10	40.30	24.90

(*continued*)

Table 1. Continued.

Crystal (Temp. K)	Structure	Bravais lattice	c_{11} (GPa)	c_{12} (GPa)	c_{66} (GPa)
SrF_2 (300)	Fluorite	fcc	123.50	43.05	31.28
ThO_2 (298)	Fluorite	fcc	367.00	106.00	79.70
CaF_2 (room)	Fluorite	fcc	164.00	45.00	33.80
UO_2 (298)	Fluorite	fcc	396.00	121.00	64.10
$MgAl_2O_4$ (room)	Spinel	fcc	279.00	153.00	153.00
$BaTiO_3$ (423)	Perovskite	Simple cubic	172.78	81.96	108.23
$SrTiO_3$ (room)	Perovskite	Simple cubic	348.17	100.64	454.55

Table 2. Inverse anisotropic ratios and normalized elastic parameters of various cubic single crystals.

Crystal	$\bar{\lambda} = \lambda' = 1/\lambda$	λ	χ	λ''	χ''
Li	8.5243	0.1173	−0.6176	0.3131	0.1203
Na	7.1624	0.1396	−0.5846	0.3334	0.1038
K	6.7143	0.1489	−0.5734	0.3426	0.1032
α-Fe	2.4106	0.4148	0.0674	0.5519	0.2798
Ta	1.5814	0.6324	0.4106	0.7218	0.5329
W	1.0085	~1.0	~1.0	~1.0	~1.0
Mo	0.9067	1.1029	1.1432	1.0770	1.1236
V	0.7790	1.2838	1.4316	1.2119	1.3618
Nb	0.5130	1.9492	2.4671	1.7049	2.2404
Au	2.8522	0.3506	−0.2008	0.5077	0.0435
Th	3.6212	0.2762	−0.1938	0.4401	0.1151
Cu	3.2085	0.3117	−0.1845	0.4722	0.1220
Ag	3.0131	0.3319	−0.1713	0.4897	0.1303
Pd	2.8129	0.3555	−0.1441	0.5383	0.2598
Ni	2.5141	0.3978	0.0380	0.5383	0.2598
Pt	1.5938	0.6275	0.3581	0.7188	0.5030
Al	1.2198	0.8198	0.7175	0.8643	0.7710
Ge	1.6482	0.6067	0.4609	0.7005	0.8166
Si	1.5636	0.6395	0.5005	0.7261	0.5803
C (diamond)	1.2109	0.8258	0.8056	0.8684	0.8166
AlSb	1.8418	0.5429	0.3165	0.6517	0.4496
GaSb	1.8004	0.5554	0.3524	0.6611	0.4645
GaAs	1.8258	0.5477	0.3431	0.6550	0.4643
GaP	1.7915	0.5582	0.3626	0.6632	0.4211
InAs	2.0820	0.4803	0.1979	0.6709	0.4023
InP	2.0628	0.4848	0.1944	0.6069	0.3669
InSb	1.9790	0.5053	0.2359	0.6228	0.3952
ZnS	1.9429	0.5147	0.1993	0.6314	0.7208
ZnSe	2.7403	0.3649	−0.0180	0.5120	0.2227
ZnTe	2.0388	0.4905	0.1993	0.6115	0.3714
CdTe	2.3880	0.4188	0.0190	0.5570	0.2544
HgTe	2.4431	0.4093	−0.0014	0.5497	0.2410
LiF	1.8150	0.5510	0.3814	0.6569	0.4833
LiCl	1.8582	0.5382	0.3269	0.6487	0.4780
LiBr	1.8544	0.5393	0.3195	0.6487	0.4780
MgO	1.5364	0.6513	0.5456	0.7347	0.6067

(*continued*)

Table 2. Continued.

Crystal	$\bar{\lambda} = \lambda' = 1/\lambda$	λ	χ	λ''	χ''
NaF	0.7692	1.3000	1.3751	1.2233	1.3411
NaCl	0.6865	1.4567	1.5734	1.3390	1.5228
NaBr	0.6723	1.4875	1.6104	1.3618	1.5576
KF	0.5030	1.9883	2.2121	1.7280	2.1268
KCl	0.3759	2.6603	2.9465	2.2143	2.8532
KBr	0.3507	2.8515	3.1619	2.3522	3.0641
RbF	0.4090	2.4451	2.7620	2.0601	2.6510
RbCl	0.3130	3.1947	3.5620	2.6003	3.4520
RbBr	0.2855	3.5026	3.8937	2.8210	3.7825
TiC	0.9044	1.1057	1.1296	1.0790	1.1181
PbS	0.5103	1.9597	2.1849	1.7073	2.0982
PbSe	0.2618	3.8192	4.0220	3.0408	3.9735
PbF_2	1.1798	0.8476	0.7666	0.8853	0.8087
BaF_2	~1.0	~1.0	~1.0	~1.0	~1.0
SrF_2	0.7776	1.2860	1.3857	1.2060	1.3296
ThO_2	0.6107	1.6374	1.8215	1.4721	1.7442
CaF_2	0.5681	1.7604	1.9691	1.5622	1.8841
UO_2	0.4662	2.1451	2.495	1.8470	2.3641
$MgAl_2O_4$	2.4386	0.4118	0.0892	0.5486	0.2899
$BaTiO_3$	2.3834	0.4196	0.1443	0.5535	0.3186
$SrTiO_3$	3.67	0.2720	0.0616	0.4241	0.2184

Table 3. Nature of roots for three cleavage systems and relatively easy cleavage system(s).

Crystal	Roots $\{010\}\langle001\rangle$	Roots $\{\bar{1}10\}\langle001\rangle$	Roots $\{1\bar{1}0\}\langle110\rangle$	Relatively easy cleavage system(s)	
Li	Complex	Imaginary	Complex	$\{\bar{1}10\}\langle001\rangle$	
Na	Complex	Imaginary	Complex	$\{\bar{1}10\}\langle001\rangle$	
K	Complex	Imaginary	Complex	$\{\bar{1}10\}\langle001\rangle$	
α-Fe	Complex	Imaginary	Complex	$\{\bar{1}10\}\langle001\rangle$	
Ta	Complex	Imaginary	Complex	$\{\bar{1}10\}\langle001\rangle$	
W	Degenerate	Degenerate	Degenerate	$\{010\}\langle001\rangle$	$\{1\bar{1}0\}\langle110\rangle$
Mo	Imaginary	Complex	Imaginary	$\{010\}\langle001\rangle$	$\{1\bar{1}0\}\langle110\rangle$
V	Imaginary	Complex	Imaginary	$\{010\}\langle001\rangle$	$\{1\bar{1}0\}\langle110\rangle$
Nb	Imaginary	Complex	Imaginary	$\{010\}\langle001\rangle$	$\{1\bar{1}0\}\langle110\rangle$
Au	Complex	Imaginary	Complex	$\{\bar{1}10\}\langle001\rangle$	
Th	Complex	Imaginary	Complex	$\{\bar{1}10\}\langle001\rangle$	
Cu	Complex	Imaginary	Complex	$\{\bar{1}10\}\langle001\rangle$	
Ag	Complex	Imaginary	Complex	$\{\bar{1}10\}\langle001\rangle$	
Pd	Complex	Imaginary	Complex	$\{\bar{1}10\}\langle001\rangle$	
Ni	Complex	Imaginary	Complex	$\{\bar{1}10\}\langle001\rangle$	
Pt	Complex	Imaginary	Complex	$\{\bar{1}10\}\langle001\rangle$	
Al	Complex	Imaginary	Complex	$\{\bar{1}10\}\langle001\rangle$	
Ge	Complex	Imaginary	Complex	$\{\bar{1}10\}\langle001\rangle$	
Si	Complex	Imaginary	Complex	$\{\bar{1}10\}\langle001\rangle$	
C (diamond)	Complex	Imaginary	Complex	$\{\bar{1}10\}\langle001\rangle$	
AlSb	Complex	Imaginary	Complex	$\{\bar{1}10\}\langle001\rangle$	

(*continued*)

Table 3. Continued.

Crystal	Roots $\{010\}\langle 001\rangle$	Roots $\{\bar{1}10\}\langle 001\rangle$	Roots $\{1\bar{1}0\}\langle 110\rangle$	Relatively easy cleavage system(s)	
GaSb	Complex	Imaginary	Complex	$\{\bar{1}10\}\langle 001\rangle$	
GaAs	Complex	Imaginary	Complex	$\{\bar{1}10\}\langle 001\rangle$	
GaP	Complex	Imaginary	Complex	$\{\bar{1}10\}\langle 001\rangle$	
InAs	Complex	Imaginary	Complex	$\{\bar{1}10\}\langle 001\rangle$	
InP	Complex	Imaginary	Complex	$\{\bar{1}10\}\langle 001\rangle$	
InSb	Complex	Imaginary	Complex	$\{\bar{1}10\}\langle 001\rangle$	
ZnS	Complex	Imaginary	Complex	$\{\bar{1}10\}\langle 001\rangle$	
ZnSe	Complex	Imaginary	Complex	$\{\bar{1}10\}\langle 001\rangle$	
ZnTe	Complex	Imaginary	Complex	$\{\bar{1}10\}\langle 001\rangle$	
CdTe	Complex	Imaginary	Complex	$\{\bar{1}10\}\langle 001\rangle$	
HgTe	Complex	Imaginary	Complex	$\{\bar{1}10\}\langle 001\rangle$	
LiF	Complex	Imaginary	Complex	$\{\bar{1}10\}\langle 001\rangle$	
LiCl	Complex	Imaginary	Complex	$\{\bar{1}10\}\langle 001\rangle$	
LiBr	Complex	Imaginary	Complex	$\{\bar{1}10\}\langle 001\rangle$	
MgO	Complex	Imaginary	Complex	$\{\bar{1}10\}\langle 001\rangle$	
NaF	Imaginary	Complex	Imaginary	$\{010\}\langle 001\rangle$	$\{1\bar{1}0\}\langle 110\rangle$
NaCl	Imaginary	Complex	Imaginary	$\{010\}\langle 001\rangle$	$\{1\bar{1}0\}\langle 110\rangle$
NaBr	Imaginary	Complex	Imaginary	$\{010\}\langle 001\rangle$	$\{1\bar{1}0\}\langle 110\rangle$
KF	Imaginary	Complex	Imaginary	$\{010\}\langle 001\rangle$	$\{1\bar{1}0\}\langle 110\rangle$
KCl	Imaginary	Complex	Imaginary	$\{010\}\langle 001\rangle$	$\{1\bar{1}0\}\langle 110\rangle$
KBr	Imaginary	Complex	Imaginary	$\{010\}\langle 001\rangle$	$\{1\bar{1}0\}\langle 110\rangle$
RbF	Imaginary	Complex	Imaginary	$\{010\}\langle 001\rangle$	$\{1\bar{1}0\}\langle 110\rangle$
RbCl	Imaginary	Complex	Imaginary	$\{010\}\langle 001\rangle$	$\{1\bar{1}0\}\langle 110\rangle$
RbBr	Imaginary	Complex	Imaginary	$\{010\}\langle 001\rangle$	$\{1\bar{1}0\}\langle 110\rangle$
TiC	Imaginary	Complex	Imaginary	$\{010\}\langle 001\rangle$	$\{1\bar{1}0\}\langle 110\rangle$
PbS	Imaginary	Complex	Imaginary	$\{010\}\langle 001\rangle$	$\{1\bar{1}0\}\langle 110\rangle$
PbSe	Imaginary	Complex	Imaginary	$\{010\}\langle 001\rangle$	$\{1\bar{1}0\}\langle 110\rangle$
PbF_2	Complex	Imaginary	Complex	$\{\bar{1}10\}\langle 001\rangle$	
BaF_2	Degenerate	Degenerate	Degenerate	TBD*	
SrF_2	Imaginary	Complex	Imaginary	$\{010\}\langle 001\rangle$	$\{1\bar{1}0\}\langle 110\rangle$
ThO_2	Imaginary	Complex	Imaginary	$\{010\}\langle 001\rangle$	$\{1\bar{1}0\}\langle 110\rangle$
CaF_2	Imaginary	Complex	Imaginary	$\{010\}\langle 001\rangle$	$\{1\bar{1}0\}\langle 110\rangle$
UO_2	Imaginary	Complex	Imaginary	$\{010\}\langle 001\rangle$	$\{1\bar{1}0\}\langle 110\rangle$
$MgAl_2O_4$	Complex	Imaginary	Complex	$\{\bar{1}10\}\langle 001\rangle$	
$BaTiO_3$	Complex	Imaginary	Complex	$\{\bar{1}10\}\langle 001\rangle$	
$SrTiO_3$	Complex	Imaginary	Complex	$\{\bar{1}10\}\langle 001\rangle$	

Note: *TBD: to be determined

less than unity and $\sqrt{c_{11}/c'_{11}}$, respectively, also giving rise to complex roots for the $(1\bar{1}0)[110]$ through crack. It can then be inferred that $\{\bar{1}10\}\langle 001\rangle$ would constitute a relatively easy cleavage system, while both $\{010\}\langle 001\rangle$ and $\{1\bar{1}0\}\langle 110\rangle$ would be deemed difficult. This behavior somewhat carries over to transition metals with bcc structures, such as α-Fe and Ta, listed in Tables 1–3, the only difference is that $\chi > 0$. It may be noted here that α-Fe and Ta as well as W, Mo, V and Nb, all transition metals with bcc structure, belong to the *d*-block with partially filled *d*-shells [63].

The latter transition metals with bcc structure, such as W, Mo, V and Nb listed in Tables 1 and 2 are, however, exceptions to the above behavior attributable to the bcc structure. The anisotropic ratios, $\bar{\lambda} = \lambda'$, for these transition metals, as listed in Table 2, are less than unity with the exception of W, which is macroscopically isotropic. As a result, λ (or λ'') and χ are both greater than unity ($\chi > 1$, $\chi' < 1$, $\chi'' > \sqrt{c_{11}/c'_{11}}$) for Mo, V and Nb crystals, giving rise to imaginary roots for the (010)[001] and (1$\bar{1}$0)[110] through-cracks, and complex roots for the ($\bar{1}$10)[001] through-crack. It can then be inferred that both {010}⟨001⟩ and {1$\bar{1}$0}⟨110⟩ would constitute easy cleavage systems, while {$\bar{1}$10}⟨001⟩ would be deemed difficult. The reason for this exceptional behavior for these transition metals is the occurrence of mixed metallic–covalent bonding known as hybridization [63], involving various types of "dsp" bonding orbitals, which more than compensates the behavior attributed to the bcc structure. Six octahedral d^2sp^3 hybrids are formed when the $d_{x^2-y^2}$, d_{z^2}, an s, and the three p orbitals are mixed (according to crystal field theory) [64]. These bonds lie along the x, y and z axes in plus and minus directions, and can be used in construction of six "σ" bonds [64]. Covalent bond is, unlike its metallic counterpart, known to be highly directional. It appears that for α-Fe and Ta, this effect of mixed metallic-covalent bonding involving various types of "*dsp*" bonding orbitals is not large enough to alter the behavior due to the bcc structure, while in W, the two effects seem to balance each other.

In monocrystalline fcc metals, the bonds are oriented along the face diagonals, ⟨110⟩. The fcc metals Au, Cu, Ag, Pd, Ni, Pt and Al, listed in Tables 1–3, all belong to the *d*-block with partially filled *d*-shells [63]. Th, which belongs to the actinide series, belongs to the same category. The fcc metals contain linear chains of near-neighbor bonds in these directions, resulting in higher elastic stiffness coefficients along them. Since the ⟨110⟩ directions are generally closer to the corresponding ⟨111⟩ compared to their ⟨100⟩ counterparts, $\bar{\lambda} = \lambda'$ is generally larger than unity. λ (or λ'') and χ are both less than unity ($\chi < 1$, $\chi' > 1$, $\chi'' < \sqrt{c_{11}/c'_{11}}$) for these crystals, giving rise to complex roots for both the (010)[001] and (1$\bar{1}$0)[110] through-cracks, and imaginary roots for the ($\bar{1}$10)[001] through-crack. It can then be inferred that {$\bar{1}$10}⟨001⟩ would constitute an easy cleavage system, while both {010}⟨001⟩ and {1$\bar{1}$0}⟨110⟩ would be deemed difficult.

The last class of elemental cubic single crystals considered here belong to group IVA of the periodic table. The group IVA elements C, Si and Ge vary in metallicity from C to Ge. While C (diamond) is strictly nonmetallic, characterized by covalent bonding, there is some metallic character in Si and Ge, the last one being termed metalloid [63]. As reported by Hoshi and Fujiwara [65], the electronic structures of the diamond cubic structure solids can be scaled with the metallicity parameter, α_m, defined using the quantum mechanical concept of hopping within an atom, wherein the nearest neighbor tight binding (TB) Hamiltonians can be constructed within the sp^3-hybridized orbitals. Detailed discussions on this topic are available in standard treatises, e.g., Harrison [66]. A system would be termed metallic, when $\alpha_m \to 1$. Computed α_m values for C, Si and Ge are reported to be 0.44, 0.75 and 0.77, respectively [65]. Si and Ge are also semiconductors unlike carbon. The covalent bond being strongly directional in nature gives diamond its high stiffness, as noted in Table 1. The diamond cubic structure displayed by these crystals can be seen from two points of view, as illustrated by Cotton and Wilkinson [63]: (i) the conventional

cubic unit cell and (ii) stacked layers, with layers running perpendicular to the body diagonals of the cubic.

It may be noted that the above bonds, unlike in the bcc and fcc metals, are not arranged in linear chains in crystals with diamond cubic structure listed in Tables 1–3. Here although the bonds are oriented along ⟨111⟩ directions, they are not continuously connected [59]. Tensile strain along any of the ⟨111⟩ directions will, therefore, involve some bending as well as stretching. It is therefore reasonable to expect that the anisotropic ratios ($\bar{\lambda} = \lambda' = 1/\lambda$) for these classes of crystals are generally not much larger than unity (Table 2). Additionally, because of such layering, the easy cleavage plane for these cubic crystals belongs to the {111}, while {110} cleavage planes are also possible. The fracture in different propagation directions on the {111} cleavage planes is currently under investigation, and will be reported in a follow-up paper. As shown in Tables 2 and 3, λ (or λ'') and χ are both less than unity ($\chi < 1, \chi' > 1, \chi'' < \sqrt{c_{11}/c'_{11}}$) for these crystals, giving rise to complex roots for both the (010) [001] and ($1\bar{1}0$)[110] through-cracks, and imaginary roots for the ($\bar{1}10$)[001] through-crack. It can then be inferred that {$\bar{1}10$}⟨001⟩ would constitute a relatively easy cleavage system, while both {010}⟨001⟩ and {$1\bar{1}0$}⟨110⟩ would be deemed difficult. This is in agreement with experimental and computer simulation results for Si [17,28]. This also explains the anisotropy of crack propagation on the {110} in Si, both experimentally observed [17,28] as well as supported by computer simulations [28].

The next classes of cubic single crystals studied here belong to compounds, such as those with rock salt (NaCl), zinc blende (ZnS) and fluorite (CaF_2) cubic structures. As Cotton and Wilkinson [63] have stated, that "as soon as one changes from elements, where adjacent atoms are identical and the bonds are necessarily non-polar, to compounds, there enters the vexatious question of when to describe a substance ionic and when to describe it as covalent". Table 4 lists % of ionic character of compound cubic crystals with rock salt, zinc blende and fluorite structures, based on Pauling's [62] approximate formula given below:

$$\% \text{ of ionic character in a single bond} = \left[1 - \exp\left\{-\frac{(X_A - X_B)^2}{4}\right\}\right]100, \qquad (80)$$

in which X_A and X_B are electronegativity coefficients for elements A and B, respectively, forming the single bond. For example, Cotton and Wilkinson [63] have further added, "bonds between unlike atoms all have some degree of polarity and when the polarity is relatively small it is practical to describe the bonds as polar covalent and when the polarity is very high it makes more sense to consider that the substance consists of an array of ions".

In rock salt structure, the bonds form uninterrupted chains along the ⟨100⟩ cube edges. As shown in Table 2, the anisotropic ratios ($\bar{\lambda} = \lambda' = 1/\lambda$) are generally smaller than unity for alkali halides (with the rock salt structure), which implies that the crystal is the stiffest along the cube edges, ⟨100⟩, which are also directions for nearest-neighbor bonds. Under applied tensile stress parallel to any of the ⟨100⟩ directions, the bonds elongate without any rotation. In contrast, tensile stresses applied parallel to ⟨110⟩, ⟨111⟩ and other directions result in bending motion in addition to stretching [59]. Since bending is generally easier than stretching, alkali

Table 4. Percentage of ionic bonding in compound crystals, based on Pauling's [62] equation.

Crystal	Structure	X_M	X_N	% Ionic bond
AlSb	Zinc blende	1.5	1.8	2.23
GaSb	Zinc blende	1.8	1.8	0
GaAs	Zinc blende	1.8	2.2	3.92
GaP	Zinc blende	1.8	2.1	2.23
InAs	Zinc blende	1.5	2.2	11.53
InP	Zinc blende	1.5	2.1	8.61
InSb	Zinc blende	1.5	1.8	2.23
ZnS	Zinc blende	1.7	2.4	11.53
ZnSe	Zinc blende	1.7	2.5	14.79
ZnTe	Zinc blende	1.7	2.0	2.23
CdTe	Zinc blende	1.5	2.0	6.06
HgTe	Zinc blende	1.5	2.0	6.06
LiF	Rock salt	1.0	4.1	90.95
LiCl	Rock salt	1.0	2.9	59.45
LiBr	Rock salt	1.0	2.8	55.50
MgO	Rock salt	1.3	3.5	70.18
NaF	Rock salt	1.0	4.1	90.95
NaCl	Rock salt	1.0	2.9	59.45
NaBr	Rock salt	1.0	2.8	55.50
KF	Rock salt	0.9	4.1	92.27
KCl	Rock salt	0.9	2.9	63.21
KBr	Rock salt	0.9	2.8	59.45
RbF	Rock salt	0.9	4.1	92.27
RbCl	Rock salt	0.9	2.9	63.21
RbBr	Rock salt	0.9	2.8	59.45
TiC	Rock salt	1.3	2.5	30.23
PbS	Rock salt	1.6	2.4	14.79
PbSe	Rock salt	1.6	2.5	18.33
PbF_2	Fluorite	1.6	4.1	79.04
BaF_2	Fluorite	0.9	4.1	92.27
SrF_2	Fluorite	1.0	4.1	90.95
ThO_2	Fluorite	1.0	3.5	92.27
CaF_2	Fluorite	1.1	4.1	79.04
UO_2	Fluorite	1.0	3.5	79.04

halides are stiffest along the ⟨100⟩ directions. As a result, λ (or λ'') and χ are both greater than unity ($\chi > 1, \chi' < 1, \chi'' > \sqrt{c_{11}/c'_{11}}$) for these alkali halide crystals, giving rise to imaginary roots for the (010)[001] and $(1\bar{1}0)$[100] through-cracks, and complex roots for the $(\bar{1}10)$[001] through-crack. It can then be inferred that both $\{010\}\langle 001\rangle$ and $\{1\bar{1}0\}\langle 110\rangle$ would constitute easy cleavage systems, whereas $\{\bar{1}10\}\langle 001\rangle$ would be deemed difficult.

MgO (an alkaline earth metal oxide) and lithium salts are, however, exceptions to the above-mentioned general rule for ionic crystals with the rock salt structure, for which $\bar{\lambda} = \lambda' > 1$. The reason is explained by Newnham [59]. For rock salt structures with small cations, such as Li^+ and Mg^{2+}, the anions are in contact with one another. Bending actions are restricted when the anions are in contact. Consequently, elastic stiffness coefficients in the ⟨110⟩ and ⟨111⟩ directions become larger than their ⟨100⟩

counterparts, resulting in larger than unity $\bar{\lambda} = \lambda'$. This is in contrast to the alkali halides, such as NaCl and KCl, where Cl^- anions are not in contact. The importance of anion-anion forces were pointed out by Weidner and Simmons [67], who have found, in connection with the computation of elastic properties of several alkali halides from a two-body central force model, the necessity to include anion-anion interactions in addition to cation-anion forces. As shown in Tables 2 and 3, λ (or λ'') and χ are both less than unity ($\chi < 1, \chi' > 1, \chi'' < \sqrt{c_{11}/c'_{11}}$) for these crystals, giving rise to complex roots for both the (010) [001] and $(1\bar{1}0)[110]$ through-cracks, and imaginary roots for the $(\bar{1}10)[001]$ through-crack. It can then be inferred that $\{\bar{1}10\}\langle 001\rangle$ would constitute an easy cleavage system, whereas both $\{010\}\langle 001\rangle$ and $\{1\bar{1}0\}\langle 110\rangle$ would be deemed difficult.

TiC, PbS and PbSe with rock salt structures are more covalent than ionic, as compared to NaCl. However, TiC, PbS and PbSe although covalent like zinc blende compounds behave like other crystals with rock salt structures (NaCl). It may be noted that TiC is an interstitial-type carbide in which the carbon atom occupies the octahedral hole in a closed packed array of metal (Ti) atoms [59]. Since the anisotropic ratios, $\bar{\lambda} = \lambda'$, for these crystals, as listed in Table 2, are less than unity, λ (or λ'') and χ are both greater than unity ($\chi > 1, \chi' < 1, \chi'' > \sqrt{c_{11}/c'_{11}}$), giving rise to imaginary roots for both the (010)[001] and $(1\bar{1}0)[110]$ through-cracks, and complex roots for the $(\bar{1}10)[001]$ through-crack. It can then be inferred that both $\{010\}\langle 001\rangle$ and $\{1\bar{1}0\}\langle 110\rangle$ would constitute easy cleavage systems, while $\{\bar{1}10\}\langle 001\rangle$ would be deemed difficult.

Since the bonds are not arranged in linear chains, the situation becomes more complicated in other compound cubic crystal structures listed in Tables 1–3. In the zinc blende (sphalerite) and fluorite structures, the bonds are oriented along $\langle 111\rangle$ directions, but they are not continuously connected [59]. Tensile strain along any of the $\langle 111\rangle$ directions will, therefore, involve some bending as well as stretching [59]. It is therefore reasonable to expect that the anisotropic ratios ($\bar{\lambda} = \lambda' = 1/\lambda$) for these classes of crystals are generally not much larger than unity (Table 2).

The III–V compound semiconductors, AlSb, GaSb, GaAs, GaP, InAs, InP and InSb listed in Tables 1–3 have zinc blende (ZnS) or sphalerite (essentially diamond cubic) structures. The same is true II–VI compound semiconductors ZnS, ZnSe, ZnTe, CdS, CdTe, HgTe. As Pauling [62] has stated that if the atoms are those of group IVA or two elements symmetrically arranged relative to the IVA, the number of valence electrons is right to permit the formation of a tetrahedral covalent bond between each atom and its four neighbors. Based on Pauling's equation, Equation (80), they are all covalent compounds with very low ionicity, as can be seen from Table 3. However, it should be noted that Pauling's formula, given by Equation (80), is only an approximation based on a single factor of electronegativity. As Pauling [62] has himself stated that in ZnS, for example, the extreme covalent structure of ZnS "places formal charges 2^- on zinc and 2^+ on sulfur. It is probable that the bonds have enough ionic character in this crystal and in others of similar structure to make charges of the atoms nearly zero; for ZnS this would require about 50% ionic character". Other chemists are also ambivalent about the issue, as can be seen from the statement of Cotton and Wilkinson [63] quoted above. This ambiguity notwithstanding, these compound semiconductors can generally be classified as polar covalent compounds unlike rock salt types that are primarily ionic. As shown

in Tables 2 and 3, λ (or λ'') and χ are both less than unity ($\chi < 1, \chi' > 1, \chi'' < \sqrt{c_{11}/c'_{11}}$) for these crystals, giving rise to complex roots for both the (010)[001] and (1$\bar{1}$0)[110] through-cracks, and imaginary roots for the ($\bar{1}$10)[001] through-crack. It can then be inferred that {$\bar{1}$10}⟨001⟩ would constitute a relatively easy cleavage system, while both {010}⟨001⟩ and {1$\bar{1}$0}⟨110⟩ would be deemed difficult. As has been experimentally observed by Margevicius and Gumbsch [33] for GaAs single crystals, and also noted by Perez and Gumbsch [28], the {110} family of planes constitute the easy cleavage plane for polar semiconductors. Furthermore, ⟨110⟩ was seen to be the preferred propagation direction. This is in agreement with the theoretical prediction of the present investigation.

The compound cubic crystals, PbF_2, BaF_2, SrF_2, ThO_2, CaF_2 and UO_2 listed in Tables 1–3 with fluorite structure are primarily ionic solids. With the exception of PbF_2 and BaF_2, $\bar{\lambda} = \lambda' = (1/\lambda)$ is generally lower than unity. As a result, λ (or λ'') and χ are both greater than unity ($\chi > 1, \chi' < 1, \chi'' > \sqrt{c_{11}/c'_{11}}$) for these, like their alkali halide counterparts, giving rise to imaginary roots for both the (010)[001] and (1$\bar{1}$0)[001] through-cracks, and complex roots for the ($\bar{1}$10)[001] through-crack. It can then be inferred that both {010}⟨001⟩ and {1$\bar{1}$0}⟨110⟩ would constitute relatively easy cleavage systems, while {$\bar{1}$10}⟨001⟩ would be deemed difficult. BaF_2 is macroscopically isotropic, while for PbF_2, as shown in Tables 2 and 3, λ (or λ'') and χ are both less than unity ($\chi < 1, \chi' > 1, \chi'' < \sqrt{c_{11}/c'_{11}}$), giving rise to complex roots for both the (010) [001] and (1$\bar{1}$0)[110] through-cracks, and imaginary roots for the ($\bar{1}$10)[001] through-crack. It can then be inferred that {$\bar{1}$10}⟨001⟩ would constitute a relatively easy cleavage system, while both {010}⟨001⟩ and {1$\bar{1}$0}⟨110⟩ would be deemed difficult.

Lastly, $MgAl_2O_4$, with spinel structure, and perovskites $BaTiO_3$ (above the critical temperature, T_c) and $SrTiO_3$, are listed in Tables 1–3. Strontium titanate has, at room temperature, an ideal cubic perovskite structure with TiO_6 octahedra being connected by straight chains [59]. As shown in Tables 2 and 3, λ (or λ'') and χ are both less than unity ($\chi < 1, \chi' > 1, \chi'' < \sqrt{c_{11}/c'_{11}}$), giving rise to complex roots for both the (010) [001] and (1$\bar{1}$0)[110] through-cracks, and imaginary roots for the ($\bar{1}$10)[001] through-crack. It can then be inferred that {$\bar{1}$10}⟨001⟩ would constitute a relatively easy cleavage system, while both {010}⟨001⟩ and {1$\bar{1}$0}⟨110⟩ would be deemed difficult.

Further, the anisotropy of crack propagation direction should deserve a discussion with respect to a difficult spontaneous dislocation emission from the crack tip (or front). Rice and Thomson [68] have proposed a necessary criterion for spontaneous emission of dislocations from the tip or front of an atomically sharp cleavage crack. According to these authors [68], cleavage is favored when the energy required to separate atoms is lower than the energy associated with dislocation emission from the crack tip or front. Although this criterion has not been derived in a rigorous sense, this can broadly be summarized as follows: the crystals, whose dislocations have wide cores and values of the parameter, $b/(s_{66}\gamma_s) \leq 7.5 - 10$, are ductile, whereas those with narrow cores and larger values of the parameter are brittle. Here b is the magnitude of the Burger's vector, and γ_s is the true surface energy of the crack plane. Rice and Thomson [68] have concluded with a certain level of confidence that except iron, sodium and fcc single crystals, no spontaneous or

thermally assisted blunting of a crack tip (front) can occur in the crystals investigated by them, which include W, LiF, NaCl, MgO, Al_2O_3, Si, Ge, C (diamond).

11. Numerical results

First, the following sets of normalized displacements and stresses are defined (stiffnesses, stresses and stress intensity factors are expressed in terms of Pa, Pa and Pa$\sqrt{\text{m}}$, respectively, whereas displacements and thickness are in meter (m)):

$$(u*, v*) = 10^6 \frac{(\sigma^\infty, \tau^\infty)}{K_{\text{I/II}}\sqrt{h}}(u, v),$$

$$\left(\sigma_x^*, \sigma_y^*, \tau_{xy}^*\right) = 10^2 \frac{\sqrt{h}}{K_{\text{I/II}}}(\sigma_x, \sigma_y, \tau_{xy}),$$

in which the half-thickness $h = 100\,\mu\text{m}$ and far-field (applied) mode I/II loadings, σ^∞ and τ^∞ are each 1 MPa. Figures 5 and 6 show the variations of the u^* and v^*, under mode I loading condition, with respect to x-direction, [100], in the vicinity of a semi-infinite crack front in Si single crystal shown in Figure 1.

Figures 7 and 8 depict the variations of u^* and v^*, under mode I loading condition, with respect to x'-direction, [110], in the vicinity of a semi-infinite crack front in Si single crystal shown in Figure 2.

Figures 9–11 show the variations of σ_x^*, σ_y^* and τ_{xy}^*, under mode I loading condition, with respect to x-direction, [100], in the vicinity of a semi-infinite crack front in Si single crystal shown in Figure 1.

Figures 12–14 depict the variations of σ_x^*, σ_y^* and τ_{xy}^*, under mode I loading condition, with respect to x'-direction, [110], in the vicinity of a semi-infinite crack

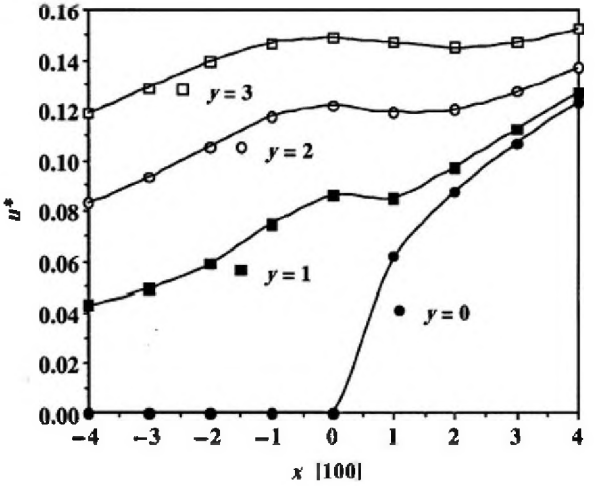

Figure 5. Variation of displacement, u^*, in the vicinity of a (010) [001] crack front (tip) in silicon along x [100] direction (mode I).

front in Si single crystal shown in Figure 2. As expected, comparison of results relating to the displacements and stresses in the vicinity of the crack front pertaining to both the crack systems, shown in Figures 1 and 2 do not reveal any difference of behaviors under mode I loading condition.

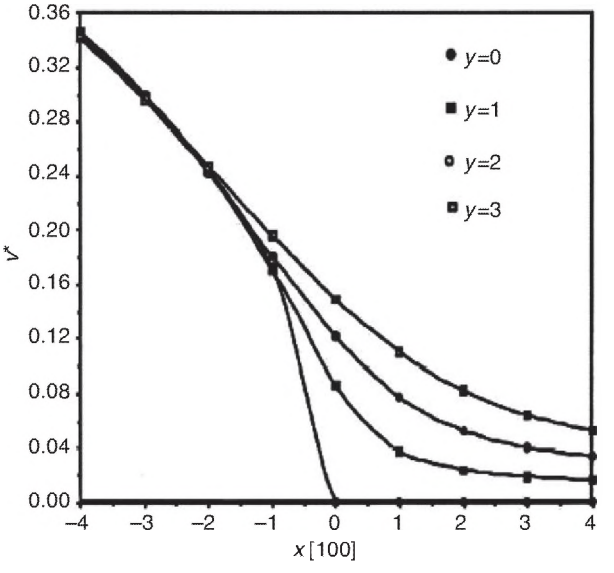

Figure 6. Variation of displacement, v^*, in the vicinity of a (010) [001] crack front (tip) in silicon along x [100] direction (mode I).

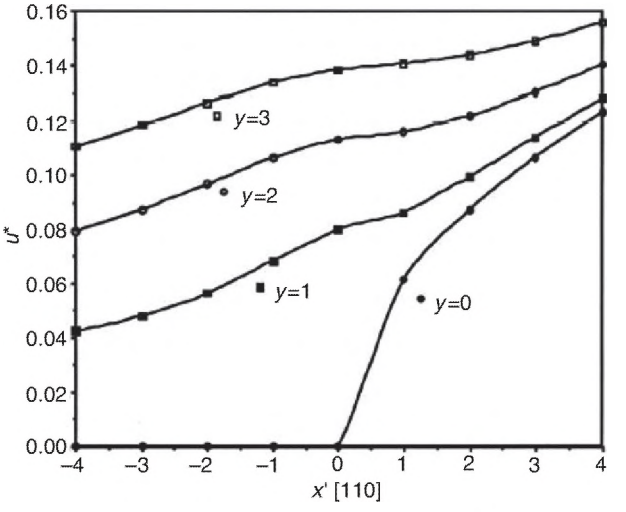

Figure 7. Variation of displacement, u^*, in the vicinity of a $(\bar{1}10)[001]$ crack front (tip) in silicon along x' [110] direction (mode I).

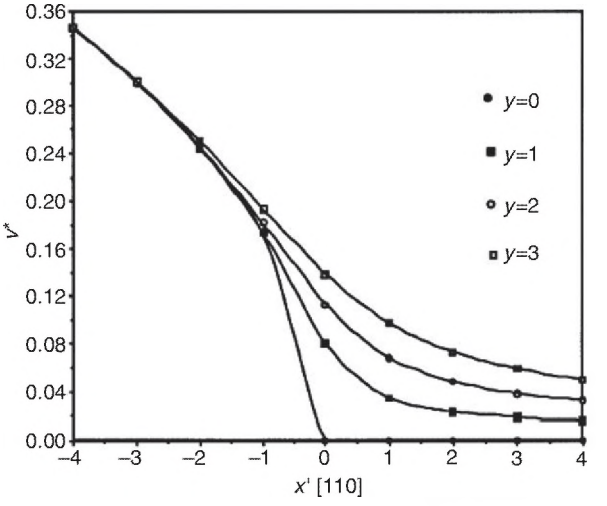

Figure 8. Variation of displacement, v^*, in the vicinity of a $(\bar{1}10)[001]$ crack front (tip) in silicon along x' [110] direction (mode I).

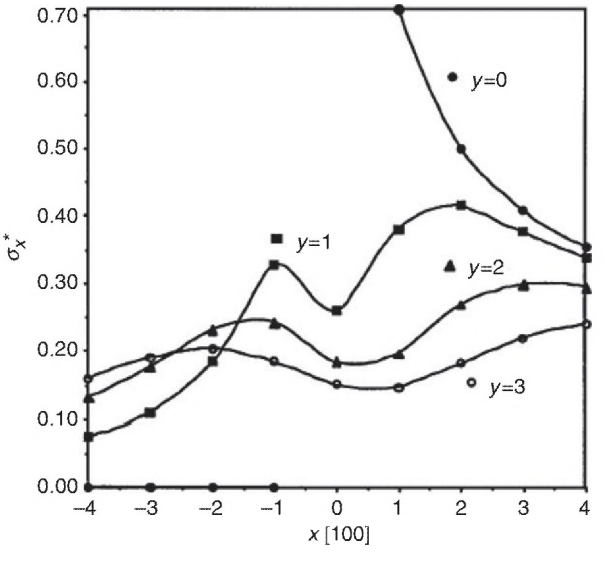

Figure 9. Variation of normal stress, σ_x^*, in the vicinity of a (010) [001] crack front (tip) in silicon along x [100] direction (mode I).

Figures 15 and 16 show the variations of u^* and v^* under mode II loading condition, with respect to x-direction, [100], in the vicinity of a semi-infinite crack front in Si single crystal shown in Figure 1.

Figures 17 and 18 depict the variations of u^* and v^* under mode II loading condition, with respect to x'-direction, [110], in the vicinity of a semi-infinite crack front in Si single crystal shown in Figure 2.

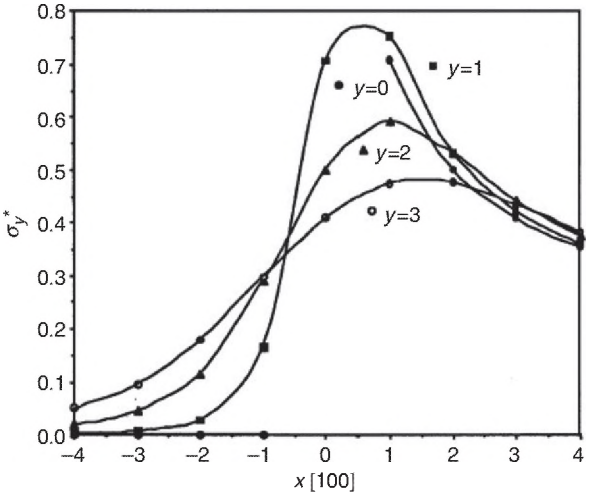

Figure 10. Variation of normal stress, σ_y^*, in the vicinity of a (010) [001] crack front (tip) in silicon along x [100] direction (mode I).

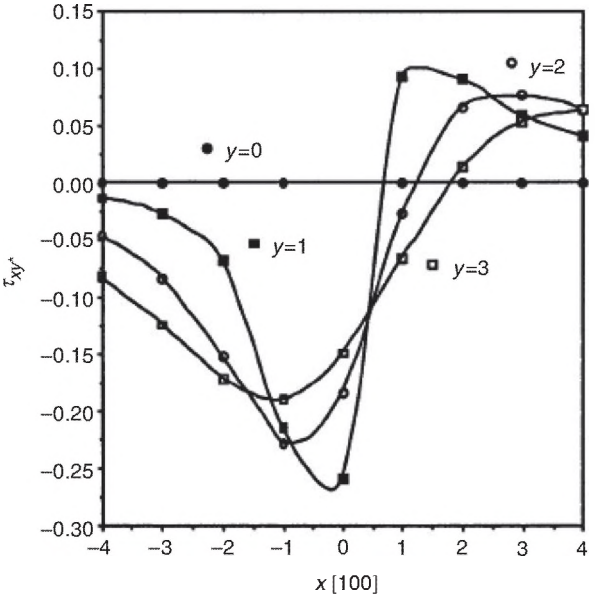

Figure 11. Variation of shear stress, τ_{xy}^*, in the vicinity of a (010) [001] crack front (tip) in silicon along x [100] direction (mode I).

Figures 19–21 show the variations of σ_x^*, σ_y^* and τ_{xy}^*, under mode II loading condition, with respect to x-direction, [100], in the vicinity of a semi-infinite crack front in Si single crystal shown in Figure 1.

Figures 22–24 depict the variations of σ_x^*, σ_y^* and τ_{xy}^*, under mode II loading condition, with respect to x'-direction, [110], in the vicinity of a semi-infinite crack

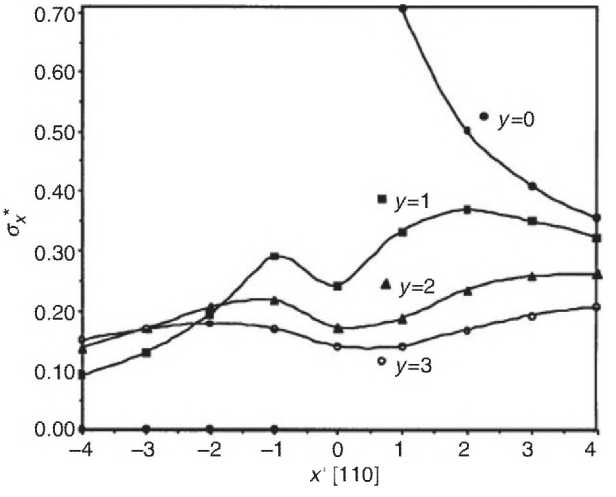

Figure 12. Variation of normal stress, σ_x^*, in the vicinity of a $(\bar{1}10)[001]$ crack front (tip) in silicon along x' [110] direction (mode I).

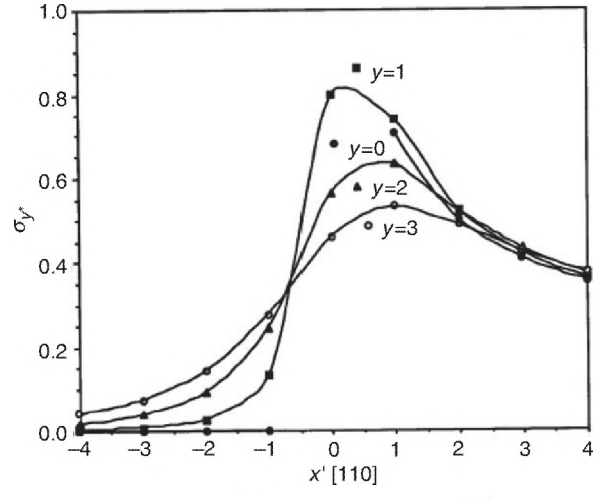

Figure 13. Variation of normal stress, $\sigma_{y'}^*$, in the vicinity of a $(\bar{1}10)[001]$ crack front (tip) in silicon along x' [110] direction (mode I).

front in Si single crystal shown in Figure 2. As expected, comparison of results relating to these displacements and stresses in the vicinity of the crack front pertaining to both crack systems, shown in Figures 1 and 2 do not reveal any difference of behaviors under mode II loading condition.

Figure 25 shows variation of the normalized stress intensity factor, $K^*(z) = K(z)/K_{\text{plane strain}}$, through the thickness of a cubic crystal plate and weakened by any of the three through-cracks investigated here. Figure 25a shows the

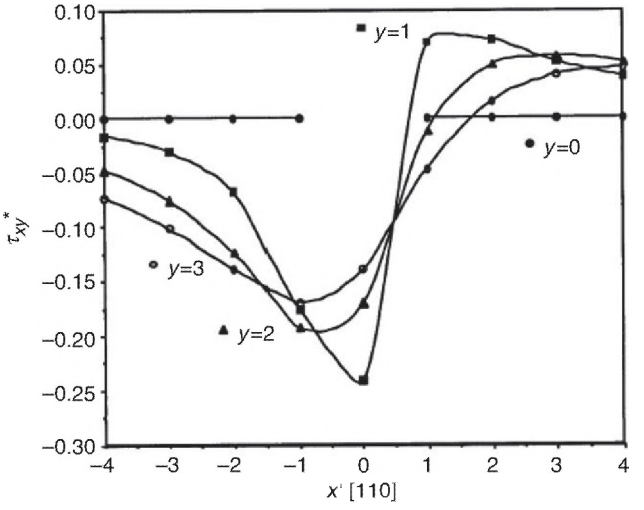

Figure 14. Variation of shear stress, τ^*_{xy}, in the vicinity of a $(\bar{1}10)[001]$ crack front (tip) in silicon along x' [110] direction (mode I).

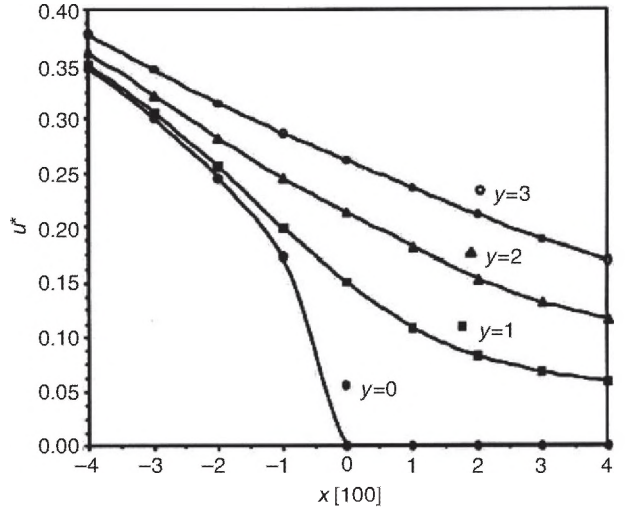

Figure 15. Variation of displacement, u^*, in the vicinity of a (010) [001] crack front (tip) in silicon along x [100] direction (mode II).

through-thickness variation for a far-field symmetrically distributed uniform load, whereas its antisymmetric counterpart is displayed in Figure 25b. Such types of results are, to this date, unavailable in the literature. A large number of terms (about 300,000) are used to replicate the sharp drop to zero at the top and bottom (stress free) surfaces of the cracked cubic crystal plate under investigation.

Table 5a lists the structures and elastic compliance properties of selected rock salt cubic single crystals [61]. In addition, W (bcc) is also included for its interesting

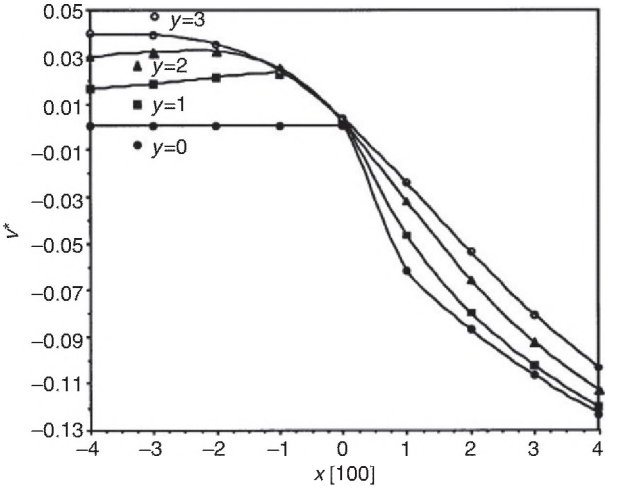

Figure 16. Variation of displacement, v^*, in the vicinity of a (010) [001] crack front (tip) in silicon along x [100] direction (mode II).

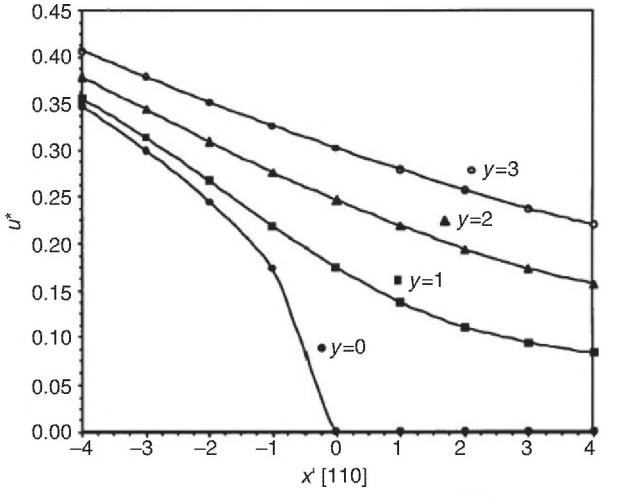

Figure 17. Variation of displacement, u^*, in the vicinity of a $(\bar{1}10)[001]$ crack front (tip) in silicon along x' [110] direction (mode II).

fracture characteristics. Tables 5b and c show the results for computed LCD parameter (energy barrier) and associated bond shear strains at crack deviation from a difficult cleavage system to an easy one, and their correlations with the appropriate anisotropic ratios. Only two crack systems are considered: $\{100\}\langle 001\rangle$ and $\{\bar{1}10\}\langle 001\rangle$.

For alkali halides, $\{100\}\langle 001\rangle$ is deemed to be the preferred cleavage system for reasons explained earlier in Section 10, whereas $\{\bar{1}10\}\langle 001\rangle$ is considered difficult for

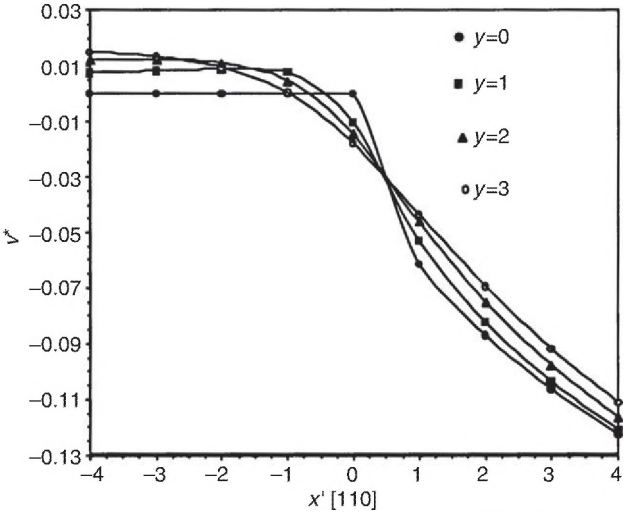

Figure 18. Variation of displacement, v^*, in the vicinity of a $(\bar{1}10)[001]$ crack front (tip) in silicon along x' [110] direction (mode II).

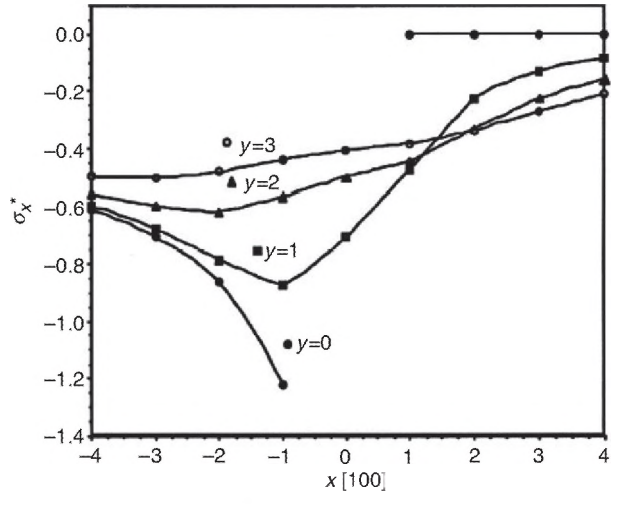

Figure 19. Variation of normal stress, σ_x^*, in the vicinity of a (010) [001] crack front (tip) in silicon along x [100] direction (mode II).

crack propagation. This is illustrated in Figure 26a. Non-vanishing LCD energy barrier implies that a $\{\bar{1}10\}\langle 001\rangle$ through crack in such single crystals would not deflect right at the appropriate Griffith critical stress intensity factor for mixed mode propagation because of the lattice effect, but would require additional bond shear strains for NaCl, KCl, etc. (Table 5b). In the case of non-vanishing LCD barrier, e.g. in NaCl with moderately high anisotropic ratio, $\bar{\lambda} = \lambda' (= 1/\lambda) = 0.6865$, the difficult $\{\bar{1}10\}\langle 001\rangle$ crack may initially get lattice trapped and/or propagate in a

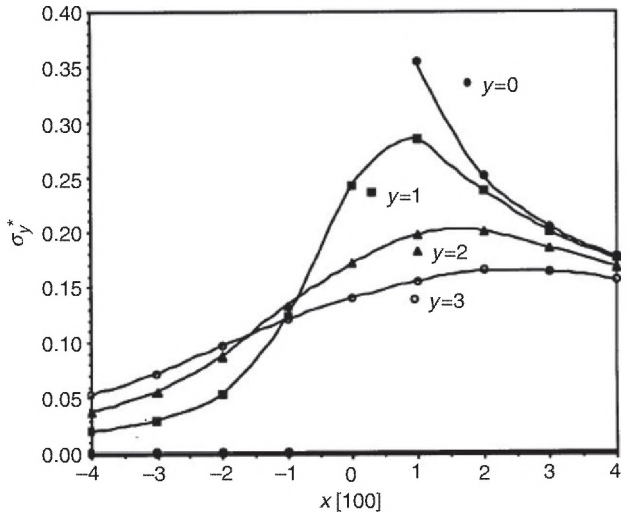

Figure 20. Variation of normal stress, σ_y^*, in the vicinity of a (010) [001] crack front (tip) in silicon along x [100] direction (mode II).

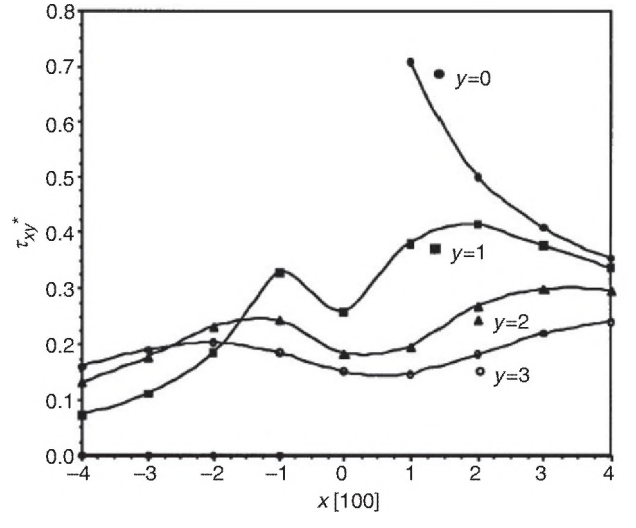

Figure 21. Variation of shear stress, τ_{xy}^*, in the vicinity of a (010) [001] crack front (tip) in silicon along x [100] direction (mode II).

"difficult" manner till an applied load somewhat higher than its Griffith mixed mode counterpart is reached, and then only deflect into the easy cleavage system, $\{100\}\langle 001\rangle$. In addition, the bond breaking would not be continuous but abrupt. In contrast, for an ionic crystal with the very low anisotropic ratio, $\bar{\lambda} = \lambda' \ (= 1/\lambda)$, such as RbBr ($\bar{\lambda} = 0.2855$), LCD barrier vanishes and the difficult $\{\bar{1}10\}\langle 001\rangle$ crack would deflect into its easy counterpart right at the Griffith mixed mode critical stress

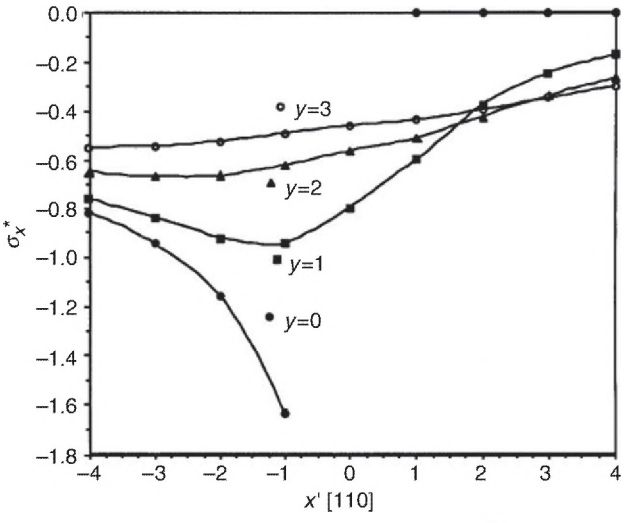

Figure 22. Variation of normal stress, σ_x^*, in the vicinity of a $(\bar{1}10)[001]$ crack front (tip) in silicon along x' [110] direction (mode II).

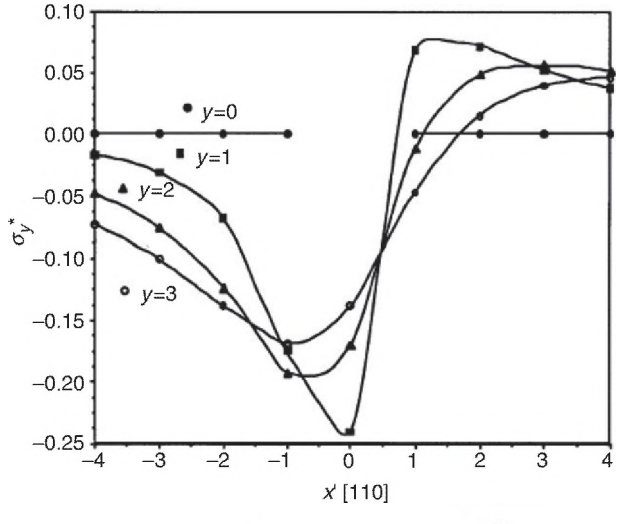

Figure 23. Variation of normal stress, σ_y^*, in the vicinity of a $(\bar{1}10)[001]$ crack front (tip) in silicon along x' [110] direction (mode II).

intensity factor. Reduction of the LCD barrier with the decrease of the anisotropic ratio is quite rapid, as can be seen from Table 5b.

For lithium halides and MgO, $\{\bar{1}10\}\langle 001\rangle$ is deemed to be the preferred cleavage system for reasons explained earlier in Section 10, whereas $\{100\}\langle 001\rangle$ is considered difficult for crack propagation. This is illustrated in Figure 26b. Non-vanishing LCD energy barrier implies that a $\{100\}\langle 001\rangle$ through crack in such single crystals would not deflect right at the appropriate Griffith critical stress intensity factor for mixed

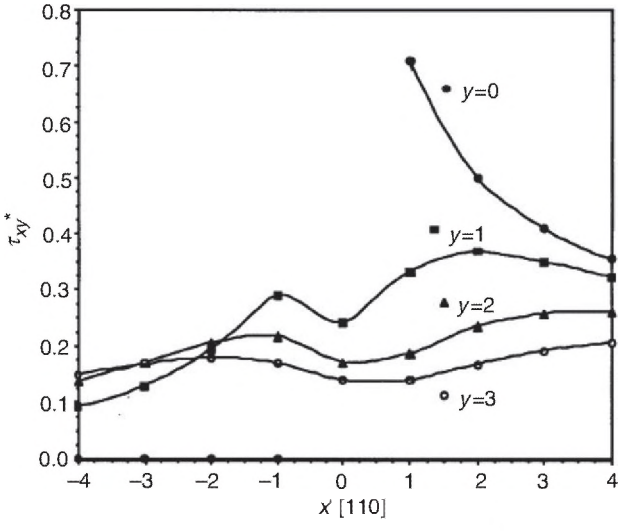

Figure 24. Variation of shear stress, τ^*_{xy}, in the vicinity of a $(\bar{1}10)[001]$ crack front (tip) in silicon along x' [110] direction (mode II).

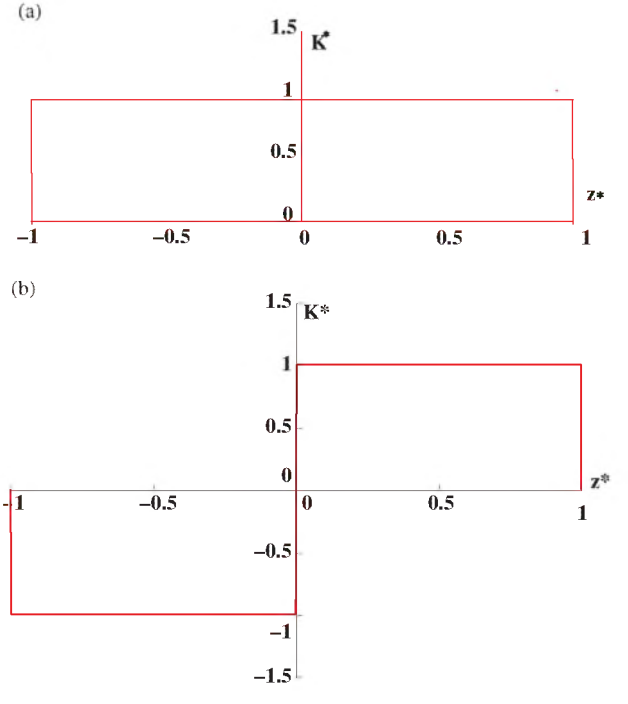

Figure 25. Variation of stress intensity factor through thickness (a) symmetric loading, (b) skew-symmetric loading.

Table 5. (a) Structures and elastic compliance properties of selected rock salt, and tungsten (bcc) cubic single crystals [61]. (b) Anisotropic ratio, lattice crack deviation barrier and associated bond strains in (Na, K and Rb) halide and tungsten (bcc) cubic single crystals. (c) Modified anisotropic ratio, lattice crack deviation barrier and associated bond shear strains in lithium halide and MgO cubic single crystals.

(a)

Crystal (Temp. K)	Structure	Bravais lattice	s_{11} (10^{-2}GPa^{-1})	s_{12} (10^{-2}GPa^{-1})	s_{66} (10^{-2}GPa^{-1})
LiF (room)	Rock salt	fcc	1.1342	−0.3109	1.5924
LiCl (room)	Rock salt	fcc	2.8399	−0.8914	4.0161
LiBr (room)	Rock salt	fcc	3.6691	−1.1852	5.2356
MgO (300)	Rock salt	fcc	0.4024	−0.0936	0.6461
NaF (room)	Rock salt	fcc	1.1445	−0.2291	3.5714
NaCl (room)	Rock salt	fcc	2.2457	−0.4570	7.8740
NaBr (300)	Rock salt	fcc	2.8036	−0.5646	10.02
KF (room)	Rock salt	fcc	1.6584	−0.3062	7.8125
KCl (295)	Rock salt	fcc	2.6009	−0.3824	15.8730
KBr (room)	Rock salt	fcc	3.0363	−0.4359	19.802
RbF (room)	Rock salt	fcc	1.9046	−0.3426	10.9890
RbCl (room)	Rock salt	fcc	2.8818	−0.4131	21.0526
RbBr (300)	Rock salt	fcc	3.3093	−0.4472	26.3158
W (20)	bcc (hybridized)	bcc	0.2389	−0.0664	0.6130

(b)

Crystal (Temp. K)	Anisotropic ratio $\bar{\lambda} = \lambda' (= 1/\lambda)$	Easy cleavage system (ECS)	Difficult cleavage system (DCS)	Bond shear strain at lattice crack deviation (γ_{bd})	Lattice crack deviation (LCD) parameter in DCS (ΔK^*)
NaF (room)	0.7692	{010}⟨001⟩	{$\bar{1}$10}⟨001⟩	0.3993	0.4637
NaCl (room)	0.6865	{010}⟨001⟩	{$\bar{1}$10}⟨001⟩	0.3694	0.4177
NaBr (300)	0.6723	{010}⟨001⟩	{$\bar{1}$10}⟨001⟩	0.3574	0.3996
KF (room)	0.5030	{010}⟨001⟩	{$\bar{1}$10}⟨001⟩	0.2597	0.2663
KCl (295)	0.3759	{010}⟨001⟩	{$\bar{1}$10}⟨001⟩	0.1170	0.1070
KBr (room)	0.3507	{010}⟨001⟩	{$\bar{1}$10}⟨001⟩	0.0494	0.0447

(*continued*)

Table 5. Continued.

(b)

Crystal (Temp. K)	Anisotropic ratio $\bar{\lambda} = \lambda'(= 1/\lambda)$	Easy cleavage system (ECS)	Difficult cleavage system (DCS)	Bond shear strain at lattice crack deviation (γ_{bd})	Lattice crack deviation (LCD) parameter in DCS (ΔK^*)
RbF (room)	0.4090	{010}⟨001⟩	{$\bar{1}$10}⟨001⟩	0.1688	0.1619
RbCl (room)	0.3130	{010}⟨001⟩	{$\bar{1}$10}⟨001⟩	0.0140	0.0025
RbBr (300)	0.2855	{010}⟨001⟩	{$\bar{1}$10}⟨001⟩	0.0	0.0
W (20)	~1	{010}⟨001⟩	{110}⟨001⟩	0.4773	0.4011

(c)

Crystal (Temp. K)	Modified anisotropic ratio $\bar{\lambda}' = \lambda(= 1/\lambda')$	Easy cleavage system (ECS)	Difficult cleavage system (DCS)	Bond shear strain at lattice crack deviation (γ_{bd})	Lattice crack deviation (LCD) parameter in DCS (ΔK^*)
LiF (room)	0.5510	{$\bar{1}$10}⟨001⟩	{100}⟨001⟩	0.2877	0.3284
LiCl (room)	0.5382	{$\bar{1}$10}⟨001⟩	{100}⟨001⟩	0.2300	0.2412
LiBr (room)	0.5393	{$\bar{1}$10}⟨001⟩	{100}⟨001⟩	0.2350	0.2534
MgO (300)	0.6513	{$\bar{1}$10}⟨001⟩	{100}⟨001⟩	0.2502	0.2350

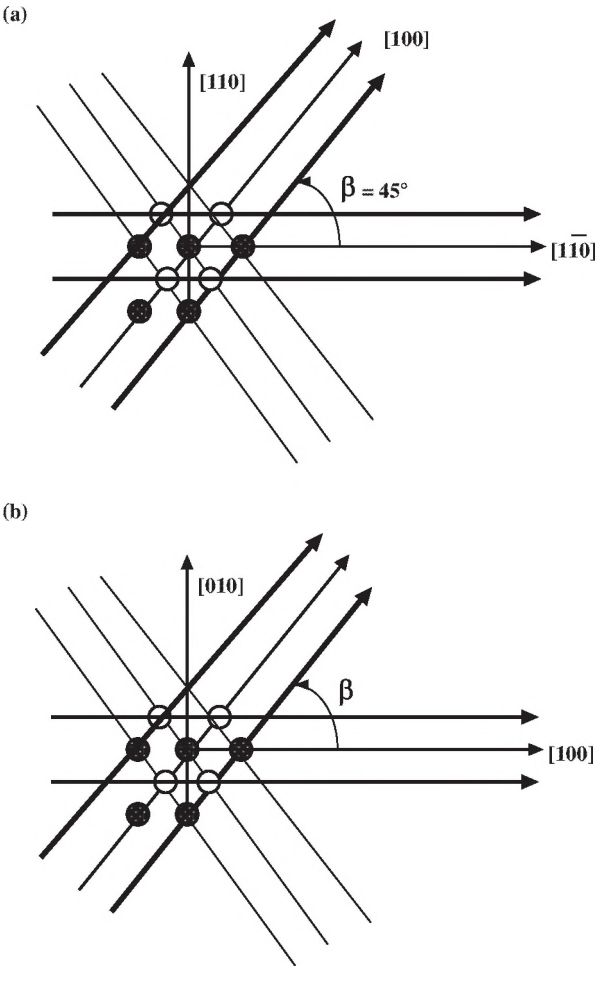

Figure 26. Lattice crack deviation in cubic crystals: (a) Na, K and Rb halides; (b) Li halides and MgO.

mode propagation because of the lattice effect, but would require additional bond shear strains (Table 5c). Again, the bond breaking would not be continuous but abrupt, when the LCD parameter is high. Here also, the correlation of the LCD barrier with the modified anisotropic ratio is clearly observable from Table 5c.

It is interesting to note, in connection with bcc metals in general and W in particular, that according to Griffith's fracture theory, only surfaces with minimum surface energy should be favored as the plane of crack propagation. Notwithstanding the success of this approach, there are exceptions to this rule, the most enigmatic being the {100} cleavage of bcc transition metals [34], especially macroscopically isotropic tungsten (W). Although the close packed {110} surface has lower surface energy, γ, the preferred cleavage plane has been observed by Hull and Beardmore [35] to be {100}. For W, {100}⟨001⟩ is deemed to be the preferred cleavage system for reasons of having d^2sp^3 hybridized orbitals, as discussed in Section 10, whereas

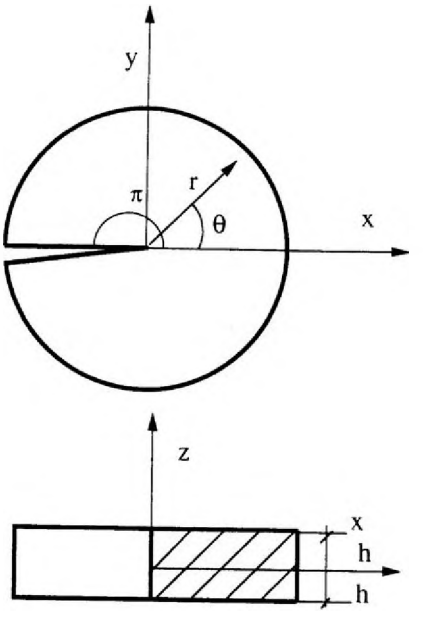

Figure 27. Schematic of a through-thickness semi-infinite crack in a cubic monocrystalline plate and the associated coordinate systems.

$\{\bar{1}10\}\langle 001\rangle$ is considered difficult for crack propagation. Non-vanishing LCD energy barrier implies that a $\{\bar{1}10\}\langle 001\rangle$ through crack in a W single crystal would not deflect right at the appropriate Griffith critical stress intensity factor for mixed mode propagation because of the lattice effect, but would require additional bond shear strains (Table 5b). In the case of non-vanishing LCD barrier, the difficult $\{\bar{1}10\}\langle 001\rangle$ crack may initially get lattice trapped and/or propagate in a "difficult" manner till an applied load somewhat higher than its Griffith mixed mode counterpart is reached, and then only deflect onto the easy cleavage system, $\{100\}\langle 001\rangle$. In addition, the bond breaking would not be continuous but abrupt.

12. Summary and conclusions

Derivation of the three-dimensional stress field at the front of a through-crack weakening a cubic single crystal plate has remained a challenge to the researchers in the field of mechanics of solids/materials. A heretofore unavailable eigenfunction expansion technique, based in part on separation of the z-variable, is developed to derive three-dimensional asymptotic displacement and stress fields in the vicinity of the front of a semi-infinite through-crack weakening an infinite plate made of a homogeneous cubic single crystal. Crack-side boundary conditions and those that are prescribed on the top and bottom (free, fixed or lubricated) surfaces of the cubic crystal plate are exactly satisfied. Explicit expressions for singular stress fields in the vicinity of the front of through cracks, weakening cubic single crystal plates subjected to far-field extension/bending (mode I), sliding shear/twisting (mode II)

and antiplane shear (mode III) loadings are presented. Expressions for displacements and stresses derived here reduce to their two-dimensional counterparts. Extensive numerical results for the displacement and stress fields are also presented. Of special significance are the numerical results pertaining to the through-thickness variations of stress intensity factors for uniform load and its skew-symmetric counterpart that also satisfy the stress free boundary conditions on the top and bottom surfaces of the cracked cubic crystal plates under investigation.

The present investigation considers three through-crack systems, (010)[001] with the [100] propagation direction, $(\bar{1}10)[001]$ with the [110] propagation direction, and $(1\bar{1}0))[110]$ with the [001] propagation direction, weakening cubic crystals. The choice for easier (or more difficult) cleavage system depends on the normalized elastic parameter, χ, χ' or χ'', which, in turn, depends on the respective anisotropic ratio, $\bar{\lambda} = 1/\lambda$, $\bar{\lambda}' = 1/\lambda'$, or $\bar{\lambda}'' = 1/\lambda''$. $\bar{\lambda} = 1/\lambda$. is a function of the elastic stiffness coefficients computed with respect to the cube edges.

Atomistic modeling of cracks requires consideration of both the long range elastic interactions and the short range chemical reactions. The Griffith–Irwin approach does not take the latter into account. Besides, the experimentally observed deflected crack would propagate under mixed mode (i.e. opening and shear mode) and its relationship with the lattice trapping phenomenon has not been studied in the literature. These concerns have necessitated introduction of a new concept of the lattice crack deviation (LCD) parameter, and its quantification. The LCD parameter is, like its lattice trapping counterpart, also a manifestation of the discreteness of the lattice itself. It also is influenced by the direction in which the crack front bonds are broken. The critical stress, σ_{sc}^{+}, responsible for shear kinking of bonds which follow zigzag paths, has been obtained in a manner analogous to micro-buckling and kink band formation and propagation in a unidirectional fiber reinforced composite specimen, such as carbon fiber reinforced epoxy, with initial fiber waviness or misalignment. The primary difference is, however, that here although the applied loading is tensile (and not compressive), the bond will initially be compressed and shear-kinked because of the snapping effect. The present analysis is based on elastic plane inextensional deformation of the bond. The dominant effect of the shear deformation would cause the onset of a critical state in the parallel atomic bonds, responsible for a collective phenomenon (domino effect) of kinked bond–band formation and propagation, leading to crack turning from a more difficult cleavage system to an easier one.

Additionally, the relationships of the easier cleavage planes based on the present solutions with the structural chemistry aspects of various single crystals, such as bcc alkali metals, bcc transition alkali metals, fcc transition metals, group IVA (diamond cubic) elements, usually ionic compounds (rock salt and fluorite structures), covalent compounds (zinc blende structure), etc, are discussed here. Various aspects of the underlying structural chemistry of these cubic crystals, such as Bravais lattice type, bonding (covalent, ionic and metallic), bonding (including hybridized) orbitals, electro-negativity of constituent atoms in a compound, polarity, etc, play key roles in the determination of easy cleavage planes and propagation directions. The present solutions are consistent with the some of the results pertaining to structure-fracture property relationships of cubic single crystals obtained by the structural chemists and materials scientists.

Finally, the results for computed LCD parameter (energy barrier) and associated bond shear strains at crack deviation from a difficult cleavage system onto an easy one, and their correlations with the appropriate anisotropic ratios are presented. Only two crack systems are considered: $\{100\}\langle 001\rangle$ and $\{\bar{1}10\}\langle 001\rangle$. For example, for alkali halides, $\{100\}\langle 001\rangle$ is deemed to be the preferred cleavage system for reasons explained earlier in Section 10, whereas $\{\bar{1}10\}\langle 001\rangle$ is considered difficult for crack propagation. Non-vanishing LCD energy barrier implies that a $\{\bar{1}10\}\langle 001\rangle$ through crack in such single crystals would not deflect right at the appropriate Griffith critical stress intensity factor for mixed mode propagation because of the lattice effect, but would require additional bond shear strains for NaCl, KCl, etc. (Table 5b). In the case of non-vanishing LCD barrier, e.g. in NaCl with moderately high anisotropic ratio, $\bar{\lambda} = \lambda' \ (= 1/\lambda) = 0.6865$, the difficult $\{\bar{1}10\}\langle 001\rangle$ crack may initially get lattice trapped and/or propagate in a "difficult" manner till an applied load somewhat higher than its Griffith mixed mode counterpart is reached, and then only deflect onto the easy cleavage system, $\{100\}\langle 001\rangle$. In addition, the bond breaking would not be continuous but abrupt. For an ionic crystal with the very low anisotropic ratio, $\bar{\lambda} = \lambda' \ (= 1/\lambda)$, such as RbBr $\bar{\lambda} = 0.2855$, LCD barrier vanishes and the difficult $\{\bar{1}10\}\langle 001\rangle$ crack would deflect into its easy counterpart right at the Griffith mixed mode critical stress intensity factor. Reduction of the LCD barrier with the decrease of the appropriate anisotropic ratio is quite rapid.

In single crystals of alkali halides (rock salt structure), when subjected to tensile stress, σ^+, applied along, e.g. [010] direction, bonds will ultimately fail in tension, and no rotation or shear deformation effect is expected to influence bond failure. No crack deviation is expected in such cases. In contrast, when single crystals of bcc metals, lithium salts or MgO, are subjected to tensile stress, σ^+, applied along, e.g. [010] direction, bonds follow zigzag paths, and the bond failure would primarily be governed by shear deformation, and will generally lead to crack deflection.

References

[1] J.A. Collins, *Failure of Materials in Mechanical Design*, John Wiley & Sons, New York, 1981, Chapter 13.
[2] W. Nowacki, *Crystal Data, Systematic Tables*, Monograph No. 6, American Crystallographic Association, 1967.
[3] J.F. Shackelford, *Introduction to Materials Science for Engineers*, Prentice-Hall, Upper Saddle River, NJ, 2000.
[4] A.N. Stroh, Phil. Mag. 7 (1958) p.625.
[5] J.D. Eshelby, W.T. Read and W. Shockley, Acta Metall. 1 (1953) p.251.
[6] J.F. Nye, *Physical Properties of Crystals*, Oxford University Press, Oxford, 1979.
[7] A. Kelley and N.H. Macmillan, *Strong Solids*, 3rd ed., Oxford University Press, New York, 1986.
[8] G.C. Sih, P.C. Paris and G.R. Irwin, Int. J. Fract. Mech. 1 (1965) p.189.
[9] G.P. Cherepanov, *Mechanics of Brittle Fracture*, McGraw-Hill, New York, 1979.
[10] T.L. Sham and Y. Zhou, Int. J. Fract. 40 (1989) p.13.
[11] I.I. Argatov and S.A. Nazarov, J. Appl. Math. Mech. 66 (2002) p.491.
[12] J. Samuels and S.G. Roberts, Proc. Roy. Soc. Lond. Math. Phys. Sci. 421 (1989) p.1.
[13] D. Clarke, Semiconduct. Semimet. 37 (1992) p.79.

[14] C.F. St. John, Phil. Mag. 32 (1975) p.1193.
[15] M. Brede and P. Haasen, Acta Metall. 36 (1988) p.2003.
[16] G. Michot, Cryst. Properties Preparations 17–18 (1988) p.55.
[17] A. George and G. Michot, Mater. Sci. Eng. A 164 (1993) p.118.
[18] D. Zhao, D. Haneman and N.S. McAlpine, Surf. Sci. 369 (1996) p.76.
[19] T. Cramer, A. Wanner and P. Gumbsch, Phys. Status Solidi A 164 (1997) p.R5.
[20] J.A. Hauch, D. Holland, M. Marder and H. Swinny, Phys. Rev. Lett. 82 (1999) p.3823.
[21] F. Ebrahimi and L. Kalwani, Mater. Sci. Eng. A 268 (1999) p.116.
[22] T. Cramer, A. Wanner and P. Gumbsch, Phys. Rev. Lett. 85 (2000) p.788.
[23] D. Sherman, J. Mech. Phys. Solid 53 (2005) p.2742.
[24] R.F. Cook, J. Mater. Sci. 41 (2006) p.841.
[25] D. Sherman, M. Markovitz and O. Barkai, J. Mech. Phys. Solid 56 (2008) p.376.
[26] J.R. Kermode, T. Albaret, D. Sherman, N. Bernstein, P. Gumbsch, M.C. Payne, G. Csányi and A. De Vita, Nature 455 (2008) p.1224.
[27] J.C.H. Spence, Y.M. Huang and O. Sankey, Acta Metall. Mater. 41 (1993) p.2815.
[28] R. Perez and P. Gumbsch, Phys. Rev. Lett. 84 (2000) p.5347.
[29] J.G. Swadener, M.I. Baskes and M. Nastasi, Phys. Rev. Lett. 89 (2002) p.085503.
[30] N. Bernstein and D.W. Hess, Phys. Rev. Lett. 91 (2003) p.025501.
[31] T. Hoshi, R. Takayama, Y. Iguchi and T. Fujiwara, Phys. B: Condens. Matter 376–377 (2006) p.975.
[32] M.J. Buehler, H. Tang, A.C.T. van Duin and W.A. Goddard III, Phys. Rev. Lett. 99 (2007) p.165502.
[33] R.W. Margevicius and P. Gumbsch, Phil. Mag. A 78 (1998) p.567.
[34] K. Sauthoff, M. Wenderoth, A.J. Heinrich, M.A. Rosentreter, K.J. Engel, T.C.G. Reusch and R.G. Ulrich, Phys. Rev. B 60 (1999) p.4789.
[35] D. Hull and P. Beardmore, Int. J. Fract. Mech. 2 (1966) p.468.
[36] R.A. Ayres and D.F. Stein, Acta Metall. 19 (1971) p.789.
[37] G.M. Pharr, D.M. Barnett and W.D. Nix, Scripta Metall. 12 (1978) p.973.
[38] J. Riedle, P. Gumbsch and H.F. Fischmeister, Phys. Rev. Lett. 76 (1996) p.3594.
[39] R. Thomson, C. Hsieh and V. Rana, J. Appl. Phys. 42 (1971) p.3154.
[40] J.E. Sinclair and B.R. Lawn, Proc. Roy. Soc. Lond. Math. Phys. Sci. 329 (1972) p.83.
[41] J.E. Sinclair, Phil. Mag. 31 (1975) p.647.
[42] W.A. Curtin, J. Mater. Res. 5 (1990) p.1549.
[43] S. Kohloff, P. Gumbsch and H.F. Fischmeister, Phil. Mag. A 64 (1991) p.851.
[44] R.A. Chaudhuri and M. Xie, Compos. Sci. Tech. 60 (2000) p.2565.
[45] R.A. Chaudhuri, Int. J. Fract. 121 (2003) p.95.
[46] M. Xie and R.A. Chaudhuri, Compos. Struct. 40 (1998) p.137.
[47] R.A. Chaudhuri and M. Xie, Compos. Sci. Tech. 60 (2000) p.2503.
[48] H.S. Carslaw, *Introduction to the Theory of Fourier Series and Integrals*, 3rd ed., Dover, New York, 1930.
[49] C.H. Wilcox, J. Elasticity 9 (1979) p.221.
[50] M. Xie and R.A. Chaudhuri, Compos. Struct. 54 (2001) p.509.
[51] J.S.H. Chiu and R.A. Chaudhuri, Compos. Struct. 58 (2002) p.129.
[52] R.A. Chaudhuri and M. Xie, Compos. Struct. 40 (1998) p.129.
[53] R.A. Chaudhuri and S.H.J. Chiu, Compos. Struct. 78 (2007) p.254.
[54] R.A. Chaudhuri and S.H.J. Chiu, Compos. Struct. 89 (2009) p.475.
[55] T.H. Courtney, *Mechanical Behavior of Materials*, 2nd ed., McGraw-Hill, New York, 2000.
[56] R.A. Chaudhuri, J. Compos. Mater. 25 (1991) p.1244.
[57] R.A. Chaudhuri and H.J. Garala, J. Compos. Mater. 29 (1995) p.1695 (see also Errata for Tables 7–10, ibid. 30 (1996) p.138).

[58] R.A. Chaudhuri, M. Xie and H.J. Garala, J. Compos. Mater. 30 (1996) p.672.
[59] R.E. Newnham, *Structure–Property Relations*, Springer-Verlag, New York, 1975.
[60] R.A. Chaudhuri, Compos. Struct. 92 (2010) p.395.
[61] G. Simmons and H. Wang, *Single Crystal Elastic Constants and Calculated Aggregate Properties: A Handbook*, MIT Press, Cambridge, MA, 1971.
[62] L. Pauling, *The Chemical Bond*, Cornell University Press, Ithaca, NY, 1967.
[63] F.A. Cotton and G. Wilkinson, *Advanced Inorganic Chemistry*, 4th ed., John Wiley & Sons, New York, 1980.
[64] A.L. Companion, *Chemical Bonding*, McGraw-Hill, New York, 1964.
[65] T. Hoshi and T. Fujiwara, J. Phys. Soc. Jpn 69 (2000) p.3773.
[66] W.A. Harrison, *Electronic Structure and Properties of Solids*, W.H. Freeman & Co., San Francisco, 1980.
[67] D.J. Weidner and G. Simmons, J. Geophys. Res. 77 (1972) p.826.
[68] J.R. Rice and R. Thomson, Phil. Mag. 29 (1974) p.73.
[69] R.A. Chaudhuri, Compos. Struct. 92 (2010) p.1977.
[70] R.A. Chaudhuri, Compos. Struct., in review.

Appendix 1. Details of the derivation of the solution involving complex roots for a (010) [001] through-crack (mode I/II loading)

Some of the details of the mathematical derivation of the solution, involving complex roots, for a cubic crystal plate, weakened by (010) [001] through-crack and subjected to mode I/II loading (Section 5, Case (a)), are presented here. The components of displacement that satisfy the equilibrium Equations (1) can be expressed in the following form:

$$u(x,y,z) = \left(\bar{\bar{D}}_1 i\sin(kz) + \bar{\bar{D}}_2\cos(kz)\right)(ik)^s\left[\bar{A}_1(x+(\xi+i\eta)y)^s + \bar{A}_2(x+(\xi-i\eta)y)^s + \bar{A}_3(x+(-\xi+i\eta)y)^s + \bar{A}_4(x+(-\xi-i\eta)y)^s\right], \tag{81a}$$

$$v(x,y,z) = \left(\bar{\bar{D}}_1 i\sin(kz) + \bar{\bar{D}}_2\cos(kz)\right)(ik)^s\left[\bar{B}_1(x+(\xi+i\eta)y)^s + \bar{B}_2(x+(\xi-i\eta)y)^s + \bar{B}_3(x+(-\xi+i\eta)y)^s + \bar{B}_4(x+(-\xi-i\eta)y)^s\right], \tag{81b}$$

$$w(x,y,z) = \left(\bar{\bar{D}}_1\cos(kz) + \bar{\bar{D}}_2 i\sin(kz)\right)(ik)^{s+1}\left[\bar{C}_1(x+(\xi+i\eta)y)^{s+1} + \bar{C}_2(x+(\xi-i\eta)y)^{s+1} + \bar{C}_3(x+(-\xi+i\eta)y)^s + \bar{C}_4(x+(-\xi-i\eta)y)^s\right], \tag{81c}$$

where ξ and η are as given in Equation (22), and $\overline{A}_k$, $\overline{B}_k$, $\overline{C}_k$, $k=1,\ldots,4$, are undetermined coefficients. It may be noted that $\overline{B}_k$ can be expressed in terms of the corresponding $\overline{A}_k$, $k=1,\ldots,4$ by using Equations (15) and (21).

$$\bar{B}_1 = (H_1 + iH_2)\bar{A}_1, \quad \bar{B}_2 = (H_1 - iH_2)\bar{A}_2, \tag{82a, b}$$

$$\bar{B}_3 = (-H_1 + iH_2)\bar{A}_3, \quad \bar{B}_4 = -(H_1 + iH_2)\bar{A}_4, \tag{82c, d}$$

in which

$$H_1 = -\frac{\xi(c_{11}+c_{66})}{(c_{12}+c_{66})}, \quad H_2 = \frac{\eta(c_{11}-c_{66})}{(c_{12}+c_{66})}. \tag{83a, b}$$

The corresponding stress field can easily be obtained from Equation (81). It is convenient to express the components of the displacement vector and stress tensor, in terms of the cylindrical polar coordinate system (r,θ,z); see Figure 27. Expressing

$$\rho\cos(\psi) = r(\cos(\theta) + \xi\sin(\theta)), \quad \rho\sin(\psi) = r(\eta\sin(\theta)), \tag{84a}$$

$$\rho' \cos(\psi) = r(\cos(\theta) - \xi \sin(\theta)), \quad \rho' \sin(\psi) = r(\eta \sin(\theta)), \tag{84b}$$

in which

$$\rho = r\left\{(\cos(\theta) + \xi \sin(\theta))^2 + \eta^2 \sin^2(\theta)\right\}^{1/2}, \tag{85a}$$

$$\rho' = r\left\{(\cos(\theta) - \xi \sin(\theta))^2 + \eta^2 \sin^2(\theta)\right\}^{1/2}, \tag{85b}$$

and

$$\cos(\psi(\theta)) = \frac{\cos(\theta) + \xi \sin(\theta)}{\left\{(\cos(\theta) + \xi \sin(\theta))^2 + \eta^2 \sin^2(\theta)\right\}^{1/2}}, \tag{86a}$$

$$\sin(\psi(\theta)) = \frac{\eta \sin(\theta)}{\left\{(\cos(\theta) + \xi \sin(\theta))^2 + \eta^2 \sin^2(\theta)\right\}^{1/2}}, \tag{86b}$$

$$\cos(\psi'(\theta)) = \frac{\cos(\theta) - \xi \sin(\theta)}{\left\{(\cos(\theta) - \xi \sin(\theta))^2 + \eta^2 \sin^2(\theta)\right\}^{1/2}}, \tag{86c}$$

$$\sin(\psi'(\theta)) = \frac{\eta \sin(\theta)}{\left\{(\cos(\theta) - \xi \sin(\theta))^2 + \eta^2 \sin^2(\theta)\right\}^{1/2}}, \tag{86d}$$

the general asymptotic form for the displacement and stress fields can be written as follows:

$$\begin{aligned} u(r,\theta,z) = r^s D_b(z)(ik)^s \Big[&\left\{(\cos(\theta) + \xi \sin(\theta))^2 + \eta^2 \sin^2(\theta)\right\}^{s/2} \left\{A_1 \cos(s\psi) + A_2 \sin(s\psi)\right\} \\ &+ \left\{(\cos(\theta) - \xi \sin(\theta))^2 + \eta^2 \sin^2(\theta)\right\}^{s/2} \left\{A_3 \cos(s\psi') + A_4 \sin(s\psi')\right\} \Big] + O(r^{s+2}), \end{aligned} \tag{87a}$$

$$\begin{aligned} v(r,\theta,z) = r^s D_b(z)(ik)^s \Big[&\left\{(\cos(\theta) + \xi \sin(\theta))^2 + \eta^2 \sin^2(\theta)\right\}^{s/2} \\ &\times \left\{(H_1 A_1 + H_2 A_2)\cos(s\psi) + (H_1 A_2 - H_2 A_1)\sin(s\psi)\right\} \\ &+ \left\{(\cos(\theta) - \xi \sin(\theta))^2 + \eta^2 \sin^2(\theta)\right\}^{s/2} \\ &\times \left\{-(H_1 A_3 - H_2 A_4)\cos(s\psi') - (H_1 A_4 + H_2 A_3)\sin(s\psi')\right\} + O(r^{s+2}), \end{aligned} \tag{87b}$$

$$w(r,\theta,z) = O(r^{s+1}), \tag{87c}$$

and

$$\begin{aligned} \sigma_x(r,\theta,z) = r^{s-1} D_b(z)(ik)^s s \Big\{ &\left\{(\cos(\theta) + \xi \sin(\theta))^2 + \eta^2 \sin^2(\theta)\right\}^{(s-1)/2} [(A_1\{c_{11} + (\xi H_1 - \eta H_2)c_{12}\right\} \\ &+ A_2\left\{(\eta H_1 + \xi H_2)c_{12}\right\}) \cos((s-1)\psi) + (-A_1\left\{(\eta H_1 + \xi H_2)c_{12}\right\} \\ &+ A_2\{c_{11} + (\xi H_1 - \eta H_2)c_{12}\}) \sin((s-1)\psi)] + \left\{(\cos(\theta) - \xi \sin(\theta))^2 \right. \\ &\left. + \eta^2 \sin^2(\theta)\right\}^{(s-1)/2} [(A_3\{c_{11} + (\xi H_1 - \eta H_2)c_{12}\} - A_4\left\{(\eta H_1 + \xi H_2)c_{12}\right\}) \cos((s-1)\psi') \\ &+ (A_3\left\{(\eta H_1 + \xi H_2)c_{12}\right\} + A_4\{c_{11} + (\xi H_1 - \eta H_2)c_{12}\}) \sin((s-1)\psi')] \Big\} + O(r^{s+1}), \end{aligned} \tag{88a}$$

$$\sigma_y(r,\theta,z) = r^{s-1}D_b(z)(ik)^s s\Big\langle\big\{(\cos(\theta)+\xi\sin(\theta))^2+\eta^2\sin^2(\theta)\big\}^{(s-1)/2}$$
$$\times\big[(A_1\{c_{12}+(\xi H_1-\eta H_2)c_{11}\}+A_2\{(\eta H_1+\xi H_2)c_{11}\})\cos((s-1)\psi)$$
$$+(-A_1\{(\eta H_1+\xi H_2)c_{11}\}+A_2\{c_{12}+(\xi H_1-\eta H_2)c_{11}\})\sin((s-1)\psi)\big]$$
$$+\big\{(\cos(\theta)-\xi\sin(\theta))^2+\eta^2\sin^2(\theta)\big\}^{(s-1)/2}\big[(A_3\{c_{12}+(\xi H_1-\eta H_2)c_{11}\}$$
$$-A_4\{(\eta H_1+\xi H_2)c_{11}\})\cos((s-1)\psi')+(A_3\{(\eta H_1+\xi H_2)c_{11}\}$$
$$+A_4\{c_{12}+(\xi H_1-\eta H_2)c_{11}\})\sin((s-1)\psi')\big]\Big\rangle+O(r^{s+1}), \tag{88b}$$

$$\tau_{xy}(r,\theta,z) = r^{s-1}D_b(z)(ik)^s s c_{66}\Big\langle\big\{(\cos(\theta)+\xi\sin(\theta))^2+\eta^2\sin^2(\theta)\big\}^{(s-1)/2}\big[\big\{A_1(\xi+H_1)$$
$$+A_2(\eta+H_2)\big\}\cos((s-1)\psi)+\big\{-A_1(\eta+H_2)+A_2(\xi+H_1)\big\}\sin((s-1)\psi)\big]$$
$$+\big\{(\cos(\theta)-\xi\sin(\theta))^2+\eta^2\sin^2(\theta)\big\}^{(s-1)/2}\big[\big\{-A_3(\xi+H_1)+A_4(\eta+H_2)\big\}\cos((s-1)\psi')$$
$$-\big\{A_3(\eta+H_2)+A_4(\xi+H_1)\big\}\sin((s-1)\psi')\big]\Big\rangle+O(r^{s+1}), \tag{88c}$$

$$\sigma_z(r,\theta,z) = r^{s-1}D_b(z)(ik)^s s c_{12}\Big\langle\big\{(\cos(\theta)+\xi\sin(\theta))^2+\eta^2\sin^2(\theta)\big\}^{(s-1)/2}[(A_1\{1$$
$$+\xi H_1-\eta H_2\}+A_2\{\eta H_1+\xi H_2\})\cos((s-1)\psi)+(-A_1\{\eta H_1+\xi H_2\}$$
$$+A_2\{1+\xi H_1-\eta H_2\})\sin((s-1)\psi)]+\big\{(\cos(\theta)-\xi\sin(\theta))^2$$
$$+\eta^2\sin^2(\theta)\big\}^{(s-1)/2}[(A_3\{1+\xi H_1-\eta H_2\}-A_4\{\eta H_1+\xi H_2\}\big)\cos((s-1)\psi'))$$
$$+(A_3\{\eta H_1+\xi H_2\}-A_4\{1+\xi H_1-\eta H_2\})\sin((s-1)\psi')]\Big\rangle+O(r^{s+1}), \tag{88d}$$

$$\tau_{xz}(r,\theta,z)=O(r^s);\quad \tau_{yz}(r,\theta,z)=O(r^s), \tag{88e, f}$$

in which

$$A_1=\bar{A}_1+\bar{A}_2,\quad A_2=i(\bar{A}_1-\bar{A}_2), \tag{89a}$$

$$A_3=\bar{A}_3+\bar{A}_4,\quad A_4=i(\bar{A}_3-\bar{A}_4), \tag{89b}$$

and

$$D_b(z)=D_1\sin(kz)+D_2\cos(kz), \tag{90}$$

with

$$D_1=i\bar{\bar{D}}_1,\quad D_2=\bar{\bar{D}}_2. \tag{91a, b}$$

It may be noted that since s or Re s (when s is complex) is positive, all the higher order terms in Equation (88) vanish as $r\to 0$. The components of displacement can now be expressed in the cylindrical polar coordinate system as follows:

$$u_r(r,\theta,z) = r^s D_b(z)(ik)^s\Big\langle\big\{(\cos(\theta)+\xi\sin(\theta))^2+\eta^2\sin^2(\theta)\big\}^{s/2}\big[\big\{A_1\cos(\theta)$$
$$+(H_1A_1+H_2A_2)\sin(\theta)\big\}\cos(s\psi)+\big\{A_2\cos(\theta)+(H_1A_2-H_2A_1)\sin(\theta)\big\}\sin(s\psi)\big]$$
$$+\big\{(\cos(\theta)-\xi\sin(\theta))^2+\eta^2\sin^2(\theta)\big\}^{s/2}\big[\big\{A_3\cos(\theta)+(-H_1A_3+H_2A_4)\sin(\theta)\big\}$$
$$\times\cos(s\psi')+\big\{A_4\cos(\theta)-(H_1A_4-H_2A_3)\sin(\theta)\big\}\sin(s\psi')\big]\Big\rangle+O(r^{s+2}), \tag{92a}$$

$$u_\theta(r,\theta,z) = r^s D_b(z)(ik)^s \Big\langle \big\{(\cos(\theta)+\xi\sin(\theta))^2+\eta^2\sin^2(\theta)\big\}^{s/2}\big[\big\{-A_1\sin(\theta) + (H_1A_1+H_2A_2)\cos(\theta)\big\}\cos(s\psi) + \big\{-A_2\sin(\theta)+(H_1A_2-H_2A_1)\cos(\theta)\big\}\sin(s\psi)\big] + \big\{(\cos(\theta)-\xi\sin(\theta))^2+\eta^2\sin^2(\theta)\big\}^{s/2}\big[-\big\{A_3\sin(\theta)+(H_1A_3-H_2A_4)\cos(\theta)\big\} \times\cos(s\psi') - \big\{A_4\sin(\theta)+(H_1A_4+H_2A_3)\cos(\theta)\big\}\sin(s\psi')\big]\Big\rangle + O(r^{s+2}), \tag{92b}$$

$$w(r,\theta,z) = O(r^{s+1}). \tag{92c}$$

Similarly, the components of the asymptotic stress field can be conveniently expressed by using standard transformation rule:

$$\begin{Bmatrix}\sigma_r\\ \sigma_\theta\\ \tau_{r\theta}\end{Bmatrix} = \begin{bmatrix}\cos^2\theta & \sin^2\theta & \sin 2\theta\\ \sin^2\theta & \cos^2\theta & -\sin 2\theta\\ -\frac{1}{2}\sin 2\theta & \frac{1}{2}\sin 2\theta & \cos 2\theta\end{bmatrix}\begin{Bmatrix}\sigma_x\\ \sigma_y\\ \tau_{xy}\end{Bmatrix}, \tag{93a}$$

$$\begin{Bmatrix}\tau_{rz}\\ \tau_{\theta z}\end{Bmatrix} = \begin{bmatrix}\cos\theta & \sin\theta\\ -\sin\theta & \cos\theta\end{bmatrix}\begin{Bmatrix}\tau_{xz}\\ \tau_{yz}\end{Bmatrix}. \tag{93b}$$

The stress component, σ_z, is as given in Equation (88d).

Appendix 2. Details of the derivation of the solution involving imaginary roots for a (010) [001] through-crack (mode I/II loading)

This appendix provides some of the details of the mathematical derivation of the solution, involving imaginary roots, for a cubic crystals plate, weakened by (010) [001] through-crack and subjected to mode I/II loading (Section 5, Case (b)). The components of displacement that satisfy the Equilibrium Equations (1) can be expressed in the following form:

$$u(x,y,z) = \Big(\bar{\bar{D}}_1 i\sin(kz)+\bar{\bar{D}}_2\cos(kz)\Big)(ik)^s\big[\bar{A}_1(x+i(\xi'+\eta')y)^s + \bar{A}_2(x-i(\xi'+\eta')y)^s + \bar{A}_3(x+i(\xi'-\eta')y)^s + \bar{A}_4(x-i(\xi'-\eta')y)^s\big], \tag{94a}$$

$$v(x,y,z) = \Big(\bar{\bar{D}}_1 i\sin(kz)+\bar{\bar{D}}_2\cos(kz)\Big)(ik)^s\big[\bar{B}_1(x+i(\xi'+\eta')y)^s + \bar{B}_2(x-i(\xi'+\eta')y)^s + \bar{B}_3(x+i(\xi'-\eta')y)^s + \bar{B}_4(x-i(\xi'-\eta')y)^s\big], \tag{94b}$$

$$w(x,y,z) = \Big(\bar{\bar{D}}_1\cos(kz)+\bar{\bar{D}}_2 i\sin(kz)\Big)(ik)^{s+1}\big[\bar{C}_1(x+i(\xi'+\eta')y)^{s+1} + \bar{C}_2(x-i(\xi'+\eta')y)^{s+1} + \bar{C}_3(x+i(\xi'-\eta')y)^{s+1} + \bar{C}_4(x-i(\xi'-\eta')y)^{s+1}\big], \tag{94c}$$

where ξ' and $\eta'$are as given in Equation (39), and $\bar{A}_k$, $\bar{B}_k$, $\bar{C}_k$, $k=1,\ldots,4$, are undetermined coefficients. It may be noted that $\bar{B}_k$ can be expressed in terms of the corresponding $\bar{A}_k$, $k=1,\ldots,4$, by using Equations (15) and (38).

$$\bar{B}_1 = -iH_1'\bar{A}_1, \quad \bar{B}_2 = iH_1'\bar{A}_2, \tag{95a, b}$$

$$\bar{B}_3 = -iH_2'\bar{A}_3, \quad \bar{B}_4 = iH_2'\bar{A}_4, \tag{95c, d}$$

in which

$$H_1' = -\frac{\left\{c_{11} - c_{66}(\xi' + \eta')^2\right\}}{(c_{12} + c_{66})(\xi' + \eta')}, \quad H_2' = -\frac{\left\{c_{11} - c_{66}(\xi' - \eta')^2\right\}}{(c_{12} + c_{66})(\xi' - \eta')}. \tag{96a, b}$$

The corresponding stress field can easily be obtained from Equation (94). It is convenient to express the components of the displacement vector and stress tensor, in terms of the cylindrical polar coordinate system (r, θ, z), see Figure 27. Expressing

$$\rho_1 \cos(\psi_1(\theta)) = r\cos(\theta), \quad \rho_1 \sin(\psi_1(\theta)) = r(\xi' + \eta')\sin(\theta), \tag{97a}$$

$$\rho_1' \cos(\psi_1'(\theta)) = r\cos(\theta), \quad \rho_1' \sin(\psi_1'(\theta)) = r(\xi' + \eta')\sin(\theta), \tag{97b}$$

in which

$$\rho_1 = r\left\{\cos^2(\theta) + (\xi' + \eta')^2 \sin^2(\theta)\right\}^{1/2}, \tag{98a}$$

$$\rho_1' = r\left\{\cos^2(\theta) + (\xi' - \eta')^2 \sin^2(\theta)\right\}^{1/2}, \tag{98b}$$

and

$$\cos(\psi_1(\theta)) = \frac{\cos(\theta)}{\left\{\cos^2(\theta) + (\xi' + \eta')^2 \sin^2(\theta)\right\}^{1/2}}, \tag{99a}$$

$$\sin(\psi_1(\theta)) = \frac{(\xi' + \eta')\sin(\theta)}{\left\{\cos^2(\theta) + (\xi' + \eta')^2 \sin^2(\theta)\right\}^{1/2}}, \tag{99b}$$

$$\cos(\psi_1'(\theta)) = \frac{\cos(\theta)}{\left\{\cos^2(\theta) + (\xi' - \eta')^2 \sin^2(\theta)\right\}^{1/2}}, \tag{99c}$$

$$\sin(\psi_1'(\theta)) = \frac{(\xi' - \eta')\sin(\theta)}{\left\{\cos^2(\theta) + (\xi' - \eta')^2 \sin^2(\theta)\right\}^{1/2}}, \tag{99d}$$

the general asymptotic form for the displacement and stress fields can be written as follows:

$$u(r,\theta,z) = r^s D_b(z)(ik)^s \Big[\left\{\cos^2(\theta) + (\xi' + \eta')^2 \sin^2(\theta)\right\}^{s/2}\left\{A_1 \cos(s\psi_1) + A_2 \sin(s\psi_1)\right\} + \left\{\cos^2(\theta) + (\xi' - \eta')^2 \sin^2(\theta)\right\}^{s/2}\left\{A_3 \cos(s\psi_1') + A_4 \sin(s\psi_1')\right\}\Big] + O(r^{s+2}), \tag{100a}$$

$$v(r,\theta,z) = r^s D_b(z)(ik)^s \Big[\left\{\cos^2(\theta) + (\xi' + \eta')^2 \sin^2(\theta)\right\}^{s/2}\left\{-H_1' A_2 \cos(s\psi_1) + H_1' A_1 \sin(s\psi_1)\right\} + \left\{\cos^2(\theta) + (\xi' - \eta')^2 \sin^2(\theta)\right\}^{s/2}\left\{-H_2' A_4 \cos(s\psi_1') + H_2' A_3 \sin(s\psi_1')\right\}\Big] + O(r^{s+2}), \tag{100b}$$

$$w(r,\theta,z) = O(r^{s+1}), \tag{100c}$$

and

$$\sigma_s(r,\theta,z) = r^{s-1} D_b(z)(ik)^s s\Big\{\left\{\cos^2(\theta) + (\xi' + \eta')^2 \sin^2(\theta)\right\}^{(s-1)/2}\left\{c_{11} + H_1'(\xi + \eta)c_{12}\right\} \times \left\{A_1 \cos((s-1)\psi_1) + A_2 \sin((s-1)\psi_1)\right\} + \left\{\cos^2(\theta) + (\xi' - \eta')^2 \sin^2(\theta)\right\}^{(s-1)/2} \times \left\{c_{11} + H_2'(\xi - \eta)c_{12}\right\}\left\{A_3 \cos((s-1)\psi_1') + A_4 \sin\left((s-1)\psi_1'\right)\right\}\Big\} + O(r^{s+1}), \tag{101a}$$

$$\sigma_y(r,\theta,z) = r^{s-1} D_b(z)(ik)^s s\Big\{\big\{\cos^2(\theta)+(\xi'+\eta')^2\sin^2(\theta)\big\}^{(s-1)/2}\big\{c_{12}+H_1'(\xi+\eta)c_{11}\big\}$$
$$\times\big\{A_1\cos((s-1)\psi_1)+A_2\sin((s-1)\psi_1)\big\}+\big\{\cos^2(\theta)+(\xi'-\eta')^2\sin^2(\theta)\big\}^{(s-1)/2}$$
$$\times\{c_{12}+H_2'(\xi-\eta)c_{11}\}\big\{A_3\cos((s-1)\psi_1')+A_4\sin((s-1)\psi_1')\big\}\Big\}+O(r^{s+1}), \qquad (101b)$$

$$\tau_{xy}(r,\theta,z) = r^{s-1} D_b(z)(ik)^s s c_{66}\Big\{\big\{\cos^2(\theta)+(\xi'+\eta')^2\sin^2(\theta)\big\}^{(s-1)/2}\Big[\big\{H_1'-(\xi'+\eta')\big\}$$
$$\times\big\{-A_2\cos((s-1)\psi_1)+A_1\sin((s-1)\psi_1)\big\}+\big\{\cos^2(\theta)+(\xi'-\eta')^2\sin^2(\theta)\big\}^{(s-1)/2}$$
$$\times\big\{H_2'-(\xi'-\eta')\big\}\big\{-A_4\cos((s-1)\psi_1')+A_3\sin((s-1)\psi_1')\big\}+O(r^{s+1}), \qquad (101c)$$

$$\sigma_z(r,\theta,z) = r^{s-1} D_b(z)(ik)^s s c_{12}\Big\{\big\{\cos^2(\theta)+(\xi'+\eta')^2\sin^2(\theta)\big\}^{(s-1)/2}$$
$$\times\big\{1+H_1'(\xi+\eta)\big\}\big\{A_1\cos((s-1)\psi_1)+A_2\sin((s-1)\psi_1)\big\}$$
$$+\big\{\cos^2(\theta)+(\xi'-\eta')^2\sin^2(\theta)\big\}^{(s-1)/2}\big\{1+H_2'(\xi-\eta)\big\}\big\{A_3\cos((s-1)\psi_1')$$
$$+A_4\sin((s-1)\psi_1')\big\}+O(r^{s+1}), \qquad (101d)$$

$$\tau_{xz}(r,\theta,z)=O(r^s), \quad \tau_{yz}(r,\theta,z)=O(r^s), \qquad (101e,f)$$

in which A_k, $k=1,\ldots,4$, is defined as before in Equation (89), whereas $D_b(z)$ is the same as given earlier in Equations (90) and (91).

It may be noted that since s or Re s (when s is complex) is positive, all the higher order terms in Equation (101) vanish as $r\to 0$. The components of displacement can now be expressed in the cylindrical polar coordinate system as follows:

$$u_r(r,\theta,z) = r^s D_b(z)(ik)^s\Big\{\big\{\cos^2(\theta)+(\xi'+\eta')^2\sin^2(\theta)\big\}^{s/2}\Big[\big\{A_1\cos(\theta)-H_1'A_2\sin(\theta)\big\}\cos(s\psi_1)$$
$$+\big\{A_2\cos(\theta)+H_1'A_1\sin(\theta)\big\}\sin(s\psi_1)\Big]+\big\{\cos^2(\theta)+(\xi'-\eta')^2\sin^2(\theta)\big\}^{s/2}$$
$$\times\Big[\big\{A_3\cos(\theta)-H_2'A_4\sin(\theta)\big\}\cos(s\psi_1')+\big\{A_4\cos(\theta)+H_2'A_3\sin(\theta)\big\}\sin(s\psi_1')\Big]\Big\}+O(r^{s+2}), \qquad (102a)$$

$$u_\theta(r,\theta,z) = r^s D_b(z)(ik)^s\Big\{\big\{\cos^2(\theta)+(\xi'+\eta')^2\sin^2(\theta)\big\}^{s/2}\Big[-\big\{A_1\sin(\theta)+H_1'A_2\cos(\theta)\big\}\cos(s\psi_1)$$
$$+\big\{-A_2\sin(\theta)+H_1'A_1\cos(\theta)\big\}\sin(s\psi_1)\Big]+\big\{\cos^2(\theta)+(\xi'-\eta')^2\sin^2(\theta)\big\}^{s/2}$$
$$\times\Big[-\big\{A_3\sin(\theta)+H_2'A_4\cos(\theta)\big\}\cos(s\psi_1')+\big\{-A_4\sin(\theta)+H_2'A_3\cos(\theta)\big\}\sin(s\psi_1')\Big]\Big\}$$
$$+O(r^{s+2}), \qquad (102b)$$

$$w(r,\theta,z)=O(r^{s+1}). \qquad (102c)$$

Similarly, the components of the asymptotic stress field can be conveniently expressed by using standard transformation rule, given earlier in Equation (93). The stress component, σ_z, is as given in Equation (101d).

Appendix 3. Solution for a $(1\bar{1}0)[110]$ through-crack

(i) Mode III loading

The asymptotic solutions for displacements and stresses in a cubic crystal plate weakened by a $(1\bar{1}0)[110]$ through-crack and subjected to mode III loading (Section 7), are presented here.

Following a similar procedure as outlined in Appendix 2, for nontrivial c_s, the characteristic equation for the system of PDEs, Equations (56), is obtained as follows:

$$c_{66} + c'_{66}p^2 = 0, \tag{103a}$$

leading to

$$p_{1,2} = \pm i\sqrt{\frac{c_{66}}{c'_{66}}}. \tag{103b}$$

The displacement and stress fields in the vicinity of a semi-infinite crack front can now be expressed in the same manner as that of an orthorhombic plate [69].

(ii) Mode I/II loadings

The asymptotic solutions for displacements and stresses in a cubic crystal plate weakened by a $(1\bar{1}0)[110]$ through-crack and subjected to mode I/II loading (Section 7), are presented here.

(a) Complex roots

By following a similar procedure as outlined above in Section 5 and Appendix 1, and defining the mode I stress intensity factor, $K_I(z)$, as

$$K_I(z) = \sqrt{2}D_b(z)(ik)^{1/2}\left(\sqrt{c_{11}c_{22}} + c_{12}\right)A_1, \tag{104}$$

the components of in-plane displacements in the vicinity of a semi-infinite crack front, under symmetric far-field loading, can be expressed as follows:

$$\begin{aligned} u(r,\theta,z) = \frac{K_I(z)}{(c_{11}c'_{11} - c_{12}^2)}\sqrt{\frac{r}{2}}\Bigg[&\left\{(\cos\theta + \xi''\sin\theta)^2 + \eta''\sin^2\theta\right\}^{1/4}\Bigg\{\left(\sqrt{c_{11}c'_{11}} - c_{12}\right)\cos(\psi/2) \\ &- \left(\sqrt{c_{11}c'_{11}} + c_{12}\right)\frac{\eta''}{\xi''}\sin(\psi/2)\Bigg\} + \left\{(\cos\theta - \xi''\sin\theta)^2 + \eta''\sin^2\theta\right\}^{1/4} \\ &\times\left\{\left(\sqrt{c_{11}c'_{11}} - c_{12}\right)\cos(\psi'/2) + \left(\sqrt{c_{11}c'_{11}} + c_{12}\right)\frac{\eta''}{\xi''}\sin(\psi'/2)\right\}\Bigg], \end{aligned} \tag{105a}$$

$$\begin{aligned} v(r,\theta,z) = \frac{K_I(z)}{(c_{11}c'_{11} - c_{12}^2)}\sqrt{\frac{r}{2}}\Bigg[&\left\{(\cos\theta + \xi''\sin\theta)^2 + \eta''\sin^2\theta\right\}^{1/4}\Bigg\{-\frac{(c_{11}c'_{11} - c_{12}^2)}{2c_{66}\xi''}\cos(\psi/2) \\ &+ 2\sqrt{c_{11}c'_{11}}\eta''\sin(\psi/2)\Bigg\} + \left\{(\cos\theta - \xi''\sin\theta)^2 + \eta''\sin^2\theta\right\}^{1/4} \\ &\times\left\{\frac{(c_{11}c'_{11} - c_{12}^2)}{2c_{66}\xi''}\cos(\psi'/2) + 2\sqrt{c_{11}c'_{11}}\eta''\sin(\psi'/2)\right\}\Bigg], \end{aligned} \tag{105b}$$

whereas the components of in-plane displacements in the vicinity of a semi-infinite crack front, under skew-symmetric far-field loading, can be expressed as follows:

$$\begin{aligned} u(r,\theta,z) = \frac{K_{II}(z)}{(c_{11}c'_{11} - c_{12}^2)}\sqrt{\frac{r}{2}}\Bigg[&\left\{(\cos\theta + \xi''\sin\theta)^2 + \eta''\sin^2\theta\right\}^{1/4}\Bigg\{\frac{(c_{11}c'_{11} - c_{12}^2)}{2c_{66}\xi''}\cos(\psi/2) \\ &+ 2\sqrt{c_{11}c'_{11}}\eta''\sin(\psi/2)\Bigg\} + \left\{(\cos\theta - \xi''\sin\theta)^2 + \eta''\sin^2\theta\right\}^{1/4} \\ &\times\left\{-\frac{(c_{11}c'_{11} - c_{12}^2)}{2c_{66}\xi''}\cos(\psi'/2) + 2\sqrt{c_{11}c'_{11}}\eta''\sin(\psi'/2)\right\}\Bigg], \end{aligned} \tag{106a}$$

$$v(r,\theta,z) = -\frac{K_{II}(z)}{(c_{11}c'_{11}-c_{12}^2)}\sqrt{\frac{r}{2}}\Bigg[\left\{(\cos\theta+\xi''\sin\theta)^2+\eta''\sin^2\theta\right\}^{1/4}\left\{\left(\sqrt{c_{11}c'_{11}}-c_{12}\right)\cos(\psi/2)\right.$$
$$\left.+\left(\sqrt{c_{11}c'_{11}}+c_{12}\right)\frac{\eta''}{\xi''}\sin(\psi/2)\right\}+\left\{(\cos\theta-\xi''\sin\theta)^2+\eta''\sin^2\theta\right\}^{1/4}$$
$$\times\left\{\left(\sqrt{c_{11}c'_{11}}-c_{12}\right)\cos(\psi'/2)-\left(\sqrt{c_{11}c'_{11}}+c_{12}\right)\frac{\eta''}{\xi''}\sin(\psi'/2)\right\}\Bigg], \tag{106b}$$

in which ψ and ψ' are given by Equations (86a, b) and (86c, d), respectively, with ξ and η being replaced by ξ'' and η'', respectively. The expressions for stress components can also be written by using appropriate ψ and ψ', and also replacing ξ and η by ξ'' and η'', respectively in Equations (31) and (37) for mode I and mode II loading, respectively. This case is similar to its orthotropic (transversely isotropic) counterpart [70].

Case (b): imaginary roots

By following a similar procedure as outlined above in Section 5 and Appendix 2, and defining the mode I stress intensity factor, $K_I(z)$, as

$$K_I(z) = \sqrt{2}D_b(z)(ik)^{1/2}\frac{c_{66}\eta'''}{(c_{12}+c_{66})}\left\{\sqrt{c_{11}c_{22}}(\xi'''-\eta''')+c_{12}(\xi'''+\eta''')\right\}A_1, \tag{107}$$

the components of in-plane displacements, in the vicinity of a semi-infinite crack front, under symmetric far-field loading, can be expressed as follows:

$$u(r,\theta,z) = \frac{K_I(z)}{(c_{11}c'_{11}-c_{12}^2)\eta'}\sqrt{\frac{r}{2}}\Bigg[\left\{\cos^2\theta+(\xi'''+\eta''')^2\sin^2\theta\right\}^{1/4}\left\{\sqrt{c_{11}c'_{11}}(\xi'''+\eta''')\right.$$
$$\left.+c_{12}(\xi'''-\eta''')\right\}\cos(\psi_1/2)-\left\{\cos^2\theta+(\xi'''-\eta''')^2\sin^2\theta\right\}^{1/4}\left\{\sqrt{c_{11}c'_{11}}(\xi'''-\eta''')\right.$$
$$\left.+c_{12}(\xi'''+\eta''')\right\}\cos(\psi'_1/2)\Bigg], \tag{108a}$$

$$v(r,\theta,z) = \frac{K_I(z)}{(c_{11}c'_{11}-c_{12}^2)\eta'''}\sqrt{\frac{r}{2}}\Bigg[\left\{\cos^2\theta+(\xi'''+\eta''')^2\sin^2\theta\right\}^{1/4}\left\{c_{12}+\sqrt{c_{11}c'_{11}}(\xi'''-\eta''')^2\right\}\sin(\psi_1/2)$$
$$-\left\{\cos^2\theta+(\xi'''-\eta''')^2\sin^2\theta\right\}^{1/4}\left\{c_{12}+\sqrt{c_{11}c'_{11}}(\xi'''+\eta''')^2\right\}\sin(\psi'_1/2)\Bigg]. \tag{108b}$$

By defining the mode II stress intensity factor, $K_{II}(z)$, as

$$K_{II}(z) = \sqrt{2}D_b(z)(ik)^{1/2}\frac{c_{66}\eta'''}{(c_{12}+c_{66})(\xi'''+\eta''')}\left\{\sqrt{c_{11}c_{22}}(\xi'''-\eta''')+c_{12}(\xi'''+\eta''')\right\}A_2, \tag{109}$$

the components of in-plane displacements, in the vicinity of a semi-infinite crack front, under skew-symmetric far-field loading, can be expressed as follows:

$$u(r,\theta,z) = -\frac{K_{II}(z)}{(c_{11}c'_{11}-c_{12}^2)\eta'''}\sqrt{\frac{r}{2}}\Bigg[\left\{\cos^2\theta+(\xi'''+\eta''')^2\sin^2\theta\right\}^{1/4}$$
$$\times\left\{\sqrt{c_{11}c'_{11}}(\xi'''+\eta''')^2+c_{12}\right\}\sin(\psi_1/2)-\left\{\cos^2\theta+(\xi'''-\eta''')^2\sin^2\theta\right\}^{1/4}$$
$$\times\left\{\sqrt{c_{11}c'_{11}}(\xi'''-\eta''')^2+c_{12}\right\}\sin(\psi'_1/2)\Bigg], \tag{110a}$$

$$v(r,\theta,z)=\frac{K_{II}(z)}{(c_{11}c'_{11}-c_{12}^2)\eta'''}\sqrt{\frac{r}{2}}\Big[\{\cos^2\theta+(\xi'''+\eta''')^2\sin^2\theta\}^{1/4}\Big\{\sqrt{c_{11}c'_{11}}(\xi'''-\eta''')$$
$$+c_{12}(\xi'''+\eta''')\Big\}\cos(\psi_1/2)-\{\cos^2\theta+(\xi'''-\eta'')^2\sin^2\theta\}^{1/4}$$
$$\times\Big\{\sqrt{c_{11}c'_{11}}(\xi'''+\eta''')+c_{12}(\xi'''-\eta''')\Big\}\cos(\psi'_1/2)\Big], \tag{110b}$$

in which ψ_1 and ψ'_1 are given by Equations (99a, b) and (99c, d), respectively, with ξ' and η' being replaced by ξ''' and η''', respectively. The expressions for stress components can also be written by using appropriate ψ_1 and ψ'_1, and also replacing ξ' and η' by ξ''' and η''', respectively in Equations (45) and (50) for mode I and mode II loading, respectively. This case is again similar to its orthotropic (transversely isotropic) counterpart [70].

Appendix 4. Comparison of solutions involving complex and imaginary roots with their isotropic counterpart

Similarity or dissimilarity of the present asymptotic solutions involving complex and imaginary roots with their isotropic counterparts, referred to in Section 5, is presented here.

(a) Isotropic materials

The in-plane displacements for an isotropic material can be rewritten in the form (for $n=0$) [44]:

$$U(x,y)=a_s(ik)^s\rho^s\exp(ip\psi), \tag{111a}$$

$$V(x,y)=b_s(ik)^s\rho^s\exp(ip\psi), \tag{111b}$$

in which

$$p=\pm(s\pm1), \tag{112}$$

$$\rho=\sqrt{x^2+y^2}, \tag{113}$$

and

$$\psi=\tan^{-1}\left(\frac{y}{x}\right). \tag{114}$$

Therefore, for an isotropic material when $x=0$, $\psi=\pi/2$ for all positive values of y.

(b) Solution involving complex roots

Going back to Equations (13a, b) and (21), the in-plane displacements can be rewritten in the form (for $n=0$):

$$U(x,y)=a_s(ik)^s(x+py)^s=a_s(ik)^s\rho^s\exp(is\psi), \tag{115a}$$

$$V(x,y)=b_s(ik)^s(x+py)^s=b_s(ik)^s\rho^s\exp(is\psi), \tag{115b}$$

in which ρ and ψ can be rewritten as follows:

$$\rho = \sqrt{(x \pm \xi y)^2 + \eta^2 y^2}, \tag{116}$$

and

$$\psi = \tan^{-1}\left(\frac{\pm \eta y}{x \pm \xi y}\right). \tag{117}$$

Therefore, for a cubic crystal with complex roots when $x = 0$,

$$\psi = \tan^{-1}\left(\frac{\pm \eta}{\pm \xi}\right) \tag{118}$$

for all positive values of y, which differs from its isotropic counterpart.

(c) Solution involving imaginary roots

Going back to Equations (13a, b) and (38), the in-plane displacements can be rewritten in the form (for $n = 0$):

$$U(x, y) = a_s(ik)^s(x + py)^s = a_s(ik)^s \rho^s \exp(is\psi), \tag{119a}$$

$$V(x, y) = b_s(ik)^s(x + py)^s = b_s(ik)^s \rho^s \exp(is\psi), \tag{119b}$$

in which ρ and ψ can be rewritten as follows:

$$\rho = \sqrt{x^2 + (\pm \xi \pm \eta)^2 y^2}, \tag{120}$$

and

$$\psi = \tan^{-1}\left(\frac{(\pm \xi \pm \eta) y}{x}\right). \tag{121}$$

Therefore, for a cubic crystal with imaginary roots when $x = 0$, $\psi = \pi/2$ for all positive values of y, which is in accord with its isotropic counterpart.

Appendix 5. Determination of critical stress for bond kinking in shear

Some of the details of the mathematical derivation of the solution for critical applied stress for bond failure in shear, referred to in Section 8, are presented here. The total potential energy, Π_s is given by

$$\Pi_s = U_s + W, \tag{122}$$

in which U_s represents the strain energy in shear, whereas W denotes the potential due to applied stress, σ_s^+, responsible for shear deformation of bonds.

U_s can be written as follows:

$$U_s = \frac{1}{2s_{66}} \int_0^L (\gamma_{xy})^2 \mathrm{d}y, \tag{123}$$

where

$$\gamma_{xy} = u_{,y} + v_{,x}. \tag{124}$$

W can be written as (for $u_0 > u$)

$$W = -\int_0^L \sigma_s^+ \left\{ \frac{\mathrm{d}v}{\mathrm{d}y} + \frac{1}{2}\left[\left(\frac{\mathrm{d}u_0}{\mathrm{d}y}\right)^2 - \left(\frac{\mathrm{d}(u_0 - u)}{\mathrm{d}y}\right)^2 \right] \right\} \mathrm{d}y. \tag{125}$$

u, u_0 and v are assumed in the form of Fourier series as given below:

$$u = \sum_{n=1}^{\infty} f_n \sin\left(\frac{n\pi y}{2L}\right), \tag{126}$$

$$u_0 = \sum_{n=1}^{\infty} f_{n0} \sin\left(\frac{n\pi y}{2L}\right), \tag{127}$$

$$v = \sum_{n=1}^{\infty} g_n \sin\left(\frac{n\pi y}{2L}\right). \tag{128}$$

Substitution of Equations (126)–(128) into Equations (123)–(125), and further substitution of the results into Equation (122), and applying the principle of stationarity of the total potential energy will yield the critical applied stress for bond failure in shear as given below:

$$\sigma_{sc}^+ = \frac{1}{s_{66}} \frac{f_n}{(f_{n0} - f_n)}; \quad n = 1, 2, \ldots \tag{129}$$

The lowest, σ_{sc}^+, is obtained when $n = 1$, and is approximated by

$$\sigma_{sc}^+ = \frac{1}{s_{66}} \frac{f/L}{(f_0 - f)/L} \approx \frac{1}{s_{66}} \frac{\gamma_{bd}}{(\phi_0 - \gamma_{bd})}; \quad \phi_0 > \gamma_{bd} \geq 0, \tag{130}$$

in which $f/L = \gamma_{bd}$ is the shear strain at which a bond kinks, and this makes the crack turn to another cleavage plane/direction. If the computed γ_{bd} is negative, it is taken as zero. A similar analysis on unloading yields the lowest, σ_{sc}^-, which is obtained when $n = 1$, and is given as follows [56]:

$$\sigma_{sc}^- = \frac{1}{s_{66}} \frac{f/L}{(\bar{f}_0 + f)/L} \approx \frac{1}{s_{66}} \frac{\gamma_{bd}}{\phi_0}; \quad \phi_0 > \gamma_{bd} \geq 0, \tag{131}$$

in which $\bar{f}_0/L = \phi_0 - \gamma_{bd}$ and $f/L = \gamma_{bd}$.

Appendix 6. Details of the derivation of the solution for determination of crack deviation angle

Some of the details of the mathematical derivation of the solution for crack deviation angle, referred to in Section 9, are presented here. Green's function operator on the left side of Equation (76) can easily be obtained as follows:

$$\Gamma(x, y) = \ln\left[y^2 + \frac{s_{11}}{s_{66}}(1 + s_{66}\sigma_{sc}^+)x^2 \right]. \tag{132}$$

The final solution is of the form

$$u(x, y) = u_1(x, y) - u_2(x, y'), \tag{133}$$

where

$$y' = y - L, \tag{134}$$

$$u_1(x,y) = \frac{s_{66}\sigma_{sc}^{+}u_0}{L}\int_0^x \ln\left\{y^2 + \frac{s_{11}}{s_{66}}(1 + s_{66}\sigma_{sc}^{+})x^2\right\}\mathrm{d}x, \tag{135a}$$

$$u_2(x,y) = \frac{s_{66}\sigma_{sc}^{+}u_0}{L}\int_0^x \ln\left\{y'^2 + \frac{s_{11}}{s_{66}}(1 + s_{66}\sigma_{sc}^{+})x^2\right\}\mathrm{d}x. \tag{135b}$$

The bond shear strain can now be written as follows:

$$\gamma_{x,y}(x,y) \approx \phi_1(x,y) = u_{1,y}(x,y), \tag{136}$$

Substitution of Equation (135a) into Equation (136) leads to

$$\phi_1(x,y) = \frac{2s_{66}\sigma_{sc}^{+}u_0}{L}\int_0^x \frac{y}{\left\{y^2 + \frac{s_{11}}{s_{66}}(1 + s_{66}\sigma_{sc}^{+})x^2\right\}}\mathrm{d}x. \tag{137}$$

$\phi_2(x,y)$ can similarly be obtained by replacing y by y' in Equation (137). $\phi_{1,\max}$ is given by the condition

$$\int_0^x \left[\frac{2}{\left\{y^2 + \frac{s_{11}}{s_{66}}(1 + s_{66}\sigma_{sc}^{+})x^2\right\}} - \frac{4y^2}{\left\{y^2 + \frac{s_{11}}{s_{66}}(1 + s_{66}\sigma_{sc}^{+})x^2\right\}^2}\right]\mathrm{d}x = 0, \tag{138}$$

which yields

$$y^2 = \frac{s_{11}}{s_{66}}(1 + s_{66}\sigma_{sc}^{+})x^2, \tag{139}$$

or

$$y = \pm\left[\frac{s_{11}}{s_{66}}(1 + s_{66}\sigma_{sc}^{+})\right]^{1/2}x = \pm x\tan\beta, \tag{140}$$

in which

$$\tan(\beta) = \frac{\mathrm{d}y}{\mathrm{d}x} = \pm\left[\frac{s_{11}}{s_{66}}(1 + s_{66}\sigma_{sc}^{+})\right]^{1/2}, \tag{141}$$

as long as

$$y^2 + \frac{s_{11}}{s_{66}}(1 + s_{66}\sigma_{sc}^{+})x^2 \neq 0. \tag{142}$$

$\phi_{2,\max}$ is similarly obtained by replacing y by y'.